Near- to Far-Field Transformation for Arbitrarily-Shaped Rotationally-Symmetric Antenna Measurement Surfaces

by

Joshua Benjamin Julius Philipson

Thesis submitted to the University of Ottawa
in partial fulfillment of the requirements for the degree of

Master of Applied Science
in Electrical & Computer Engineering

Ottawa-Carleton Institute for Electrical and Computer Engineering
School of Electrical Engineering and Computer Science
Faculty of Engineering
University of Ottawa

To my wife, Martina and my daughter, Mia

The joy of my life

ABSTRACT

The wireless industry is such that suppliers of antennas have to adapt their designs to requirement changes over a period of just a few months. In these short design cycles time is crucial. Radiation pattern testing of the antennas at various points in this design cycle are nowadays mostly done using spherical near-field techniques, where the tangential electric field is acquired over an imaginary sphere close to, and surrounding, the antenna under test, and this data then transformed into a far-zone radiation pattern. There are some applications where acquisition over a rotationally symmetric surface other than a spherical one would not only reduce test times, but allow equipment cost reductions as well. However, near-field to far-field transformations for finite non-spherical measurement surface shapes are not available. Such a transformation is proposed, implemented and validated in this thesis. It uses the method of moments, customized to a rotationally symmetric surface (body of revolution) to effect this transformation.

Keywords:

near-field antenna measurements; near-field to far-field transformation; method of moments, body of revolution

ACKNOWLEDGEMENTS

I had already worked as a design engineer in the photonics industry for 15 years when I decided to take some graduate courses on a variety of subjects on a part-time basis. Two of the courses I took on computational electromagnetics piqued my interest in the topic, and so I decided to tackle a thesis that involved such work. In my undergraduate degree, I had never had the opportunity to solve numerically for complicated cases. The cases were always special ones, with limiting assumptions. I was enthusiastic and motivated to learn how to solve these numerically. I have since come to understand the complexity of developing 3D computational electromagnetics code from scratch (even if the 3D scatterer is rotationally symmetric), and when one has a 'day job'! Oy!!

I have absolutely no doubt that doing an MASc degree was one of the best decisions of my life. Doing this on a part time basis seemed an Odyssean quest at certain times, and it had certainly not always been smooth nor easy. A mixture of happiness, sadness, excitement and stress made this an unforgettable adventure. There are so many people who have made this journey easier and more enjoyable for me, but I wish to express my genuine and profound gratitude to the following individuals in particular.

First and foremost, I thank my supervisor Dr. Derek McNamara for serving as my mentor and providing me with an exceptional environment to develop my professional skills and to grow intellectually. For your teaching, listening and walking alongside me during this journey, I will be eternally grateful. This has not been solely academic in nature, but personal, and you have touched my life deeply. I would be remiss not to add a specific note of gratitude to Dr. McNamara for allowing me to liberally garner background material from the notes of the various courses he presented at the University of Ottawa. Sir, Proverbs 22:29 refer to such as you.

I would also like sincerely to thank Dr. Daniël Janse van Rensburg for the helpful discussions and support, and for originally suggesting the idea.

I thank my wife Martina, for her inspiration, unwavering support, and endless patience with me. To you, and you forever, I sing the Song of Solomon 8:6-7. I love you so very much.

I thank my daughter Mia, for encouraging me with my homework, for visiting me when I was lonely, for your piano practices that filled our home, for your comics, but most of all, for you being you. I love you. Psalm 37:23-24.

Mom and Dad, your unconditional love has helped me through so many tough times and has made me the person I am today. Psalm 27:4. To Anyu and Apu - words fail me. I'm so grateful and I miss you both so much. I wish you could be here to see this. I know you would have been so proud of all of us.

I wish to acknowledge Chris Wagner & Dave Coomber, for their support & encouragement in pursuing this work.

Also, I thank Dr. Hamad Alroughani for his assistance in obtaining the reference scattered field data used in Section 4.3.3. These were critical results and catalyzed the convergence of this work. Thank you for your patience and sharing your expertise so freely.

I have so many family, friends, and colleagues that have helped me in matters technical, as well as personal and prayerful, that I could write a dozen more notes of gratitude. You know who you are. I am so deeply grateful to count such special people my friends. Malachi 3:10

Finally, for their financial support, I acknowledge Viavi Solutions. Without their support, this work would not have been possible.

Teach me so Thy works to read
That my faith, new strength accruing,
May from world to world proceed,
Wisdom's fruitful search pursuing;
Till, thy truth my mind imbuing,
I proclaim the eternal creed,
Oft the glorious theme renewing
God our Lord is God indeed.
- James Clerk Maxwell

I will give thee thanks;
for thou art fearfully wondrous;
wondrous are thy works;
and my soul knows it well.
- Psalm 139:14

TABLE OF CONTENTS

List of Figures

List of Tables

Glossary of Symbols

Quantity	*Explanation*
$\hat{n}\times\bar{E}^{NF}(S_{meas})$	Measured tangential electric field on surface S_{meas}.
$\bar{E}^{inc}\left\{M_s^{NF},\theta,\phi\right\}$	The electric field, of the equivalent magnetic current density over S_{meas}, in the far-zone.
$\bar{E}\left\{AUT,\theta,\phi\right\}$	Electric field of the AUT in the far-zone, in direction (θ,ϕ), obtained using the NF-to-FF transformation, with e^{-jkr}/r terms suppressed.
$\bar{E}^{exact}\left\{AUT,\theta,\phi\right\}$	Analytically determined electric field of the AUT in the far-zone, in direction (θ,ϕ), with e^{-jkr}/r term suppressed.
$\bar{r}_s$	A general point on S_{meas} (that is, $\bar{r}_s \in S_{meas}$) Subscript "s" is not an index, but signifies "surface".
$\bar{r}_p$	A point on S_{meas} at which we **sample** the tangential electric field, using interpolation of the acquired tangential electric field data. Subscript "*p*" is an index, with $p=1,2,....,P$. Thus $\{\bar{r}_p, p=1,2,....,P\}$ is a set of such points. Usually $P>Q$.
$\bar{r}_q$	A point on S_{meas} at which the tangential electric field is **acquired** on S_{meas} by measurement. Subscript "q" is an index, with $p=1,2,....,Q$. Thus $\{\bar{r}_q, p=1,2,....,Q\}$ is a set of such points.
$\bar{J}_{\text{pec}}$	Electric current density on the PEC-BOR due to $\bar{M}_s^{NF}$ acting as an impressed shroud of magnetic current density.
N_t	Number of expansion functions along the generatrix
N_{h}	The number of azimuthal harmonics included is $2N_{\text{h}}+1$
$(\bar{J}_{\text{s}},\bar{M}_{\text{s}})$	Symbols used to denote the electric and magnetic surface current densities, respectively, when applying the surface equivalence principle.

Acronyms

Acronym	**Description**
MM	Moment Method
NF-to-FF	Near-Field to Far-Field
MRS	Minimum Radius Sphere
AUT	Antenna Under Test
EFIE	Electric Field Integral Equation
MFIE	Magnetic Field Integral Equation
CFIE	Combined Field Integral Equation

CHAPTER 1
Introduction

1.1 THE WIDESPREAD USE OF ANTENNAS

Wireless communications pervades everything, from communications between individuals, to communications between systems and equipment, to data metering. If anything is wireless (as opposed to wired) then antennas are always required. As the usage of antennas increases so does the need for antenna test facilities. Such facilities are expensive if they must be useable for testing almost any antenna type one can think of. But this is not always needed. Companies often require just what is needed for some specific product, and so customized less-expensive set-ups may be preferred.

1.2 THE ANTENNA MEASUREMENT PROBLEM

In wireless communications work we are always eventually interested in the far-zone[1] radiation patterns of an antenna[2]. A very complete account of the methods used in the experimental determination of antenna far-zone patterns, and indeed all the details thereon, can be found in [PARI 18]. In essence, such determination of the far-zone radiation patterns consists of two approaches:

(a). *Direct measurement of the far-zone fields* using a test arrangement such as that depicted in Fig1.2-1. The antenna-under-test (AUT) whose far-field (FF) radiation pattern is to be measured is placed a distance R from a second antenna. The signal level received by the second antenna as the AUT rotates gives the far-zone radiation pattern of the AUT as long as R is sufficiently large that the second antenna is in the far-zone of the AUT.

(b). *Indirect determination of the far-zone fields* of the AUT using an arrangement depicted in Fig.1.2-2. The fields of the AUT are determined over a surface[3] in the near-field (NF) of the

[1] Appendix A defines the notation we will use for various field quantities, and a description of what is meant by near-field and far-field quantities.
[2] Other aspects of antenna performance may of course be of interest too. We are merely saying that the far-zone pattern performance is almost always one of them.
[3] In practice, usually spherical. We will denote the NF measurement surface by S_{meas}.

AUT, and then transformed to the FF using a NF-to-FF[4] transformation. Spherical near-field (SNF) antenna pattern testing is the de-facto standard used throughout the antenna industry since it is the only technique that can circumvent any kind of truncation. Central to this technique is the concept that a given antenna under test (AUT) can be enclosed by a **spherical surface** that is centered on the measurement coordinate system. This sphere is referred to as the "minimum radius sphere" and we use the acronym MRS to denote its radius. The number of spherical modes that must be resolved in a SNF measurement of the AUT is then usually determined as (for free space wavelength λ)

$$N = 2\pi\left(MRS/\lambda\right)+10 \tag{1-1}$$

with the margin of 10 additional spherical wave modes having been selected as described in [PARI 18]. The angular sampling density of near-field (NF) data needed in order to be able to properly reconstruct the far-zone radiation pattern of the AUT is then determined by the angular increments [PARI 18]

$$\Delta\theta = \Delta\phi = 2\pi/(2N+1) \tag{1-2}$$

We suppose that the spherical surface (call it S_{meas}) over which the NF data is acquired has radius R_{meas}. If the probe used to acquire the NF data were infinitesimally small then we could have $R_{meas} = MRS$. In practice this is never possible, due to mechanical interference of positioners and mounting hardware. Furthermore, the closer R_{meas} approaches MRS the more severe the impact of the probe on the actual NF data, and the need for probe correction becomes more significant [PARI 14]. In practice one typically finds that $R_{meas} \approx 2\times MRS$ is used, and then probe correction can often be ignored in in spherical near-field testing.

As the AUT becomes electrically larger the number of spatial samples needed over the measurement sphere increases, and hence so does the acquisition time of the NF data over this measurement sphere. The time taken to perform the near-field to far-field (NF-to-FF) transformation [PARI 18], and the computation of AUT performance parameters from this FF data, is negligible compared to the NF data acquisition time. This is certainly true with all commercial SNF systems.

[4] Acronym for "Near-Field to Far-Field".

The other two canonical NF measurement surfaces are planes and cylinders, and give rise to planar near-field (PNF) and cylindrical near-field (CNF) measurement techniques.

In PNF approaches, the data is obtained by moving a probe AUT across a plane in front of the AUT, sampling data at the required spatial rate (i.e. $<\lambda/2$), where measured signals from two orthogonal polarisations would be required to fully characterise the AUT. The plane over which the data is acquired is finite, and as such if a substantial portion of the power generated and radiated by the AUT is not incident on this plane then the fidelity of the predicted FF will be impaired. Thus the PNF range technique is a useful tool only if it used for sufficiently directive antennas where it can be assumed that by far the vast majority of radiated power is incident on the sampling plane. The plane-rectilinear geometry (e.g. tower-and-rail inverted T scanner and box frame scanner) is by far the most commonly encountered planar implementation, while plane-polar and plane bipolar geometries can also be constructed using mechanically convenient commercially available positioning equipment. The planarity alignment is critical for the PNF transformation and a great deal of effort and ingenuity has been devoted to the mechanical alignment of PNF test systems, through mechanical and optical measurements. The planar technique becomes increasingly inaccurate as the angle between the test and probe antennas increases, though this can be overcome if it forms part of a cylindrical scan. [PARI 14]

In CNF approaches, the data is obtained by combination of single rotation and single linear axes and enables the probe to trace out a conceptual cylindrical surface in three dimensions. Samples are taken at regular intervals across a cylindrical grid with, typically, the probe moving in a fixed linear direction and the AUT rotating in parallel. Typically the linear axis and rotation axes are aligned to the local gravity vector. This simplifies the alignment of the axes of the robotic positioning system, and ensures the AUT does not suffer a variation in the effect of gravity during acquisition. This geometry enables complete azimuth patterns to be obtained providing an antenna pattern including front-to-back ratio whilst maintaining the gravitational vector with respect to the AUT during acquisition. This is particularly attractive for testing gravitationally sensitive AUTs such as space borne antenna assemblies. [PARI 14]

The wireless industry is such that suppliers of antennas have to adapt their designs to changes over a period of just a few months. In these short design cycles time is crucial. Radiation pattern testing of the antennas at various points in this design cycle uses up a large amount of this time. Indeed, it has been said [CONN 01] that "in developing products it is the testing and not the design that is the more expensive, time-consuming, and difficult activity". As a result ways of reducing spherical NF test time has been investigated on an on-going basis, as in [CANO 11], [MART 11], [BEAU13], [DIRE] and [ALMA 19]. There are some applications where acquisition over a rotationally symmetric surface other than a spherical one [JANS 19] would not only reduce test times, but allow equipment cost reductions as well. However, a NF-to-FF transformation for the latter S_{meas} is not available. Such a transformation is proposed, implemented and validated in this thesis.

Some examples of such rotationally symmetric surfaces are circular plane, a capped cylinder and spheroidal [JANS 19]. The surface would not have to be closed, and can be made based upon the characteristics of the AUT and the field of view required. The rotationally symmetric surface is envisioned as being implemented in one of two ways. In the first approach outlined in [JANS 19] this would be done with a six-axis robotic arm combined with a rotary positioner that allows for NF acquisition over a parametrically reconfigurable measurement surface. The six-axis robot describes a generatrix (half of the surface cross section) while the rotator describes a surface of revolution. The perceived benefit of such an approach is the software-defined, parametrically reconfigurable measurement surface. Such reconfigurability will lead not only to test systems that are more space efficient, but also adaptable to many different types of antennas. In a second approach, a probe AUT is made to travel along a generatrix (e.g. 1-D rail gantry, or via a rotationally swept probe arm) while the AUT is placed on a rotary positioner, allowing for NF acquisition over a body-of-revolution surface. The perceived benefit of this second configuration is related to the cost savings associated with decreased robotic complexity.[5]

In either case the success of the BOR method will hinge upon the ability of the scanning probe hardware to repeatedly trace out a 1D scan, with high fidelity, and lessens the robotic constraints of the SNF technique which requires that the system maintain perfect sphericity during the high precision 2D surface scan.

[5] In SNF ranges, the two axes of rotation for θ and ϕ must intersect at a single point in space and have to be perfectly orthogonal [PARI 14]

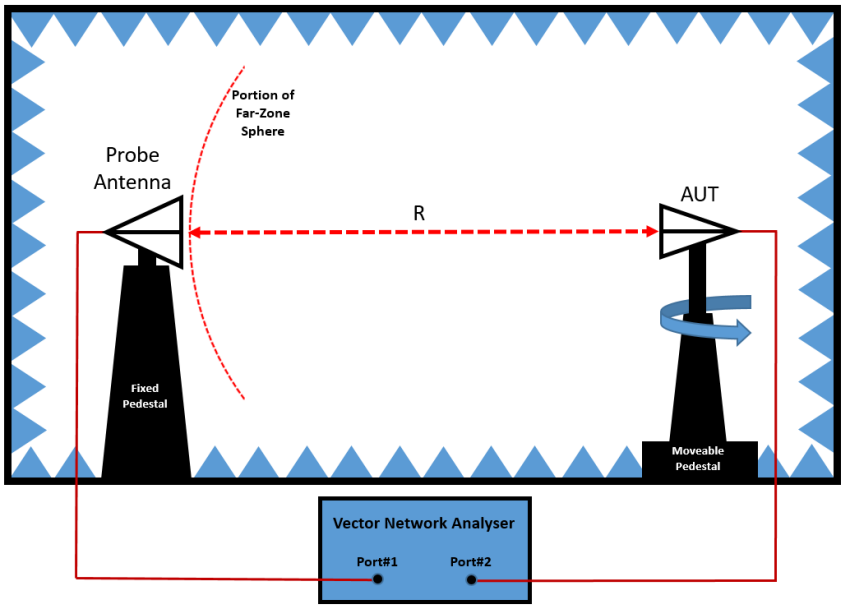

Fig.1.2-1 : Anechoic chamber with test configuration for direct measurement of the far-zone radiation pattern of an antenna-under-test (AUT).

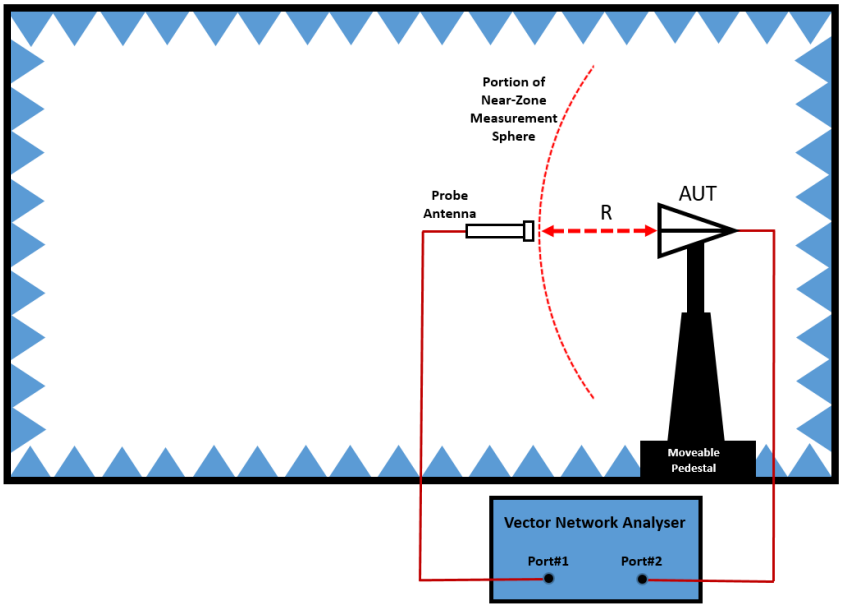

Fig.1.2-2 : Anechoic chamber with test configuration for indirect measurement ("near-field testing" approach) of the far-zone radiation pattern of an antenna-under-test (AUT).

1.3 OVERVIEW OF THE THESIS

Chapter 2 provides a review of NF antenna measurement techniques in just enough depth that we can sensibly place the contributions of this thesis in context, and so attempt to persuade the reader of its novelty and usefulness. It also summarizes the integral-equations (IE), and associated moment-method (MM) solution techniques, used in the computational electromagnetics (CEM) that will be utilized in this work. The latter is a vast subject that could fill a tome, and we therefore select and reference only those aspects that are needed to conduct the research described in this thesis. The true thesis contributions are contained in the remaining chapters. Chapter 3 proposes an approach for a new CEM-based NF-to-FF transformation that allows the near-field (NF) to be acquired on any rotationally symmetric[6] measurement surface, and not only a spherical one. Chapter 4 describes the numerical implementation of this idea. The proposed new approach is validated in Chapter 5. Chapter 6 highlights the contributions of the thesis and suggests some future work on the topic.

[6] Also called a "body of revolution (BOR)" surface.

CHAPTER 2
Review of Antenna Measurement, and Integral-Equation Moment-Method, Techniques

2.1 INTRODUCTION

The goal of this chapter is to review, and present in a consistent notation, some necessary theoretical background that will be essential in implementing the NF-to-FF transformation whose need was mentioned in Section 1.2, whose detail will be proposed in Section 3.2, which will be implemented, and validated in Chapter 5. Section 2.2 will interpret NF antenna measurement techniques as an application of the surface equivalence principle, in order to facilitate the discussion of the NF-to-FF transformation in Chapter 3. The proposed NF-to-FF transformation will involve the use of the moment method to compute the scattering from a perfectly conducting (PEC) rotationally symmetric object, modelled using an integral equation. The basic ideas of such integral equation modelling and moment method solution are therefore summarised in Section 2.3 in general terms. The details of the moment method formulation for the specific case of rotationally symmetric PEC objects are summarised quite completely in Section 2.4. It is the formulation that will be implemented in code in Chapter 4.

2.2 NEAR-FIELD MEASUREMENT TECHNIQUES : INTERPRETATION IN TERMS OF THE SURFACE EQUIVALENCE THEOREM

2.2.1 Surface Equivalence Theorem (Huygens' Principle)

All near-field (NF) antenna testing methods can be viewed as literal applications of a special case of the surface equivalence principle [HARR 61]. This special case can be stated as follows: Consider the situation in Fig.2.2-1(a) and (b) which shows impressed (actual) sources[7] and all scattering objects lying entirely within a fictitious closed surface S_{eq}, which can be of arbitrary shape. These sources provide the true actual fields $\{\bar{E}(\bar{r}), \bar{H}(\bar{r})\}$ both inside and outside of S_{eq}. The surface equivalence theorem says that if we place electric current density[8]

[7] In other words, the AUT.

[8] By $\bar{E}(S_{eq})$ we mean the electric field at points on S_{eq}, and so forth.

$$\bar{J}_s = \hat{n}(S_{eq}) \times \bar{H}(S_{eq}) \tag{2.2-1}$$

and

$$\bar{M}_s = -\hat{n}(S_{eq}) \times \bar{E}(S_{eq}) \tag{2.2-2}$$

on S_{eq} as shown in Fig.2.2-1(d), and turn off the actual sources within S_{eq}, then these surface current densities $\bar{J}_s$ and $\bar{M}_s$ (radiating together in free space[9]) will give us the actual fields external to S_{eq} and zero fields internal to S_{eq}. In a NF measurement system we could[10] measure $\hat{n} \times \bar{H}$ and $-\hat{n} \times \bar{E}$ over some selected surface S_{eq}, thus obtaining $\bar{J}_s$ and $\bar{M}_s$, and then the fields external to S_{eq} could be obtained using the free-space Green's functions as

$$\bar{E}(\bar{r}) = -j\omega\mu_0 \iint_{S_{eq}} \tilde{G}_{\text{ee}}^{\text{fs}}(\bar{r}, \bar{r}') \cdot \bar{J}_s(\bar{r}')\, dS' + \iint_{S_{eq}} \tilde{G}_{\text{em}}^{\text{fs}}(\bar{r}, \bar{r}') \cdot \bar{M}_s(\bar{r}') dS' \tag{2.2-3}$$

The $\bar{J}_s$ and $\bar{M}_s$ must now be viewed as the impressed[11] current densities. In (2.2-3), $\tilde{G}_{\text{ee}}^{\text{fs}}(\bar{r}, \bar{r}')$ is the free-space dyadic Green's function that gives the electric field due to an electric current density $\bar{J}_s$, whereas $\tilde{G}_{\text{em}}^{\text{fs}}(\bar{r}, \bar{r}')$ gives the electric field due to a magnetic current density $\bar{M}_s$. The superscript "fs" is meant to emphasize the fact that these are the Green's functions for these surface current densities radiating in a free-space environment; there are no longer any objects present anywhere. These free-space Green's functions are known [VOLA 12].

Since the field within S_{eq} is zero, we can fill the entire volume within S_{eq} with a perfect conductor without influencing the field external to S_{eq}. We therefore do this[12] until we have the situation shown in Fig.2.2-2(a), where S_{eq} now coincides snugly with a perfectly conducting (PEC) surface. The situation is now one of impressed sources $\bar{J}_s$ and $\bar{M}_s$ tangential to a PEC surface S_{eq}. The reciprocity theorem of electromagnetic theory [HARR 61] can be used to

[9] In other words, all material objects inside S_{eq} are effectively removed.

[10] In practice (as will be discussed shortly) we want to measure $-\hat{n} \times \bar{E}$ only, but for the time being please read on.

[11] By "impressed" is meant that these are unaffected by the electromagnetic fields themselves, and that if all the impressed sources were turned off there would be no fields whatsoever.

[12] It is entirely a "thought-experiment", and so no practicalities need be considered.

show[13] that $\bar{J}_s$ does not radiate at all. We now only have impressed $\bar{M}_s$ radiating, ***but it does so in the presence of a PEC object*** whose surface is S_{eq}; ***it is not radiating in free space***. If we wish to find the fields $\{\bar{E}(\bar{r}), \bar{H}(\bar{r})\}$ due to this $\bar{M}_s$ we would in principle need to evaluate

$$\bar{E}(\bar{r}) = \iint_{S_{eq}} \tilde{G}_{\text{em}}^{\text{PEC}}(\bar{r}, \bar{r}') \cdot \bar{M}_s(\bar{r}') dS' \tag{2.2-4}$$

where $\tilde{G}_{\text{em}}^{\text{PEC}}(\bar{r}, \bar{r}')$ is now not the known free space Green's function $\tilde{G}_{\text{ee}}^{\text{fs}}(\bar{r}, \bar{r}')$, but instead the Green's function for a magnetic current density $\bar{M}_s$ radiating **in the presence of a PEC object of shape** S_{eq}. An analytical form for this Green's function is in general **not known**, except in some circumstances where S_{eq} is a special shape.

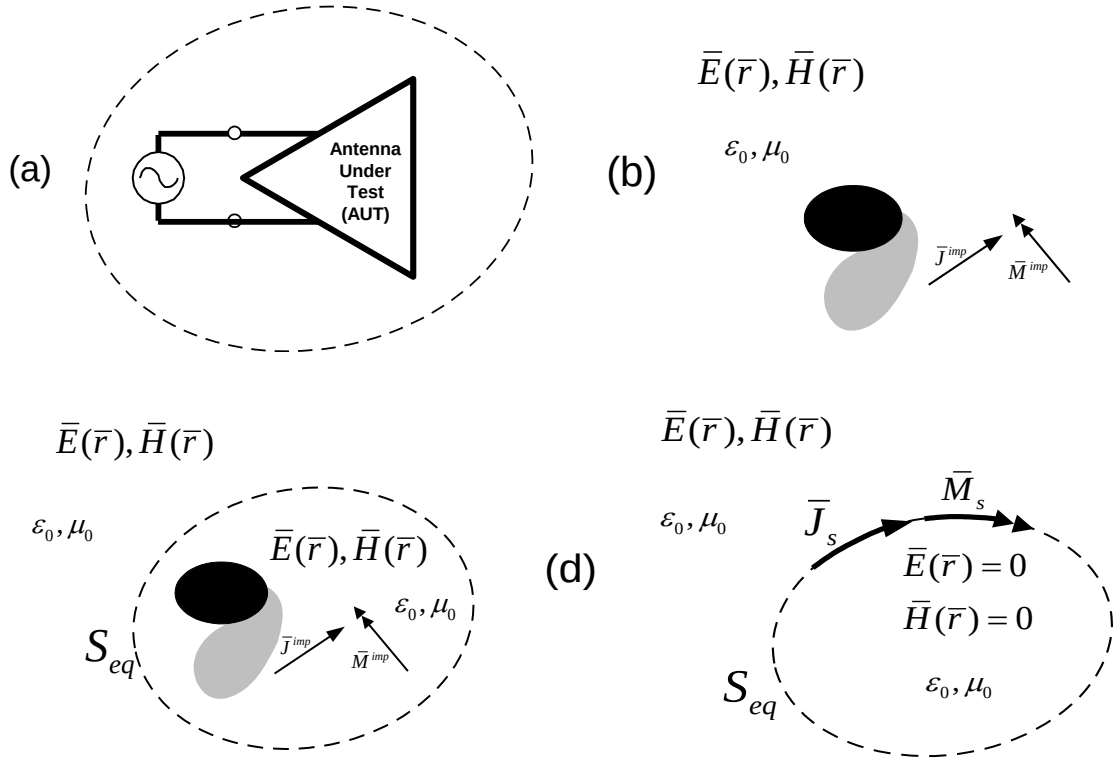

Fig.2.2-1 : (a). Original physical problem with surface on which the near-fields are measured; (b). Abstract view of the original problem (c). Original physical problem with closed surface S_{eq} selected; (d). Problem equivalent to original problem in region exterior to S_{eq}.

[13] An impressed electric current density placed tangential to a PEC surface does not radiate.

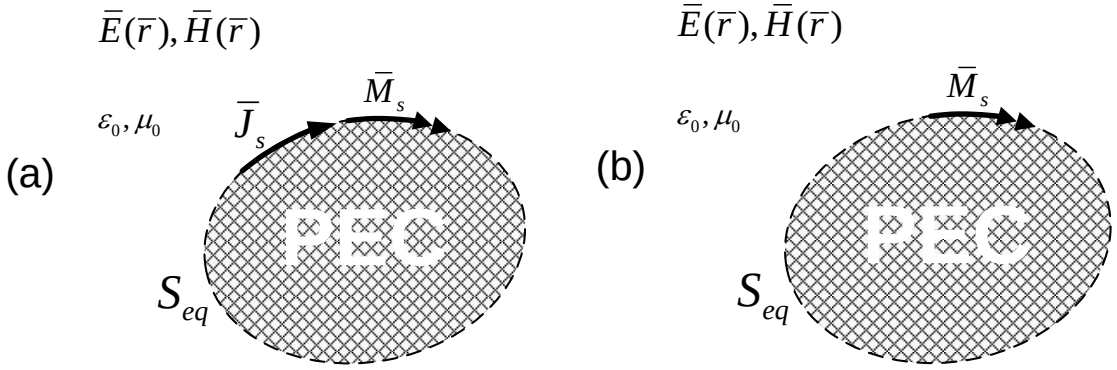

Fig.2.2-2 : (a). The situation of Fig.2.3-1(d) with the volume internal to S_{eq} filled with PEC; (b). The situation in (a) with the realisation that the $\bar{J}_s$ in (a) will not radiate and so does not contribute to the radiated fields.

In Fig.2.2-3, shown below, the logical sequence is graphically summarized.

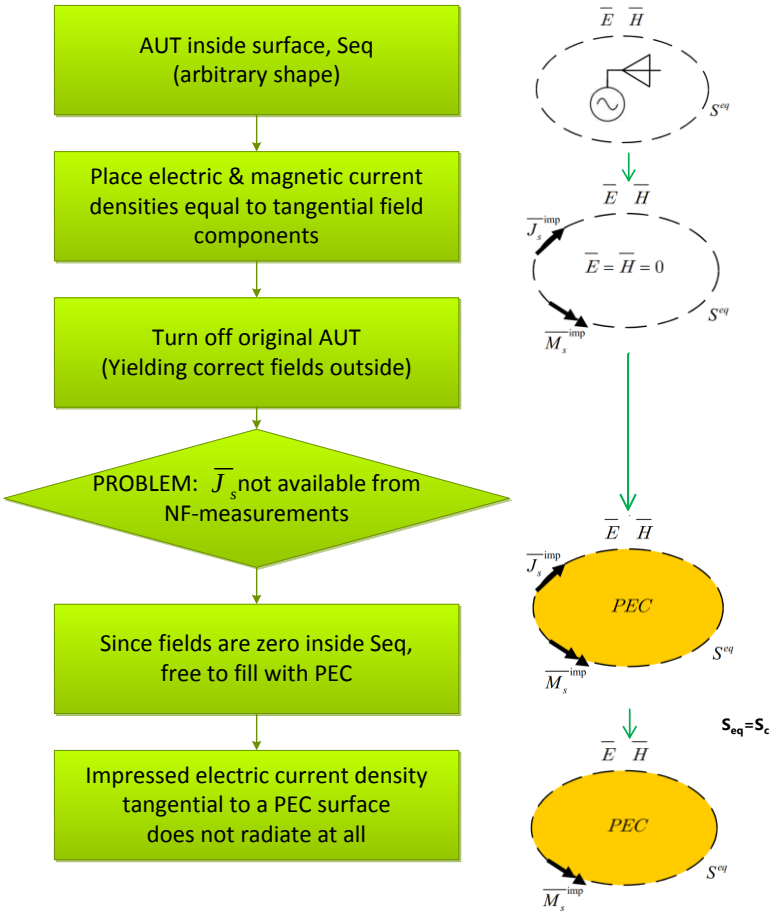

Fig.2.2-3 : Flow-chart indicating sequential application of surface equivalence and the equivalent problem that results with the realization that the $\bar{J}_s$ will not radiate, nor does it contribute to the radiated fields.

2.2.2 Near-Field Methods from a Surface Equivalence Theorem Viewpoint

In the case where S_{eq} is a spherical surface this $\tilde{G}_{\text{em}}^{\text{PEC}}(\bar{r},\bar{r}')$ can in principle be written as an infinite summation of spherical wave modes [PARI 18]. Evaluation of (2.2-4) reduces to expressing $\bar{E}(\bar{r})$ as a summation of the spherical modes, the coefficients of the expansion being dependent on the spatial distribution of $\bar{M}_s$ on the spherical surface.

In spherical near-field measurements we probe the quantity $\hat{n}(S_{meas})\times\bar{E}(S_{meas})$ over a measurement surface S_{meas}, which is now the symbol we will use in place of S_{eq}. We then "convert" this to a magnetic current density

$$\bar{M}_s^{NF} = -\hat{n}(S_{meas})\times\bar{E}(S_{meas}) \tag{2-2-5}$$

at all points on S_{meas}. This is then viewed as an impressed magnetic surface current density. The field (eg. far-zone field) at any observation point exterior to S_{meas} can then be found by evaluating the integral[14]

$$\bar{E}(\bar{r}) = \oiint_{S_{meas}} \tilde{G}_{\text{em}}^{\text{PEC}}(\bar{r},\bar{r}')\cdot\bar{M}_s^{NF}(\bar{r}')\,dS' \tag{2-2-6}$$

with $\tilde{G}_{\text{em}}^{\text{PEC}}(\bar{r},\bar{r}')$ the Green's function for an impressed magnetic current density radiating in the presence of a PEC surface that is spherical. In particular, we are interested in $\bar{E}(S_\infty)$.

2.3 INTEGRAL EQUATIONS FOR ELECTROMAGNETIC SCATTERING FROM PREFECTLY CONDUCTING (PEC) OBJECTS

2.3.1 Goals of the Present Section : Integral Equations

The electric field integral equation (EFIE) for impressed current densities radiating in the presence of a PEC object is derived in Section 2.3.2. Section 2.3.3 derives the magnetic field integral equation (MFIE) for the same situation. Unfortunately, for a closed PEC object, neither the EFIE nor the MFIE provide unique solutions at all frequencies. This problem will be a serious limitation in the present work, and so it will be necessary to use the combined field

[14] This is what is in effect done, although the actual numerical route followed might not show this explicitly.

integral equation (CFIE), which is not tainted by such non-uniqueness problems. The CFIE is derived in Section 2.3.4. Some of the material in this section has been gleaned from [MCNA 16].

2.3.2 The Electric Field Integral Equation (EFIE) for Scattering by PEC Objects

The derivation of the general form of the EFIE for conducting objects is relatively straightforward. We consider the case where the impressed source consists of electric and magnetic current densities, $\bar{J}^{imp}$ and $\bar{M}^{imp}$ respectively, as shown in Fig.2.3-1. We have an arbitrarily shaped perfectly conducting (PEC) scatterer, situated in free space. The surface of the scatterer is denoted S_c. Although we show a single scatterer, there could be more than one, with S_c the union of the surfaces of the individual scatterers. The formulation to follow is the same irrespective of the number of scatterers. The impressed electric $\bar{J}^{imp}(\bar{r})$ and magnetic $\bar{M}^{imp}(\bar{r})$ current densities exist exterior to, or on, surface S_c. In the absence of the scatterer the impressed source generate fields $\bar{E}^{inc}(\bar{r})$ and $\bar{H}^{inc}(\bar{r})$ at all points $\bar{r}$ in free space; these are of course the incident fields. Recall that an incident field is by definition that which exists when the object identified as the scatterer is removed, and that this incident field exists at all points (even within the scatterer). Because of the incident field there will be induced currents on the scatterer which will give rise to additional electromagnetic fields, namely the scattered fields $\bar{E}^{scat}(\bar{r})$ and $\bar{H}^{scat}(\bar{r})$. The total field will at all observation points[15] $\bar{r}$ be the sum of the incident and scattered fields, namely

$$\bar{E}(\bar{r}) = \bar{E}^{inc}(\bar{r}) + \bar{E}^{scat}(\bar{r}) \qquad (2.3\text{-}1)$$

$$\bar{H}(\bar{r}) = \bar{H}^{inc}(\bar{r}) + \bar{H}^{scat}(\bar{r}) \qquad (2.3\text{-}2)$$

In order to apply the surface equivalence theorem we place our "equivalence surface" S_{eq} so that it completely encloses S_c (but not the impressed sources) and then shrink it until it coincides with S_c, as shown in Fig.2.3-2. Hereafter we will refer only to S_c since it is identical to S_{eq}.

[15] Both inside and outside the PEC scatterer.

The theorem then allows us to replace the original problem with an equivalent one as follows. If we place equivalent surface current densities

$$\bar{J}_s(\bar{r}_s) = \hat{n}(\bar{r}_s) \times \bar{H}(S_c^+) \tag{2.3-3}$$

$$\bar{M}_s(\bar{r}_s) = -\hat{n}(\bar{r}_s) \times \bar{E}(S_c^+) \tag{2.3-4}$$

at all points $\bar{r}_s$ on S_c, then there will be zero total field inside S_c, and the correct total field exterior to the surface S_{eq}. But since S_c coincides everywhere with a perfectly conducting surface, we know that $\hat{n}(\bar{r}_s) \times \bar{E}(S_c^+) = 0$ everywhere on S_c, and so $\bar{M}_s(\bar{r}_s) = 0$. Thus we have an equivalent electric current density only in this case where S_{eq} is chosen to coincide with S_c.

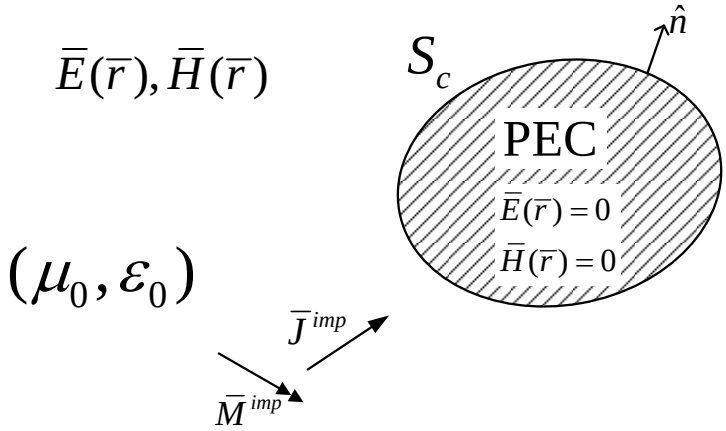

Fig.2.3-1 : Representation of the problem consisting of an impressed magnetic current density radiating in the presence of a PEC object of arbitrary shape.

The total field will be zero everywhere inside S_c; in other words things will be such that the scattered field will be precisely the negative of the incident field at all points within S_c. We can therefore remove the conducting material within S_c and replace it with free space, which means that the current density $\bar{J}_s$ radiates in free space, since we said that we had free space external to S_c to start with and now have it within S_c as well. Use of the equivalence theorem has thus allowed us to replace the original problem statement in Fig.2.3-1 by the equivalent problem in Fig.2.3-3, namely an electric current density $\bar{J}_s(\bar{r}_s)$ on a surface S_c, radiating in an unbounded medium.

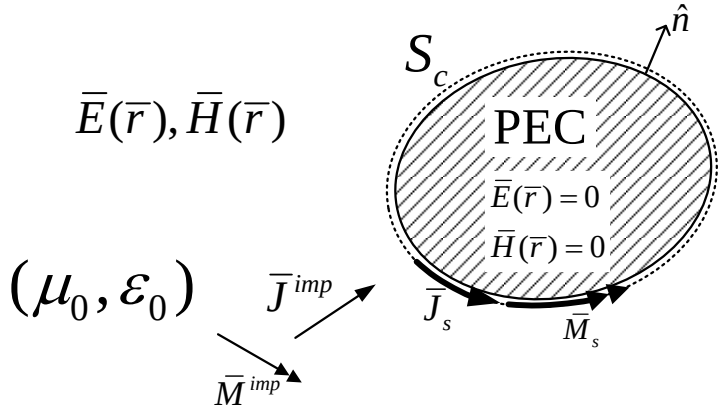

Fig.2.3-2 : Application of the surface equivalence theorem to the problem in Fig.2.3-1.

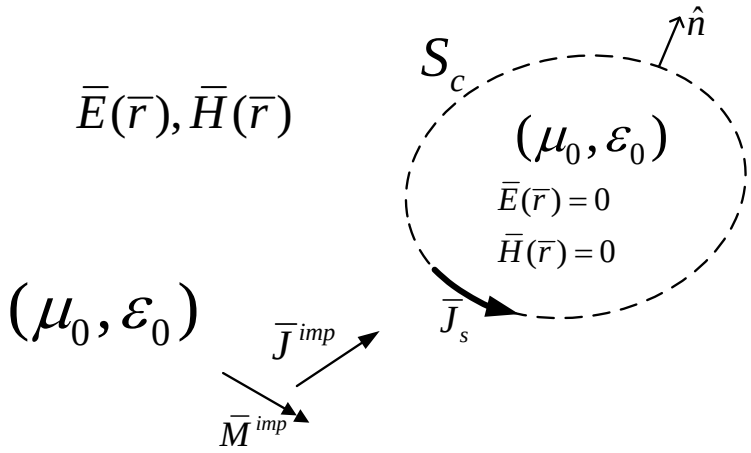

Fig.2.3-3 : Problem equivalent to the problem in Fig.2.3-1, but only in the region external to the conducting object.

The impressed magnetic current density generates incident fields everywhere, both inside and outside S_c. The sum of the incident and scattered fields will give the total fields everywhere, as expressed in (2.3-1) and (2.3-2). This $\bar{J}_s$ will generate the scattered fields $\bar{E}^{scat}$ and $\bar{H}^{scat}$ everywhere, both inside and outside the surface S_c. It is extremely important to remember that although the current density $\bar{J}_s$ is given in terms of the total field $\bar{H}\left(S_c^+\right)$, it does not generate the total fields $\bar{E}$ and $\bar{H}$, but only the scattered fields $\bar{E}^{scat}$ and $\bar{H}^{scat}$.

The EFIE is a statement of the boundary condition that the total tangential electric field must vanish at all points on the surface of a perfect electric conductor, namely

$$\hat{n}(\bar{r})\times\bar{E}(\bar{r})=0 \qquad \bar{r}\in S_c \tag{2.3-5}$$

which can be rewritten as

$$\hat{n}(\bar{r})\times\left\{\bar{E}^{inc}(\bar{r})+\bar{E}^{scat}(\bar{r})\right\}=0 \qquad \bar{r}\in S_c \tag{2.3-6}$$

and thereafter as

$$\hat{n}(\bar{r})\times\bar{E}^{scat}(\bar{r})=-\hat{n}(\bar{r})\times\bar{E}^{inc}(\bar{r}) \qquad \bar{r}\in S_c \tag{2.3-7}$$

Since $\bar{E}^{scat}$ is due to $\bar{J}_s$ on S_c, we can write it symbolically as

$$\bar{E}^{scat}\left\{\bar{J}_s,\bar{r}\right\} \tag{2.3-8}$$

In other words, it is "$\bar{E}^{scat}$, due to $\bar{J}_s$, evaluated at $\bar{r}$". The EFIE is thus

$$\underbrace{-\hat{n}(\bar{r})\times\bar{E}^{scat}\left\{\bar{J}_s,\bar{r}_s\right\}}_{\mathcal{L}_E\left\{\bar{J}_S\right\}}=\hat{n}(\bar{r})\times\bar{E}^{inc}(\bar{r}) \qquad \bar{r}\in S_c \tag{2.3-9}$$

$\bar{E}^{scat}\left\{\bar{J}_s,\bar{r}_s\right\}$ will of course be an integral involving unknown $\bar{J}_s$ and a Green's function, whereas $\hat{n}(\bar{r})\times\bar{E}^{inc}(\bar{r})$ is known.

2.3.3 The Magnetic Field Integral Equation (MFIE) for Scattering by PEC Objects

The statement of the original problem is the same as that in Fig.2.3-1, and the equivalent problem of interest the same as shown in Fig.2.3-3. In this instance we wish to derive the magnetic field integral equation (MFIE) for the unknown[16] equivalent current density $\bar{J}_s$. In order to do this we apply the boundary condition for the tangential magnetic field at the surface of a PEC, namely

$$\lim_{\underline{r}^+\to\underline{r}}\left\{\hat{n}(\bar{r})\times\bar{H}_1(\bar{r}^+)\right\}=\bar{J}_s(\bar{r}) \qquad \bar{r}\in S_c \tag{2.3-10}$$

which we rewrite as

$$\hat{n}(S_c)\times\bar{H}\left(S_c^+\right)=\bar{J}_s(S_c) \tag{2.3-11}$$

[16] The unknown quantity is the **same** electric surface current density that is the unknown in the EFIE.

S_c^+ is a surface "just outside S_c", and the symbol implies a limiting process "as the point approaches S_c from outside S_c". We use the fact that, at all points $\bar{r}$, both on and off the surface S_c, we have $\bar{H}^{inc}(\bar{r}) + \bar{H}^{scat}(\bar{r}) = \bar{H}(\bar{r})$. Therefore (2.3-11) is

$$\hat{n}(S_c) \times \left\{ \bar{H}^{inc}(S_c^+) + \bar{H}^{scat}(S_c^+) \right\} = \bar{J}_s(S_c) \tag{2.3-12}$$

Once more recall that $\bar{H}^{inc}$ is the field due to the impressed source when the PEC object is removed. Hence all its components are continuous everywhere, and thus its components tangential to S_c are continuous across S_c. It is the tangential component of $\bar{H}^{scat}$ that is discontinuous across S_c as the observation point moves from S_c^+ to S_c^-. So we can write (2.3-12) as[17]

$$\underbrace{\bar{J}_s(S_c) - \hat{n}(S_c) \times \bar{H}^{scat}\left\{S_c^+, \bar{J}_s\right\}}_{\mathcal{L}_H\left\{\bar{J}_s\right\}} = \hat{n}(S_c) \times \bar{H}^{inc}(S_c) \tag{2.3-13}$$

We have written $\bar{H}^{scat}(S_c^+)$ as $\bar{H}^{scat}\left\{S_c^+, \bar{J}_s\right\}$ to emphasize that it will be an integral involving unknown $\bar{J}_s$ and a free space Green's function. Expression (2.3-13) is the MFIE applying to a PEC object.

[17] Carefully note the arguments of each of the quantities in (6.5-4).

2.3.4 Non-Uniqueness of the Solutions to the EFIE and MFIE[18]

A unique solution to Maxwell's equations (that is for the fields, and hence conduction currents), subject to the continuity and radiation conditions, exists at all frequencies for the problem represented in Fig.2.3-1, the so-called exterior problem. However, what we often forget is that, just because we have derived some integral equation (eg. EFIE) for scattering from a PEC object using one of the continuity conditions (eg. $\hat{n}\times\bar{E}=0$), this does not mean that the other continuity condition (eg. $\hat{n}\times\bar{H}=\bar{J}_s$) on the object is automatically satisfied. As a result, the EFIE and MFIE *do not* provide unique solutions to the $\bar{J}_s$ for this class of problem at all frequencies. Paraphrasing [YAGH 81], although Maxwell's equations and continuity/radiation conditions are used to derive the EFIE and MFIE, it must be concluded that the EFIE or MFIE, when applied in the exterior problem, are not equivalent to Maxwell's equations plus continuity/radiation conditions. In other words,

- At the non-uniqueness frequencies (and only at these frequencies) the continuity condition $\hat{n}\times\bar{H}=\bar{J}_s$ on S_c is not enforced by the EFIE.

- At the non-uniqueness frequencies (and only at these frequencies) the continuity condition $\hat{n}\times\bar{E}=0$ on S_c is not enforced by the MFIE.

2.3.5 The Combined Field Integral Equation (CFIE) for Scattering by PEC Objects

If we have found the correct solution $\bar{J}_s$ for a particular problem then it must of course satisfy both the EFIE and the MFIE. In other words, $\bar{J}_s$ must cause both

$$\mathcal{L}_E\left\{\bar{J}_s\right\}=\hat{n}\left(\bar{r}\right)\times\bar{E}^{inc}\left(\bar{r}\right) \qquad \bar{r}\in S_c \qquad (2.3\text{-}14)$$

and

$$\mathcal{L}_H\left\{\bar{J}_s\right\}=\hat{n}\left(\bar{r}\right)\times\bar{H}^{inc}\left(\bar{r}\right) \qquad \bar{r}\in S_c \qquad (2.3\text{-}15)$$

to be satisfied. This at once means that it must satisfy a linear combination of (2.3-15) and (2.3-16), namely

[18] This section has been paraphrased from [McNA 16].

$$\mathcal{L}_H\left\{\bar{J}_s\right\}+\left(\frac{\alpha}{\eta_0}\right)\mathcal{L}_E\left\{\bar{J}_s\right\}=\hat{n}\left(\bar{r}\right)\times\bar{H}^{inc}\left(\bar{r}\right)+\left(\frac{\alpha}{\eta_0}\right)\hat{n}\left(\bar{r}\right)\times\bar{E}^{inc}\left(\bar{r}\right)\qquad \bar{r}\in S_c \tag{2.3-16}$$

where α is a dimensionless constant to be selected "by the user", and $\eta_0=\sqrt{\mu_0/\varepsilon_0}$. The quantity η_0 is included in order that the linear combination in (2.3-17) represents the addition of quantities which have the same units. Expression (2.3-17) is the combined field integral equation (CFIE)[19]. The CFIE can be written in more compact operator notation as

$$\mathcal{L}_{CF}\left\{\bar{J}_s\right\}=\hat{n}\left(\bar{r}\right)\times\bar{H}^{inc}\left(\bar{r}\right)+\left(\frac{\alpha}{\eta_0}\right)\hat{n}\left(\bar{r}\right)\times\bar{E}^{inc}\left(\bar{r}\right)\qquad \bar{r}\in S_c \tag{2.3-17}$$

where

$$\mathcal{L}_{CF}\left\{\bar{J}_s\right\}=\mathcal{L}_H\left\{\bar{J}_s\right\}+\left(\frac{\alpha}{\eta_0}\right)\mathcal{L}_E\left\{\bar{J}_s\right\} \tag{2.3-18}$$

It can be shown that (unlike the EFIE and MFIE) the combined field integral equation (CFIE) does indeed have a unique solution [YAGH 81] at all frequencies for $\bar{J}_s$ whenever we choose constant α to be a positive real number.

2.3.6 Numerical Solution of the Integral Equations Using the Moment Method : General Ideas

The method of moments (MM) is a numerical method used to solve IEs of the type mentioned in the previous sub-sections [HARR 68] [PETE 97] [VOLA 12]. It does so by converting the IE into a matrix equation (in other words by discretizing the IE) that can be solved numerically. The basics of the MM are easily grasped by considering a 1D case, with a typical IE of the form [MCNA 16]

$$\int_a^b f(x')G\left(x,x'\right)dx'=g\left(x\right)\qquad a\le x\le b \tag{2-3-19}$$

[19] We note in passing that, with the EFIE, MFIE and CFIE for perfectly conducting bodies that we have derived, the electric current density $\bar{J}_s$, although arising from the application of the surface equivalence principle which deals in general with equivalent current quantities, has physical significance here (since the surface S_{eq} coincides with the conductor surface S_c) in that it is the electric conduction current induced on the conducting body.

Quantity $f(x)$ is the unknown function (defined over the spatial domain $a \le x \le b$) we wish to determine, and would be an electric surface current density in the IE we will be solving in this thesis. The $G(x,x')$ is the kernel of the integral equation, which in the electromagnetics IEs mentioned earlier will be the free-space Green's function. Finally, $g(x)$ is a known as a source function that is responsible for there being a non-zero $f(x)$ at all, and in our case will be some aspect of the incident field due to some impressed source. In order to solve for the unknown $f(x)$, in the MM we expand it in terms of a set of N so-called expansion functions[20] $f_n(x)$ as

$$f(x) \approx \sum_{n=1}^{N} I_n \, f_n(x) \qquad (2\text{-}3\text{-}20)$$

After (2-3-20) has been substituted into (2-2.3-19) the IE in (2-3-19) becomes

$$\int_a^b \left(\sum_{n=1}^{N} I_n f_n(x') \right) G(x,x')\, dx' \approx g(x) \qquad (2\text{-}3\text{-}21)$$

Integral operators are linear, and hence we can write (2-3-21) as

$$\sum_{n=1}^{N} I_n \left(\int_a^b f_n(x') G(x,x')\, dx' \right) \approx g(x) \qquad (2\text{-}3\text{-}22)$$

The only unknowns at this stage are the coefficients I_n; if these could be determined then they can be substituted into (2.3-22) to provide a numerical solution for the unknown quantity $f(x)$.

In order to actually reach a matrix equation to find these coefficients we define a set of N weighting functions $g_m(x)$. Although we are at liberty to select the weighting functions as we please, the collective wisdom of those working in computational electromagnetics is overwhelmingly in favour of selecting the weighting functions to be the complex conjugates of the expansion functions, a choice known as the Galerkin approach. We therefore set our weighting functions to be the complex conjugates of the expansion functions

$$\{g_1(x), g_2(x), ..., g_n(x), ..., g_N(x)\} = \{f_1^*(x), f_2^*(x), ..., f_n^*(x), ..., f_N^*(x)\} \qquad (2\text{-}3\text{-}23)$$

[20] In formulation a particular MM for a specific IE the expansion functions $f_n(x)$ have to be selected by "the user".

We next multiply both sides of (2.3-22) by each of the weighting functions $g_m(x)$ and integrate with respect to the spatial variable x the integral equation, so that for each weighting function we have

$$\sum_{n=1}^{N} I_n \underbrace{\left(\int_a^b \int_a^b f_n(x') G(x,x') g_m(x)\, dx' dx \right)}_{A_{mn}} \approx \underbrace{\int_a^b g\left(x\right) g_m(x) dx}_{B_m} \tag{2-3-24}$$

or in other words

$$\sum_{n=1}^{N} I_n \, A_{mn} \approx B_{\mathrm{m}} \tag{2-3-25}$$

For each value of index m this is a single linear equation with the coefficients $I_1, I_2, ..., I_n, ..., I_N$ as unknowns. Therefore, enforcing (2.3-25) for each value of m yields a matrix equation

$$\begin{bmatrix} A_{11} & \cdots & A_{1N} \\ \vdots & \ddots & \vdots \\ A_{N1} & \cdots & A_{NN} \end{bmatrix} \begin{bmatrix} I_1 \\ \vdots \\ I_N \end{bmatrix} = \begin{bmatrix} B_1 \\ \vdots \\ B_N \end{bmatrix} \tag{2.3-26}$$

where the column vector $\begin{bmatrix} I_1 & \cdots & I_N \end{bmatrix}^T$ is the set of previously unknown coefficients whose values we desired. The notation used in Section 2.4 that follows becomes more concise if we define some additional concepts and terminology.

For any two functions $h(x)$ and $s(x)$, the *symmetric product* over $a \le x \le b$ as defined as

$$\left\langle h(x), s(x) \right\rangle = \int_a^b h(x) s(x) dx \tag{2-3-27}$$

Next the integral equation (2.3-24) is written in operator notation as

$$\mathcal{L}\left\{ f(x) \right\} = g(x) \tag{2-3-28}$$

where the operator $\mathcal{L}\left\{...\right\}$ is defined by[21]

[21] It is understood that when a function is inserted into $\left\{...\right\}$ its spatial variable must be primed.

$$\mathcal{L}\{...\} = \int_a^b \{...\} G(x,x')\,dx' \qquad x \in [a,b] \tag{2-3-29}$$

After application of the MM, the operator matrix elements can then be concisely written as

$$A_{mn} = \left\langle \mathcal{L}\{ f_n(x)\}, g_m(x) \right\rangle \tag{2-3-30}$$

and the right hand side column vector terms as

$$B_m = \left\langle g(x), g_m(x) \right\rangle \tag{2-3-31}$$

The MM is a general methodology used to solve electromagnetics problems, and the details change depending on the formulation. The expansion functions can exist over discretized portion over the domain $a \le x \le b$ or possibly over the entire domain. As described in Section 2.4, in the MM application used in this thesis the expansion functions are a combination of these options. The properties of the expansion functions change depending on the application, and are especially dependent on the function being approximated.

2.4 NUMERICAL SOLUTION OF THE INTEGRAL EQUATIONS USING THE MOMENT METHOD : CUSTOMIZATION TO PEC BODIES OF REVOLUTION

2.4.1 Preliminary Remarks

Integral equation formulations for scattering from a PEC body-of-revolution (BOR) surface S_c, that implicitly account for the geometrical[22] rotational symmetry of the object, can be found in many references, including the following, which are the seminal references:

[MAUT 69] J.R.Mautz and R.F.Harrington, "Radiation and scattering from bodies of revolution", Appl. Sci. Res., Vol.20, pp.405-435, June 1969.

[MAUT 77] J.R.Mautz and R.F.Harrington, *H-Field, E-Field, and Combined-Field Solutions for Bodies of Revolution*, Tech. Report RADC-TR-77-109, Department of Electrical Engineering, Syracuse University, New York, March 1977.

[MAUT 78] J.R.Mautz and R.F.Harrington, "H-field, E-field, and combined-field solutions for bodies of revolution", AEÜ, Vol.32, No.4, pp.157-164, April 1978.

As stated in Section 1.3, the contribution of this thesis is firstly to devise a near-field to far-field (NF-to-FF) transformation that applies to any rotationally symmetric measurement surface, and not only to spheres. The second is the implementation of the transformation, and thirdly the demonstration of its correctness. It was not the intention of this research to improve on existing CEM methods for scattering from BOR objects[23]. The decision was therefore taken to select and implement, in a MATLAB environment, the particular BOR formulation provided in [MAUT 77] and [MAUT 78]. There is no reason to alter the notation used in these references in any major way[24], or to re-derive detailed expressions that are already available there. However, it is still important to grasp the complexity of the formulation, and to properly understand the mathematical operations needed for its implementation in Chapter 4. The key expressions of the formulation will therefore be written down here, and each identified by the corresponding one in [MAUT 77]. We believe that the clear summary given here provides a tutorial-like addition to

[22] Even though the associated equivalent currents and associated fields will *not* in general be rotationally symmetric.
[23] Improvements such as the more precise handling of Green's function singularities [VAES 12], or enhancing the computational efficiency, have been added since the above-listed work by Mautz and Harrington. However, these have been purely numerical, and the above-listed references remain the seminal ones that should not be considered "outdated".
[24] Some minor changes in notation will be made, but these will be easily recognised should the reader actually wish to consult [MAUT 78].

the three references mentioned above (which are very compactly written), and sufficient detail to connect seamlessly with the implementation in Chapter 4. There will be some embellishment of the expressions constituting the formulation that aids in its understanding (eg. we often show the functional dependence of various quantities explicitly because this helps with the numerical implementation). We will also describe matters in a manner that is somewhat 'customized' for the particular application this thesis has in mind. The outline of the formulation will be done using expressions extracted from the references [MAUT 77] and [MAUT 78] wherever possible; all expressions that appear in these references will be given a number as per this thesis, with the corresponding number in these references alongside it.

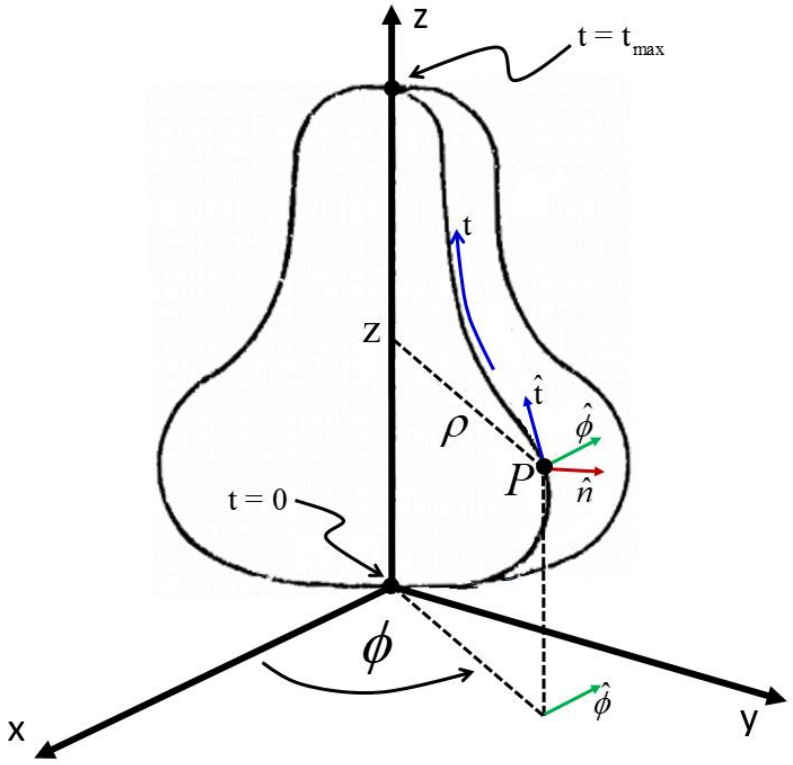

Fig.2.4-1 : Body-of-revolution (BOR) surface S_c.

2.4.2 Geometry & Coordinate System

A body-of-revolution (BOR) is completely defined if we specify a generating curve, and then rotate it around the axis of symmetry of the BOR. The lines of longitude are thus also defined by the generating curve except that each has a different value of azimuthal angle ϕ. A general point

P on the BOR surface S_c can be identified either in terms of its rectangular coordinates (x, y, z) or equivalently its cylindrical coordinates (ρ, ϕ, z), as Fig.2.4-1 indicates. The point P can also be specified by its distance along the generating curve and its azimuthal location, namely (t, ϕ). At each such point on the BOR surface a triad of orthogonal local unit vectors can be defined, related as

$$\begin{aligned} \hat{n} &= \hat{\phi} \times \hat{t} \\ \hat{\phi} &= \hat{t} \times \hat{n} \\ \hat{t} &= \hat{n} \times \hat{\phi} \end{aligned} \tag{2.4-1}$$

as can be seen by inspection of Fig.2.4-1. Since $\rho(t)$ and $z(t)$ are known once the BOR is specified, unit vector $\hat{t}$ can be found as

$$\hat{t} = \frac{\bar{t}}{|\bar{t}|} \qquad \bar{t} = \frac{\partial \rho}{\partial t}\hat{\rho} + \frac{\partial z}{\partial t}\hat{z} \tag{2.4-2}$$

The angle between $\hat{t}$ and $\hat{z}$ at point P is then

$$\nu = \cos^{-1}\left(\hat{z} \cdot \hat{t}\right) \tag{2.4-3}$$

In terms of rectangular components, it can be shown that [MAUT 69]

$$\hat{t} = \sin\nu\cos\phi\,\hat{x} + \sin\nu\cos\phi\,\hat{y} + \cos\nu\,\hat{z} = t_x\hat{x} + t_y\hat{y} + t_z\hat{z} \tag{2.4-4}$$

$$\hat{n} = \cos\nu\,\cos\phi\,\hat{x} + \cos\nu\,\sin\phi\,\hat{y} - \sin\nu\,\hat{z} = n_x\,\hat{x} + n_y\,\hat{y} + n_z\,\hat{z} \tag{2.4-5}$$

$$\hat{\rho} = c\cos\phi\,\hat{x} + \sin\phi\,\hat{y} = \rho_x\,\hat{x} + \rho_y\hat{y} \tag{2.4-6}$$

and

$$\hat{\phi} = \phi_x\hat{x} + \phi_y\hat{y} + \phi_z\hat{z} \tag{2.4-7}$$

2.4.3 Meshing of the BOR Generating Curve

The nature of the NF-to-FF transformation is such that all the BOR objects of interest will have a "north and south pole". In other words their generating curves all start and end on the z-axis. A set of points $\left(\rho_i^-, z_i^-\right)$, $i = 1,2,\ldots,N_P$ lie[25] on the generating curve of the BOR, with $\left(\rho_1^-, z_1^-\right)$ and $\left(\rho_{N_P}^-, z_{N_P}^-\right)$ at the poles. We will call these the BOR nodes. The PEC-BOR is then defined by connecting the points $\left(\rho_i^-, z_i^-\right)$ by straight lines, thus forming a frustum representation of the BOR, as depicted in Fig.2.4-2. These straight line sections (that is, the BOR segments) need not all be of the same length.

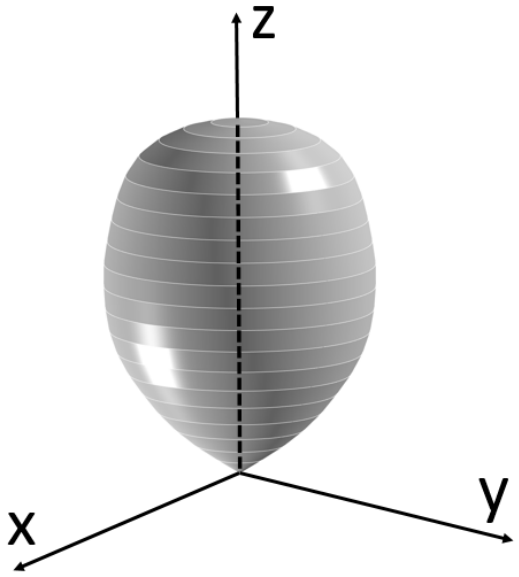

Fig.2.4-2 : Frustum representation of a complete body-of-revolution (BOR) surface.

2.4.4 Representation of the Unknown Surface Current Density $\bar{J}_S$: Broad Comments

With reference to Fig.2.4-1, the current density on the BOR object can be written in terms of two components, namely $J_t(t,\phi)$ and $J_\phi(t,\phi)$. The ϕ-dependence is represented by complex Fourier series type expansion functions of the form $e^{-jm\phi}$ for integer m ranging from $-\infty$ through zero to $+\infty$. We will refer to these as the BOR harmonics. The t-dependence is

[25] In [MAUT 77] symbol P is used instead of N_P but is also used to denote a general point. This can easily cause confusion. Hence our use of N_P.

represented by more conventional sub-domain expansion functions, namely overlapping triangular functions, to be discussed in the next section[26]. The same thing is done for the ϕ-dependence and t-dependence of the weighting functions. The final discretized form of the IE then (in principle) becomes [MAUT 69] an infinite set of uncoupled matrix equations, one matrix equation for each of the BOR harmonics. These matrix equations are uncoupled because of the selection of the complex Fourier series type expansion function to represent the ϕ-dependence. The details will next be given.

2.4.5 Expansion Functions for the Unknown Surface Current Density $\bar{J}_s$

The surface current density, at a point $(t,\phi) \in S_c$ is expanded as

$$\bar{J}_s(t,\phi) = \sum_{n=-N_h}^{N_h} \sum_{j=1}^{N_t} \left\{ I_{nj}^t \bar{J}_{nj}^t(t,\phi) + I_{nj}^{\phi} \bar{J}_{nj}^{\phi}(t,\phi) \right\} \qquad (2.4\text{-}8) \quad \text{[MAUT 77, Eq.(12)]}$$

where[27] the *j*-th expansion functions are

$$\bar{J}_{nj}^t = \hat{t}\, f_j(t) e^{jn\phi} \qquad (2.4\text{-}9) \quad \text{[MAUT 77, Eq.(13)]}$$

and

$$\bar{J}_{nj}^{\phi} = \hat{\phi} f_j(t) e^{jn\phi} \qquad (2.4\text{-}10) \quad \text{[MAUT 77, Eq.(14)]}$$

Quantity $f_j(t)$ is related to the *j*-th triangle function $T_j(t)$ by

$$f_j(t) = \frac{T_j(t)}{\rho} \qquad (2.4\text{-}11) \quad \text{[MAUT 69, Eq.(30)]}$$

In other words, the portion $f_j(t)$ of the overall expansion function is a triangle function divided by the BOR object's cylindrical coordinate $\rho(t)$. There is a triangle function associated with each BOR node. Each triangle occupies four BOR segments, and so many overlap. Each $T_j(t)$, as well as its spatial derivative, are approximated by four weighted 'pulses', one per each of the

[26] Using Fourier series with respect to both t and ϕ will imply that entire domain periodic functions would need to be defined for each different BOR. This would be extremely difficult, if not impossible, to do. The approach used in this thesis would then lose its generality.

[27] It is understood that the *j* in the exponential function is not the index *j* but $j = \sqrt{-1}$.

four segments occupied by the triangle function, when then form part of an integrand of an integral that is to be computed numerically. This is illustrated in part of Appendix F.

2.4.6 Weighting Functions

A Galerkin approach is used, and hence the *i*-th weighting functions are

$$\bar{W}_{mi}^{t} = \hat{t}\, f_i(t) e^{-jm\phi} \qquad \text{(2.4-12)} \quad \text{[MAUT 77, Eq.(15)]}$$

and

$$\bar{W}_{mi}^{\phi} = \hat{\phi} f_i(t) e^{-jm\phi} \qquad \text{(2.4-13)} \quad \text{[MAUT 77, Eq.(16)]}$$

Each triangle function forming part of the above weighting functions is approximated by four weighted delta-functions, one per each of the four segments occupied by the triangle function of the particular weighting function, when forming part of an integrand of an integral that needs to be numerically evaluated.

2.4.7 Discretized MFIE

Application of the method of moments to the MFIE as customized to a PEC object that is a BOR results in the set of matrix equations (one for each BOR harmonic[28])

$$\begin{bmatrix} [Y_n^{tt}] & [Y_n^{t\phi}] \\ [Y_n^{\phi t}] & [Y_n^{\phi\phi}] \end{bmatrix} \begin{bmatrix} [I_n^{t}] \\ [I_n^{\phi}] \end{bmatrix} = \begin{bmatrix} \left[\mathbb{I}_n^{t}\right] \\ \left[\mathbb{I}_n^{\phi}\right] \end{bmatrix}; \quad n = 0, \pm 1, \pm 2, \ldots \qquad \text{(2.4-14)} \quad \text{[MAUT 77, Eq.(17)]}$$

Computational economy follows from the fact that

$$Y_{-n}^{tt} = Y_n^{tt} \qquad \text{(2.4-15a)} \text{ [MAUT 77, Eq.102]}$$

$$Y_{-n}^{t\phi} = -Y_n^{\phi t} \qquad \text{(2.4-15b)} \text{ [MAUT 77, Eq.102]}$$

$$Y_{-n}^{\phi t} = -Y_n^{\phi t} \qquad \text{(2.4-15c)} \text{ [MAUT 77, Eq.102]}$$

[28] This is the beauty of the BOR formulation. Instead of a single enormous matrix equation, we have several smaller matrix equations, one for each BOR harmonic. These can be solved in parallel, since they are uncoupled. It is the orthogonality of the Fourier-like exponential functions used in the expansion and weighting functions that has resulted in this.

$$Y_{-n}^{\phi\phi} = Y_n^{\phi\phi} \qquad \text{(2.4-15d)} \text{ [MAUT 77, Eq.102]}$$

Once these sub-matrices have been evaluated for $n = 0,1,2,.....,N_h$ they are at once known for $n = -1,-2,.....,-N_h$. Because there are N_t expansion functions along the generatrix, each $[Y_n^{pq}]$ is a square sub-matrix of size $N_t \times N_t$.

Symbol $[I_n^t]$ represents a column vector of coefficients I_{nj}^t ($j = 0,1,2,.....,N_t$) of the expansion functions of the t-directed current density, whereas $[I_n^\phi]$ is the same for coefficients I_{nj}^ϕ of the $\hat{\phi}$-directed current density, of the n-th BOR harmonic.

The terms in the column vectors $\left[\mathbb{I}_n^t\right]$ and $\left[\mathbb{I}_n^\phi\right]$ of excitation coefficients on the right hand side of (2.4-14) are[29]

$$\mathbb{I}_{ni}^t = \int_0^{t_{\max}} dt\, \rho(t) f_i(t) \int_0^{2\pi} d\phi \left(\hat{t} \times \hat{n}\right) \cdot \bar{H}^{inc}(t,\phi) e^{-jn\phi} \qquad \text{(2.4-16)} \quad \text{[MAUT 77, Eq.(18)]}$$

and

$$\mathbb{I}_{ni}^\phi = \int_0^{t_{\max}} dt\, \rho(t) f_i(t) \int_0^{2\pi} d\phi \left(\hat{\phi} \times \hat{n}\right) \cdot \bar{H}^{inc}(t,\phi) e^{-jn\phi} \qquad \text{(2.4-17)} \quad \text{[MAUT 77, Eq.(19)]}$$

These are the coefficients of the excitation associated with the $\hat{t}$-directed and $\hat{\phi}$-directed n-th BOR harmonic; thus even the incident field $\bar{H}^{inc}$ is effectively expanded in terms of such harmonics. With N_t expansion functions along the generatrix, $\left[\mathbb{I}_n^t\right]$ and $\left[\mathbb{I}_n^\phi\right]$ are each column vectors of size $N_t \times 1$.

[29] The notation we use here for the excitation vectors is slightly different from that in [MAUT 77].

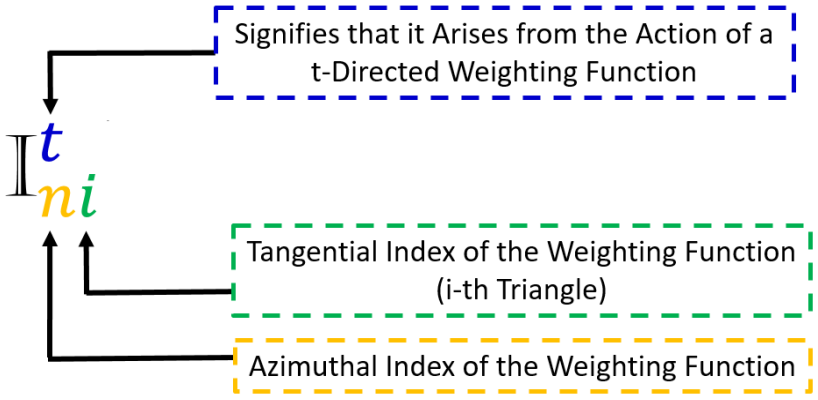

Fig.2.4-3 : Excitation vector term for MFIE formulation.

The $f_i(t)$ in (2.4-16) and (2.4-17) is from the *i*-th weighting function. Using the multiple-delta-function approximation for the weighting function (as mentioned above), the t-integration in (2.4-16) and (2.4-17) reduces these expressions to[30]

$$\mathbb{I}^t_{ni} = \sum_{q=1}^{4} T_q w_q \int_0^{2\pi} d\phi \left(\hat{t}\times\hat{n}\right)\cdot \bar{H}^{inc} e^{-jn\phi} \tag{2.4-18}$$

and

$$\mathbb{I}^{\phi}_{ni} = \sum_{q=1}^{4} T_q w_q \int_0^{2\pi} d\phi \left(\hat{\phi}\times\hat{n}\right)\cdot \bar{H}^{inc} e^{-jn\phi} \tag{2.4-19}$$

with T_q and w_q being weights, as explained in Appendix F. The elements of the moment method admittance matrix are

$$\left(Y_n^{tt}\right)_{ij} = \pi \int_0^{t_{\max}} dt\ \rho f_i(t) f_j(t)$$
$$+ k^3 \int_0^{t_{\max}} dt\, \rho f_i(t) \int_0^{t_{\max}} dt'\ \rho' f_i(t') \left[\left((\rho'-\rho)\cos(v') - (z'-z)\sin(v')\right)G_2 - G_1\rho\cos(v')\right]$$

(2.4-20) [MAUT 77, Eq.(20)]

[30] Although the t-integration limits are shown from 0 to $t_{\max}$, they of course reduce to integration over the supports of the expansion and weighting functions involved.

$$\left(Y_n^{\phi t}\right)_{ij} = jk^3 \int_0^{t_{\max}} dt\ \rho f_i(t) \int_0^{t_{\max}} dt'\ \rho' f_j(t') \left(\rho' \sin(v)\cos(v') - \rho \sin(v')\cos(v) - (z'-z)\sin(v)\sin(v')\right) G_3$$

(2.4-21) [MAUT 77, Eq.(21)]

$$\left(Y_n^{t\phi}\right)_{ij} = jk^3 \int_0^{t_{\max}} dt\ \rho f_i(t) \int_0^{t_{\max}} dt'\ \rho' f_j(t') (z'-z) G_3 \qquad \text{(2.4-22)} \quad \text{[MAUT 77, Eq.(22)]}$$

and

$$\left(Y_n^{\phi\phi}\right)_{ij} = \pi \int_0^{t_{\max}} dt\, \rho f_i(t) f_j(t) + k^3 \int_0^{t_{\max}} dt\, \rho f_i(t) \int_0^{t_{\max}} dt'\ \rho' f_j(t') \left[\left((\rho' - \rho)\cos(v') - (z'-z)\sin(v) \right) G_2 - G_1 \rho' \cos(v) \right]$$

(2.4-23) [MAUT 77, Eq.(23)]

where the "BOR Green's functions" are

$$G_1(\rho', z') = 2\int_0^{\pi} d\phi'\, G(\rho', \phi', z') \sin\left(\frac{\phi'}{2}\right) \cos(n\phi') \qquad \text{(2.4-24)} \quad \text{[MAUT 77, Eq.(24)]}$$

$$G_2(\rho', z') = \int_0^{\pi} d\phi'\, G(\rho', \phi', z') \cos(\phi') \cos(n\phi') \qquad \text{(2.4-25)} \quad \text{[MAUT 77, Eq.(25)]}$$

and

$$G_3(\rho', z') = \int_0^{\pi} d\phi'\, G(\rho', \phi', z') \sin(\phi') \sin(n\phi') \qquad \text{(2.4-26)} \quad \text{[MAUT 77, Eq.(26)]}$$

Quantity

$$G(\rho', \phi', z') = \frac{1 + jkR}{k^3 R^3} e^{-jkR} \qquad \text{(2.4-27)} \quad \text{[MAUT 77, Eq.(10)]}$$

with

$$R = \sqrt{(\rho - \rho')^2 + (z - z')^2 + 4\rho\rho' \sin^2\left(\frac{\phi'}{2}\right)} \qquad \text{(2.4-28)} \quad \text{[MAUT 77, Eq.(11)]}$$

Integration of course performed along the straight-line (frustum) representation of the BOR generatrix. Approximation, for the purposes of t-integration, of the expansion functions by

"pulses", and weighting functions by multiple-delta-functions, as already mentioned earlier, considerably simplify expression (2.4-20) through (2.4-23 to [MAUT 77, Eq.(31)]. The integrals needed to find G_1, G_2 and G_3 in (2.4-24) though (2.4-26) are evaluated using widely available Gaussian quadrature algorithms.

2.4.8 Discretized EFIE

Application of the method of moments to the EFIE as customized to a PEC object that is a BOR results in the set of matrix equations (one for each *n*-th BOR harmonic)

$$\begin{bmatrix} [Z_n^{tt}] & [Z_n^{t\phi}] \\ [Z_n^{\phi t}] & [Z_n^{\phi\phi}] \end{bmatrix} \begin{bmatrix} [I_n^t] \\ [I_n^\phi] \end{bmatrix} = \begin{bmatrix} \left[\mathbb{V}_n^t\right] \\ \left[\mathbb{V}_n^\phi\right] \end{bmatrix}; \quad n = 0, \pm 1, \pm 2, \ldots \qquad (2.4\text{-}29) \text{ [MAUT 77, Eq.(57)]}$$

Computational economy follows from the fact that

$$Z_{-n}^{tt} = Z_n^{tt} \qquad (2.4\text{-}30a) \text{ [MAUT 77, Eq.(103)]}$$

$$Z_{-n}^{t\phi} = -Z_n^{\phi t} \qquad (2.4\text{-}30b) \text{ [MAUT 77, Eq.(103)]}$$

$$Z_{-n}^{\phi t} = -Z_n^{\phi t} \qquad (2.4\text{-}30c) \text{ [MAUT 77, Eq.(103)]}$$

$$Z_{-n}^{\phi\phi} = Z_n^{\phi\phi} \qquad (2.4\text{-}30d) \text{ [MAUT 77, Eq.(103)]}$$

Once these sub-matrices have been evaluated for $n = 0,1,2,\ldots\ldots,N_h$ they are at once known for $n = -1,-2,\ldots\ldots,-N_h$. Because there are N_t expansion functions along the generatrix, each $[Y_n^{pq}]$ is a square sub-matrix of size $N_t \times N_t$.

Symbol $[I_n^t]$ represents a column vector of coefficients I_{nj}^t ($j = 0,1,2,\ldots\ldots,N_t$) of the expansion functions of the $\hat{t}$-directed current density, whereas $[I_n^\phi]$ is the same for coefficients I_{nj}^ϕ of the $\hat{\phi}$-directed current density, of the n-th BOR harmonic.

The terms in the column vectors of excitation coefficients on the right hand side of (2.4-29) are

$$\mathbb{V}_{ni}^{t} = \left\langle \bar{W}_{ni}^{t}, \bar{E}^{inc} \right\rangle = \int_{0}^{t_{\max}} dt\ \rho f_i(t) \int_{0}^{2\pi} d\phi\ \ \hat{t} \cdot \bar{E}^{inc}(t,\phi) e^{-jn\phi} \qquad (2.4\text{-}31)$$ [MAUT 77, Eq.(50)]

and

$$\mathbb{V}_{ni}^{\phi} = \left\langle \bar{W}_{ni}^{\phi}, \bar{E}^{inc} \right\rangle = \int_{0}^{t_{\max}} dt\ \rho f_i(t) \int_{0}^{2\pi} d\phi\ \ \hat{\phi} \cdot \bar{E}^{inc}(t,\phi) e^{-jn\phi} \qquad (2.4\text{-}32)$$ [MAUT 77, Eq.(50)]

Recall that in $\mathbb{V}_{ni}^{t} = \left\langle \bar{W}_{ni}^{t}, \bar{E}^{inc} \right\rangle$ the index n refers to the azimuthal mode index (the n-th BOR harmonic) in the weighting function $\bar{W}_{ni}^{t}$, and the tangential index i to the fact that this weighting function contains the $i-th$ triangle along the generatrix. This is emphasised in Fig.2.4-4.

These are the coefficients of the excitation associated with the $\hat{t}$-directed and $\hat{\phi}$-directed n-th BOR harmonic; thus even the incident field is expanded in terms of such harmonics. With N_t expansion functions along the generatrix, $\mathbb{V}_{n}^{t}$ and $\mathbb{V}_{n}^{\phi}$ are each column vectors of size $N_t \times 1$.

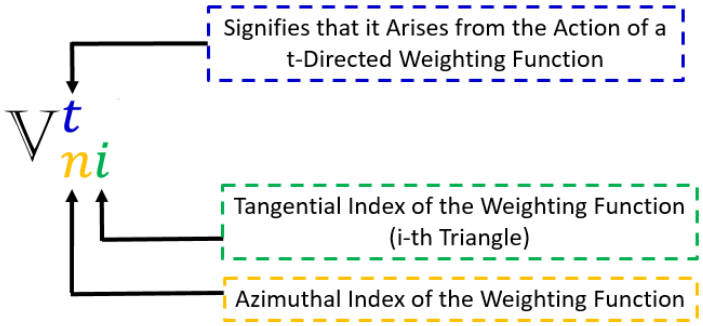

Fig.2.4-4 : Excitation vector term for EFIE formulation.

The $f_i(t)$ in (2.4-31) and (2.4-32) is from the *i*-th weighting function. Using the multiple-delta-function approximation for the weighting function the t-integration in (2.4-31) and (2.4-32) reduces these expressions to [MAUT 77]

$$\bar{\mathbb{V}}_{ni}^{t} = \sum_{q=1}^{4} T_q w_q \int_{0}^{2\pi} d\phi\ \ \hat{t} \cdot \bar{E}^{inc} e^{-jn\phi} \qquad (2.4\text{-}33)$$ [MAUT 77, Eq.(50)]

and

$$\bar{\mathbb{V}}_{ni}^{\phi} = \sum_{q=1}^{4} T_q w_q \int_0^{2\pi} d\phi \quad \hat{\phi} \cdot \bar{E}^{inc} e^{-jn\phi} \tag{2.4-34}$$ [MAUT 77, Eq.(50)]

The elements of the moment method impedance matrix are

$$\left(Z_n^{tt}\right)_{ij} = j \int_0^{t_{\max}} dt \int_0^{t_{\max}} dt' \left\{ k^2 \rho f_i(t) \rho' f_j(t') \left(G_5 \sin(v)\sin(v') + G_4 \cos(v)\cos(v') \right) \right\}$$
$$- j \int_0^{t_{\max}} dt \int_0^{t_{\max}} dt' \left\{ \frac{\partial}{\partial t}\left(\rho f_i(t)\right) \frac{\partial}{\partial t'}\left(\rho' f_j(t')\right) G_4 \right\}$$

(2.4-35) [MAUT 77, Eq.(58)]

$$\left(Z_n^{\phi t}\right)_{ij} = -\int_0^{t_{\max}} dt\, \rho f_i(t) \int_0^{t_{\max}} dt' \left(k^2 \rho' f_j(t') G_6 \sin(v') + \frac{n}{\rho} \frac{\partial}{\partial t'}\left(\rho' f_j(t')\right) G_4 \right)$$

(2.4-36) [MAUT 77, Eq.(59)]

$$\left(Z_n^{t\phi}\right)_{ij} = \int_0^{t_{\max}} dt \int_0^{t_{\max}} dt'\, \rho' f_j(t') \left(k^2 \rho f_i(t) G_6 \sin(v) + \frac{n}{\rho'} \frac{\partial}{\partial t}\left(\rho f_i(t)\right) G_4 \right)$$

(2.4-37) [MAUT 77, Eq.(60)]

and

$$\left(Z_n^{\phi\phi}\right)_{ij} = j \int_0^{t_{\max}} dt\, \rho f_i(t) \int_0^{t_{\max}} dt'\, \rho' f_j(t') \left(k^2 G_5 - \frac{n^2}{\rho\rho'} G_4 \right) \tag{2.4-38}$$ [MAUT 77, Eq.(61)]

with the additional "BOR Green's functions"

$$G_4 = \int_0^{\pi} d\phi' \frac{e^{-jkR}}{kR} \cos\left(n\phi'\right) \tag{2.4-39}$$ [MAUT 77, Eq.(62)]

$$G_5 = \int_0^{\pi} d\phi' \frac{e^{-jkR}}{kR} \cos\left(\phi'\right) \cos\left(n\phi'\right) \tag{2.4-40}$$ [MAUT 77, Eq.(63)]

and

$$G_6 = \int_0^{\pi} d\phi' \frac{e^{-jkR}}{kR} \sin\left(\phi'\right) \sin\left(n\phi'\right) \tag{2.4-41}$$ [MAUT 77, Eq.(64)]

Integration is performed along the straight-line representation of the BOR generatrix. Approximation, for the purposes of t-integration, of the expansion functions by "pulses", and weighting functions by multiple-delta-functions, once more considerably simplify expressions (2.4-35) through (2.4-38) to [MAUT 77, Eq.(69)] through [MAUT 77, Eq.(72)]. The integrals needed to find G_4, G_5 and G_6 in (2.4-39) though (2.4-41) are evaluated using Gaussian quadrature algorithms.

2.4.9 Discretized CFIE

As follows from Section 2.3.5, the discretized form of the CFIE, for each *n*-th BOR harmonic, is

$$\left[\begin{bmatrix} Y_n^{tt} & Y_n^{t\phi} \\ Y_n^{\phi t} & Y_n^{\phi\phi} \end{bmatrix} + \alpha \begin{bmatrix} Z_n^{tt} & Z_n^{t\phi} \\ Z_n^{\phi t} & Z_n^{\phi\phi} \end{bmatrix}\right]\begin{bmatrix} [I_n^t] \\ [I_n^\phi] \end{bmatrix} = \begin{bmatrix} [\mathbb{I}_n^t] \\ [\mathbb{I}_n^\phi] \end{bmatrix} + \alpha \begin{bmatrix} [\mathbb{V}_n^t] \\ [\mathbb{V}_n^\phi] \end{bmatrix}; \quad n = 0, \pm 1, \pm 2, \ldots$$

(2.4-42) [MAUT 77, Eq.(88)]

All terms have already been defined in Section 2.4.6 and Section 2.4.7. We often refer to

$$[\mathbb{B}_n] = \begin{bmatrix} [\mathbb{B}_n^t] \\ [\mathbb{B}_n^\phi] \end{bmatrix} = \begin{bmatrix} [\mathbb{I}_n^t] \\ [\mathbb{I}_n^\phi] \end{bmatrix} + \alpha \begin{bmatrix} [\mathbb{V}_n^t] \\ [\mathbb{V}_n^\phi] \end{bmatrix} \qquad (2.4\text{-}43)$$

2.4.10 Measurement Matrices and Far-Zone Fields from the Known Electric Current Density

Once the matrix equation of any of the IE's has been solved for each BOR harmonic, the electric surface current density on the BOR surface has been determined, and hence the far-zone fields[31] in direction (θ_r, ϕ_r) caused by it[32] can be found from

[31] The directions in which a far-zone pattern is being observed will be denoted either by (θ_r, ϕ_r) as done here, or simply as (θ, ϕ).

[32] It is only the scattered field. The total field will be the sum of this scattered field and the incident field (due to the impressed sources) that was used to determine the excitation column matrix terms. In other words, we must remember that $E_\theta(r, \theta_r, \phi_r) = E_\theta^{scat}(r, \theta_r, \phi_r) + E_\theta^{inc}(r, \theta_r, \phi_r)$ and $E_\phi(r, \theta_r, \phi_r) = E_\phi^{scat}(r, \theta_r, \phi_r) + E_\phi^{inc}(r, \theta_r, \phi_r)$.

$$\begin{bmatrix} E_\theta^{scat}(r,\theta_r,\phi_r) \\ E_\phi^{scat}(r,\theta_r,\phi_r) \end{bmatrix} = \frac{-j\eta e^{-jkr}}{4\pi r} \sum_{n=-N}^{N} \left[\begin{array}{c|c} \left[R_n^{t\theta}(\theta_r)\right] & \left[R_n^{\varphi\theta}(\theta_r)\right] \\ \hline \left[R_n^{t\phi}(\theta_r)\right] & \left[R_n^{\varphi\phi}(\theta_r)\right] \end{array} \right] \left[\begin{array}{c} \left[I_n^t\right] \\ \hline \left[I_n^\varphi\right] \end{array} \right] e^{jn\phi_r}$$

(2.4-44) [MAUT 77, Eq.(91)]

The above so-called far-zone "measurement matrices" $\left[R_n^{pq}(\theta_r,\phi_r)\right]$ are transposes of column vectors whose elements, illustrated in Fig.2.4-5, and are given by :

$$R_{ni}^{t\theta}(\theta_r) = \pi j^n \sum_{p=1}^{4} T_{p+4i-4} \left\{ -2J_n \sin\theta_r \cos\nu + j(J_{n+1} - J_{n-1}) \cos\theta_r \sin\nu \right\} e^{jkz\cos\theta_r}$$

$$R_{ni}^{\phi\theta}(\theta_r) = -\pi j^n \sum_{p=1}^{4} T_{p+4i-4} (J_{n+1} + J_{n-1}) \cos\theta_r \, e^{jkz\cos\theta_r}$$

(2.4-45) [MAUT 77, Eq.(92)]

$$R_{ni}^{t\phi}(\theta_r) = \pi j^n \sum_{p=1}^{4} T_{p+4i-4} (J_{n+1} + J_{n-1}) \sin\nu \, e^{jkz\cos\theta_r}$$

and

$$R_{ni}^{\phi\phi}(\theta_r) = \pi j^{n+1} \sum_{p=1}^{4} T_{p+4i-4} (J_{n+1} - J_{n-1}) e^{jkz\cos\theta_r}$$

where

$$J_n = J_n(k\rho\sin\theta_r) \qquad (2.4\text{-}46) \quad [\text{MAUT 77, Eq.(96)}]$$

is the Bessel function of the first kind, and ρ, z and ν evaluated at $t = t_{p+2i-2}$. The terms T_{p+4i-4} are explained in Appendix F.

Because there are N_t expansion functions along the generatrix, each $[R_n^{pq}]$ is a row vector of size $1\times N_t$. Computational economy follows from the fact that

$$R_{-n}^{t\theta}(\theta_r) = R_n^{t\theta}(\theta_r) \qquad \text{(2.4-47a) [MAUT 77, Eq.(104)]}$$

$$R_{-n}^{t\phi}(\theta_r) = -R_n^{t\phi}(\theta_r) \qquad \text{(2.4-47b) [MAUT 77, Eq.(104)]}$$

$$R_{-n}^{\phi\theta}(\theta_r) = -R_n^{\phi\theta}(\theta_r) \qquad \text{(2.4-47c) [MAUT 77, Eq.(104)]}$$

$$R_{-n}^{\phi\phi}(\theta_r) = R_n^{\phi\phi}(\theta_r) \qquad \text{(2.4-47d) [MAUT 77, Eq.(104)]}$$

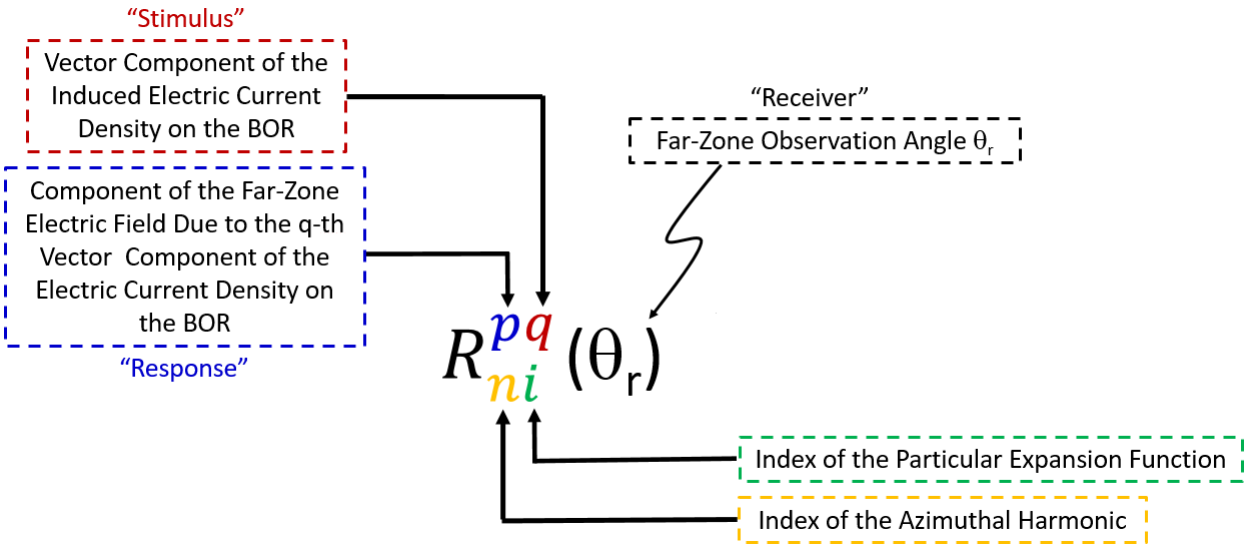

Fig.2.4-5 : Measurement matrix terms

2.5 CONCLUDING REMARKS

It was mentioned in Section 1.2 why non-spherical measurement surfaces S_{meas} would be desirable in some instances, but that NF-to-FF transformations are not available. This thesis proposes such a transformation. The goal of this chapter has been to review, and present in a consistent notation, some necessary theoretical background that will be exploited in achieving this aim.

Section 2.2 interpreted NF antenna measurement techniques as an application of the surface equivalence principle. It will facilitate the discussion in Chapter 3. Although these facts are known material for specialists in the theory of antenna measurements, we have found that it is not necessarily well-known by practitioners generally. Even if this perception is not completely true, we at any rate need to set the notation for Chapter 3.

The proposed NF-to-FF transformation involves the use of the moment method (MM) to compute the scattering from a perfectly conducting (PEC) modelled using an IE. The latter was thus briefly reviewed in Section 2.3. In particular, the proposed NF-to-FF transformation is based on scattering from a PEC object that is rotationally symmetric. Thus Section 2.4 collates an MM formulation customized for the numerical solution of the IEs pertaining to such an object, giving sufficient detail to connect seamlessly with its implementation in Chapter 4.

CHAPTER 3

Proposed Near-Field Measurement Technique for Arbitrarily-Shaped Rotationally-Symmetric Measurement Surfaces

3.1 INTRODUCTION

A NF-to-FF transformation that is applicable to a measurement surface of any shape is proposed in outline in Section 3.2, and then reasons are given for restricting it to a rotationally symmetric shape[33]. This transformation, as one of its steps, converts the measured tangential electric field $\hat{n}(S_{meas})\times\bar{E}^{NF}(S_{meas})$ into an equivalent magnetic current density. This is described in Section 3.3. The generation of the fields needed to serve as the excitation in the IE whose solution actually performs the NF-to-FF transformation, namely the "incident fields", are those of this equivalent magnetic current density when it radiates in free space. Finally, Section 3.5 concludes the chapter, and leads to the description of the implementation of the proposed NF-to-FF transformation in Chapter 4, and its application in Chapter 5.

3.2 PROPOSED NEAR-FIELD TO FAR-FIELD MEASUREMENT TECHNIQUE FOR AN ARBITRARY MEASUREMENT SURFACE

In Section 2.2 we saw how the near-field antenna measurement problem can be reduced (at least in principle) to the following steps:

- Determine an equivalent impressed magnetic current density $\bar{M}_s^{NF} = -\hat{n}(S_{meas})\times\bar{E}^{NF}(S_{meas})$ from the tangential electric field $\hat{n}(S_{meas})\times\bar{E}^{NF}(S_{meas})$ actually acquired by a probe that moves over a fictitious measurement surface S_{meas} surrounding the antenna[34].

[33] Recall that no such restriction is given on the AUT itself, but rather only upon the measurement surface around the AUT.

[34] The minimum size of this surface is technically given by a BOR that fully encapsulates the MRS of the AUT, while in applied use, according to the rule of thumb quoted in [PARI 14], the minimum size of the BOR will be given by the sum of the MRSs of the AUT and that of the probe antenna, plus an additional tolerance of 1 to 3λ, so as not to induce any reactive coupling between the AUT and NF-probe.

- Determine the fields radiated by the antenna as the fields due to an impressed magnetic current density $\bar{M}_s^{NF}$ radiating in the presence of a PEC object whose surface is the same as S_{meas}, using[35]

$$\bar{E}^{inc}(\bar{r}) = \iint_{S_{meas}} \tilde{G}_{\text{em}}^{\text{PEC}}(\bar{r},\bar{r}') \cdot \bar{M}_s^{NF}(\bar{r}')\, dS' \tag{3.2-1}$$

The difficulty is that the required Green's function $\tilde{G}_{\text{em}}^{\text{PEC}}(\bar{r},\bar{r}')$ needed to make the 2nd step possible is not known when S_{meas} is other than a spherical shape[36]. We wish to use the near-field measurement technique when S_{meas} is not spherical. In this work we propose to use the following basic approach to do this : Use an IE from Section 2.3 to find the fields of $\bar{M}_s^{NF}$ radiating in the presence of a PEC object whose surface is the same as S_{meas}. These fields will be those of the original AUT. This constitutes the proposed NF-to-FF transformation.

It would naïve to imagine that a similar idea has not been thought of by others, even though it has not been explicitly stated as such. However, the immediate difficulty is that S_{meas} will in general be electrically large, and so the solution of the IE for $\bar{M}_s^{NF}$ radiating in the presence of a PEC object whose surface is the same as S_{meas} will be computationally very demanding. The resulting matrix equation will be very large. For example, if one models a spherical PEC surface of radius only $a = 3\lambda$ using a general purpose MM code then, in order to obtain reasonably accurate values of the far-zone field with just a simple incident field[37], close to 60000 unknowns are needed to represent the unknown electric current density on the PEC sphere. At the time of the writing of this thesis, a high-end personal computer of the type typically used with NF antenna measurement ranges, takes roughly 4 hours to solve such a problem, per frequency of interest. This would not be acceptable in antenna measurement practice.

In this work, the second aspect of the proposed NF-to-FF transformation is to restrict[38] surface S_{meas} to one that is rotationally symmetric (a "body-of-revolution" or BOR) but otherwise arbitrary. A spherical surface is then a special case. This will allow us to solve the IE using a

[35] The reason for using the superscript "inc" will be made clear later.
[36] We here mean surfaces of finite extent.
[37] This example will again be mentioned in Section 4.3.
[38] This is not really a 'restriction' in practice, as will be mentioned in Section 3.3.

method of moments approach that exploits the BOR shape to reduce the resulting large matrix equation into several smaller (and independent) ones whose solution is more rapid and can be done in parallel. Such a formulation was outlined in Section 2.4. The unknown in the IE will be the equivalent current density $\bar{J}_s$ on the PEC BOR surface, and it generates the scattered fields $\bar{E}^{scat}(S_{meas})$ and $\bar{H}^{scat}(S_{meas})$. The incident fields $\bar{E}^{inc}(S_{meas})$ and $\bar{H}^{inc}(S_{meas})$ that form the excitation of the IE are due to $\bar{M}_s^{NF}$ radiating in free space (with the PEC BOR absent). The total fields

$$\bar{E}^{total}(\bar{r}) = \bar{E}^{inc}(\bar{r}) + \bar{E}^{scat}(\bar{r}) \tag{3.2-2}$$

and

$$\bar{H}^{total}(\bar{r}) = \bar{H}^{inc}(\bar{r}) + \bar{H}^{scat}(\bar{r}) \tag{3.2-3}$$

at $\bar{r}$ exterior to S_{meas} are then the AUT fields being sought. It is most important to appreciate that $\hat{n}(S_{meas}) \times \bar{E}^{inc}(S_{meas})$ is *not* the same as the $\hat{n}(S_{meas}) \times \bar{E}^{NF}(S_{meas})$ acquired on the measurement surface. As per the surface equivalence theorem, $\bar{E}^{NF}(S_{meas})$ would be generated by the combination of $\bar{M}_s^{NF} = -\hat{n}(S_{meas}) \times \bar{E}^{NF}(S_{meas})$ and $\bar{J}_s^{NF} = \hat{n}(S_{meas}) \times \bar{H}^{NF}(S_{meas})$ on S_{meas}, and **the whole problem is that we do not know the latter electric current density from measured test data**. $\bar{J}_s^{NF}$ is not the same as the $\bar{J}_s$ on the PEC BOR that we will solve for to find $\bar{E}^{scat}(\bar{r})$.

3.3 ACQUISITION & INTERPOLATION

In the imagined NF measurement process the field $\hat{n}(\bar{r}_q) \times \bar{E}^{NF}(\bar{r}_q)$ is acquired at a set of points $\{\bar{r}_q, q = 1, 2, ..., Q\}$ on S_{meas}, with Q_t points along any "line-of-longitude" (i.e. generating curve) and Q_ϕ points along any "line-of-latitude" . The latter defines the angle $\Delta\phi_{acquire}$ between acquisition points on any line-of-latitude. Indeed, these points at once define the BOR measurement surface[39] S_{meas}, as depicted[40] in Fig.3.3-1. The red dots represent points at which

[39] The assumption - which is a realistic one - is that the NF data points will be acquired by a probe on a robotic arm that steps along the generatrix of the BOR surrounding the AUT, each time the AUT (mounted on a turntable)

the measurement probe would sample the components $E_t^{NF}(\bar{r}_q)$ and $E_\phi^{NF}(\bar{r}_q)$ of $\hat{n}(\bar{r}_q)\times\bar{E}^{NF}(\bar{r}_q)$ of the AUT. An interpolation scheme is used to simultaneously interpolate both the BOR geometry[41] (simultaneously defining S_{meas} completely) and the complex values of components $E_t^{NF}(\bar{r}_q)$ and $E_\phi^{NF}(\bar{r}_q)$ on the BOR[42]. In other words, after use of the interpolation algorithm, we can find $E_t^{NF}(\bar{r}_s)$ and $E_\phi^{NF}(\bar{r}_s)$ at any point $\bar{r}_s=(x_s,y_s,z_s)=(\rho_s,\phi_s,z_s)$ on the BOR surface S_{meas} and not only at those points $\bar{r}_q$ at which the probe acquired them. If the axis of the BOR surface S_{meas} is perfectly aligned with the z-axis then the above interpolation can be one-dimensional along the generatrix, the rotational symmetry completing the process.

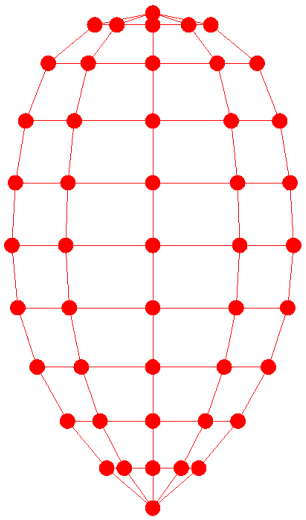

Fig.3.3-1 : Points $\{\bar{r}_q, p=1,2,....,Q\}$ on the BOR measurement surface[43] S_{meas} at which the fields $E_t^{NF}(\bar{r}_s)$ and $E_\phi^{NF}(\bar{r}_s)$ are acquired.

---

rotates a full 360°. This will accurately sample the tangential electric field over some intended BOR. Small probe position errors (by which is meant deviations form a perfect spherical S_{meas}) always occur in NF testing. Here it is the actual probe positions that actually define S_{meas}.

[40] The implication is not that the particular surface shape shown in Fig.3.3-1 is recommended; we simply wished to depict a surface other than a sphere to emphasize that, although it is a BOR, it need not be a sphere.

[41] If we refer to the measurement surface we will simply call it the BOR. When we are talking about a PEC object whose surface is identical to the measurement surface we will call it the PEC-BOR.

[42] That such interpolation is possible without loss of information is known from work such as [BUCCI 87], [BUCCI 87] and [BUCCI 89].

[43] We repeat that we are not implying that this particular BOR is a desirable one for NF measurements; this shape is being shown largely to re-emphasize that the BOR need not be a sphere.

In terms of a local coordinate system at $\bar{r}_s$ with unit vectors $(\hat{n},\hat{\phi},\hat{t})$, we can write[44] this in the alternative form[45]

$$\bar{E}^{NF}(\bar{r}_s) = E_t^{NF}(\bar{r}_s)\hat{t}(\bar{r}_s) + E_\phi^{NF}(\bar{r}_s)\hat{\phi}(\bar{r}_s) + E_n^{NF}(\bar{r}_s)\hat{n}(\bar{r}_s) \qquad (3.3\text{-}1)$$

In NF testing only $E_t^{NF}(\bar{r}_s)$ and $E_\phi^{NF}(\bar{r}_s)$ need be known (and hence acquired[46]). The component $E_n^{NF}(\bar{r}_s)$ normal to S_{meas} is not needed nor acquired. Note that if the BOR measurement surface is a sphere, then $\hat{t}(\bar{r}_s) = -\hat{\theta}(\bar{r}_s)$, and hence we would have $E_t^{NF}(\bar{r}_s) = -E_\theta^{NF}(\bar{r}_s)$.

Using the fact that $\hat{n}\times\hat{t} = -\hat{\phi}$, $\hat{n}\times\hat{\phi} = \hat{t}$ and $\hat{n}\times\hat{n} = 0$, use of (3.3-1) and (2.2.5) yields

$$\bar{M}_s^{NF}(\bar{r}_s) = -E_\phi^{NF}(\bar{r}_s)\,\hat{t}(\bar{r}_s) + E_t^{NF}(\bar{r}_s)\,\hat{\phi}(\bar{r}_s) = M_t^{NF}(\bar{r}_s)\,\hat{t}(\bar{r}_s) + M_\phi^{NF}(\bar{r}_s)\,\hat{\phi}(\bar{r}_s) \qquad (3.3\text{-}2)$$

3.4 INCIDENT FIELDS $\bar{E}^{inc}(S_{meas})$ AND $\bar{H}^{inc}(S_{meas})$ DUE TO $\bar{M}_s^{NF}(\bar{r}_s)$: OPTIONS

In Section 3.3 we explained why we can consider (due to interpolation) the measured quantity $\hat{n}(S_{meas})\times\bar{E}^{NF}(S_{meas})$ to be known as a continuous function over the measurement surface S_{meas}. This can be viewed as a known 'shroud' of magnetic current density $\bar{M}_s^{NF}(\bar{r}_s)$. We next consider how this $\bar{M}_s^{NF}(\bar{r}_s)$ may be used to find $(\bar{E}^{inc},\bar{H}^{inc})$ due to $\bar{M}_s^{NF}$ radiating in free space. Recall that this $(\bar{E}^{inc},\bar{H}^{inc})$ is needed at two different stages of the new NF-to-FF transformation :

---

[44] In (3.3-1) and (3.3-2) we purposefully show the explicit dependence of the unit vectors on the point $\bar{r}_s$ at times, since this needs to be kept firmly in mind when undertaking the transformations under discussion here. Continuing to do so will make the already cumbersome notation to follow even worse, and so we will not always do this.

[45] Once the BOR has been defined, these unit vectors are known at each point on its surface. Note in (3.3-1) that the subscript "n" is not an integer index but denotes "normal component".

[46] In accordance with the uniqueness theorem [HARR 61, pp.100-103].

(a). It is needed in order to determine the excitation vectors in the moment method solution of the IE. In such use they are of course required at points in the vicinity of the NF-BOR, namely $\bar{E}^{inc}(S_{meas})$ and $\bar{H}^{inc}(S_{meas})$.

(b). It is needed in the far-zone as well, as $\bar{E}^{inc}(S_{\infty})$ and $\bar{H}^{inc}(S_{\infty})$,where it has to be added to the scattered field due to the current density $\bar{J}_s$ on the PEC-BOR.

Actual determination of these quantities is not computationally insignificant, and is discussed in Section 4.4.

3.5 CONCLUSIONS

A NF-to-FF transformation that is applicable to a measurement surface of any rotationally symmetric shape has been proposed. Its implementation is discussed next, in Chapter 4, followed by its validated in Chapter 5. In the chapters that follow, we will denote the $\bar{J}_s$ on the PEC-BOR by the symbol $\bar{J}_{\text{pec}}$; this will allow us to cease having to state “on the PEC-BOR”.

CHAPTER 4

Implementation of the CEM-Based Near-Field to Far-Field Transformation

4.1 INTRODUCTION

The first goal of this chapter is related to the implementation in computer code, of the MM formulation for the solution of the EFIE, MFIE and CFIE models for scattering from a perfectly conducting (PEC) body-of-revolution (BOR). This is essential to performing the NF-to-FF transformation that has been proposed in Chapter 3. Such a MM code is not available commercially, and so had to be developed from scratch. Once one defines incident fields $(\bar{E}^{inc}, \bar{H}^{inc})$, the nodes (and hence shape) of the BOR, the number of expansion functions to be used along the generatrix, and the number of azimuthal harmonics to be used, and the frequency, the MM code[47] is able to compute the electric surface current density $\bar{J}_{pec}$ on the BOR, from which the scattered fields $(\bar{E}^{scat}, \bar{H}^{scat})$ are found, and hence the total fields $(\bar{E}, \bar{H}) = (\bar{E}^{inc}, \bar{H}^{inc}) + (\bar{E}^{scat}, \bar{H}^{scat})$. As stated in Chapter 2, the MM code whose development and performance is discussed here, follows the mathematical formulation given in [MAUT 77], and most of the numerical analysis (eg. numerical evaluation of certain integrals) suggested there. However, Section 4.2 briefly describes some numerical analysis procedures different from that recommended in [MAUT 77], and the relation between the near-field data acquisition locations and the BOR geometry. Section 4.3 then benchmarks the MM code by applying it to the case of a plane wave incident on a spherical BOR, a concentrated impressed source close to a spherical BOR, and a plane wave incident on a so-called cone-sphere BOR. The outcomes of *NFBOR* are compared to those obtained using other computational electromagnetic tool that do not incorporate a BOR assumption, thus validating it. This is all done quite separate from the use of *NFBOR* in the NF-to-FF transformation.

[47] Although the EFIE, MFIE and CFIE formulations are all included in the same code, it will be convenient to sometimes refer to "the EFIE code", "the MFIE code" and the "CFIE code" as if they were separate. They could have been written separately, but were not.

The code *NFBOR* will of course be part of the implementation of the proposed NF-to-FF transformation. Before it can be applied, it is necessary to find $\bar{E}^{inc}(S_{meas})$ and $\bar{H}^{inc}(S_{meas})$ due to $\bar{M}_s^{NF}(\bar{r}_s)$, as mentioned in Section 3.4. A means of achieving this in a computationally efficient way is proposed in Section 4.4, and is the second goal of this chapter. An examination of the performance of the latter approach is conducted in Section 4.5 and Section 4.6.

Section 4.7 concludes the chapter.

4.2 NUMERICAL EVALUATION OF TERMS IN THE MOMENT METHOD IMPLEMENTATION

4.2.1 Numerical Evaluations

The MM formulation for the solution of the EFIE, MFIE and CFIE models of PEC bodies-of-revolution, described in Section 2.4, has been implemented in code *NFBOR* in a MATLAB environment. Many of the numerical analysis algorithms have been implemented following advice given in [MAUT 77]. However, matrix solution algorithms intrinsic to MATLAB have been used instead of ones from [ABRA 64] suggested in [MAUT 77]. Integrations with respect to the azimuthal coordinate, in finding the excitation vector terms, have been performed using the fast Fourier transform (FFT), as described in detail in Appendix F. Other numerical integrations that [MAUT 77] indicates can be done using Gaussian quadrature rules are performed in this way using weights and abscissa values now widely available up to even high orders.

4.2.2 Relation of BOR Points to Near-Field Acquisition Points

In Fig.4.2-1(a) the large red dots are the field measurement points $\bar{r}_q$. In Fig.4.2-1(b) a parametric interpolant has been found that now defines a curved BOR on which these points $\bar{r}_q$ lie. Once this has been done we can compute the coordinates of any points $\bar{r}_s$ on the BOR. This at once provides us complete information on the generatrix of the BOR, from which we select the finite number of locations (ρ_i^-, z_i^-) on the generatrix as defined in Section 2.4.3. The number N_P of such nodes may be greater than the number of field measurement points $\bar{r}_q$ that lie on

each generatrix. Recall that the now-defined BOR, although faceted along any generatrix, is perfectly rotationally symmetric about the z-axis; it is a frustum. It is important to realise that the quadrilateral-like shapes (with white line sides) have merely been drawn in so that the three-dimensionality of the BOR can be pictured.

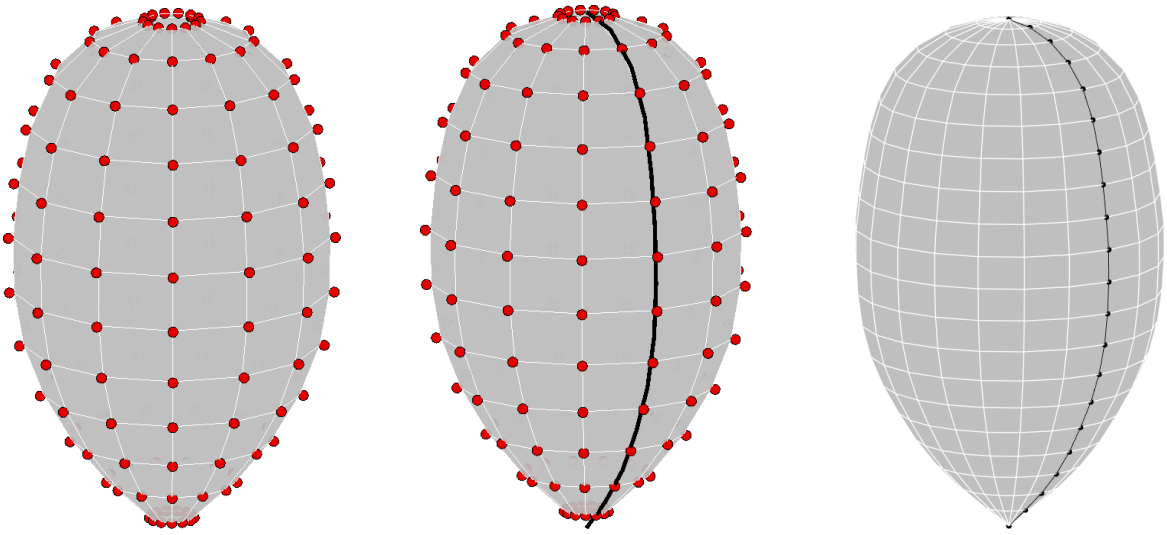

(a) **(b)** **(c)**

Fig.4.2-1 : Relation between the near-field acquisition points and the BOR geometry. In these particular diagrams quadrilateral-like shapes (with white line sides) have merely been drawn in so that the three-dimensionality of the BOR can be pictured.

4.3 BENCHMARK TESTING OF THE BOR CODE *NFBOR*

4.3.1 Introductory Comments

The code *NFBOR* developed in Section 4.2 must be tested. This is done separate from any use of the code as part of a NF-to-FF transformation. Computed fields and current densities for selected benchmark problems will be demonstrated for this purpose. The first is for plane wave incidence on PEC spheres of two different electrical sizes (radius 0.2λ and 1λ). By stating that *EFIE-NFBOR* was used in obtaining some result we mean that the EFIE capability in *NFBOR* was utilized, and similarly for the MFIE and CFIE capabilities. The second is for a PEC sphere (radius 3λ) excited by a concentrated source close to the PEC object; this is close to the way *NFBOR* will be used in the NF-to-FF transformation being proposed. The third is for plane wave

incidence on a non-spherical BOR. The computed results will show that NFBOR is indeed implementing the MM formulation correctly.

4.3.2 Plane Wave Incidence on a PEC Sphere

A. Incident Fields

The fields of a θ-polarised plane wave are given by

$$\bar{E}^{inc} = \hat{\theta} k \eta e^{-j\bar{k}\cdot\bar{r}} \tag{4.3-1}$$

$$\bar{H}^{inc} = \left(\bar{k} \times \hat{\theta}\right) e^{-j\bar{k}\cdot\bar{r}} \tag{4.3-2}$$

whereas those for a ϕ-polarised plane wave are

$$\bar{E}^{inc} = \hat{\phi} k \eta e^{-j\bar{k}\cdot\bar{r}} \tag{4.3-3}$$

and

$$\bar{H}^{inc} = \left(\bar{k} \times \hat{\phi}\right) e^{-j\bar{k}\cdot\bar{r}} \tag{4.3-4}$$

If the plane wave is incident from direction $(\theta^{inc}, \phi^{inc})$, its wave vector is

$$\bar{k} = -k\,(\hat{x}\sin\theta^{inc}\cos\phi^{inc} + \hat{y}\sin\theta^{inc}\sin\phi^{inc} + \hat{z}\cos\theta^{inc}) \tag{4.3-5}$$

with $k = \omega\sqrt{\mu_0\varepsilon_0}$, and position vector

$$\bar{r} = x\,\hat{x} + y\,\hat{y} + z\,\hat{z} \tag{4.3-6}$$

These fields are used in (2.4-18) and (2.4-19), (2.4-33) and (2.4-34), or (2.3-43), to determine the excitation vectors for the MFIE, EFIE and CFIE formulations for the case of plane wave incidence.

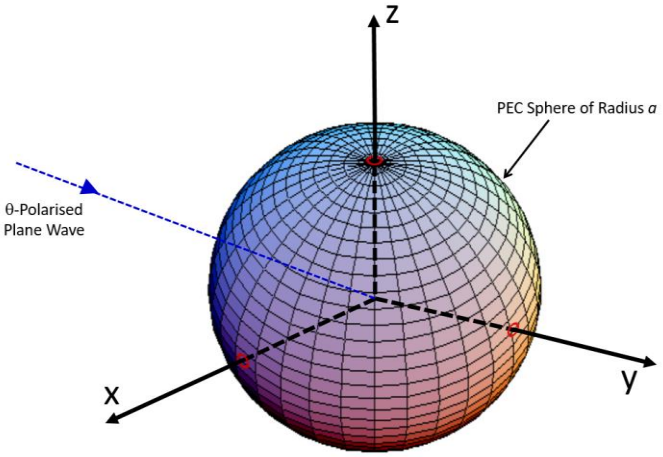

Fig.4.3-1 : PEC Sphere with θ- Polarised Plane Wave Incident from Direction $(\theta^{inc},\phi^{inc})$

B. PEC Sphere of Radius a = 0.2λ

We consider a θ-polarised plane wave incident on the PEC sphere (radius 0.2λ) from a direction $(\theta^{inc},\phi^{inc})=(30^{\circ},0^{\circ})$, as depicted in Fig.4.3-1. Note that the xy-plane pattern cut is obtained by fixing $\theta=90^{\circ}$ and varying ϕ, whereas the xz-plane pattern cut is obtained by fixing $\phi=0^{\circ}$ and varying θ.

The *NFBOR* results will be compared to those obtained using a commercial code [*FEKO*]. The latter code is a general purpose one, and any PEC object has to be finely meshed with triangular facets in order to obtain accurate computations that faithfully reflect the rotational symmetry of the object, resulting in tens of thousands of unknowns[48]. It is simply being used here as the reference against which to benchmark the *NFBOR* outcomes.

In order to obtain a quantitative measure of the correctness, a relative error is defined as

$$RE(\theta,\phi)=\frac{\left|\bar{E}_{NFBOR}(\theta,\phi)\right|-\left|\bar{E}_{FEKO}(\theta,\phi)\right|}{E_{NORM}} \tag{4.3-7}$$

with

$$E_{NORM}=\max_{(\theta,\phi)}\left\{\left|\bar{E}_{NFBOR}(\theta,\phi)\right|,\left|\bar{E}_{FEKO}(\theta,\phi)\right|\right\} \tag{4.3-8}$$

and

$$RE^{dB}(\theta,\phi)=20\log_{10}\left|RE(\theta,\phi)\right| \tag{4.3-9}$$

Fig.4.3-2(a) compares the *EFIE-NFBOR* relative power pattern for the scattered field to the *FEKO* generated result, in the xy-plane. Fig.4.3-2(b) demonstrates that the difference between the two results is indeed small. We should add that we refer to *FEKO* as the reference result and not the exact result. The reason is that we believe that the *NFBOR* result may be the "more correct" one in some cases because the BOR nature of the PEC object is inherent to the formulation, and by using larger values for N_t and N_h one effectively has the same resolution as an extremely fine mesh in code *FEKO*. Fig.4.3-3(a) shows a polar plot of the same scattered field patterns in the xy-plane, for all three integral equation models available via *NFBOR*. Once again Fig.4.3-3(b) reveals that differences between these formulations and *FEKO* are very small. Similar conclusions can be drawn from the scattered field patterns in the xz-plane in Fig.4.3-4.

[48] This was in fact used as an example in Section 3.2 to argue for use of a MM formulation that inherently assumes rotational symmetry of the object (the BOR), in so doing requiring significantly fewer unknowns.

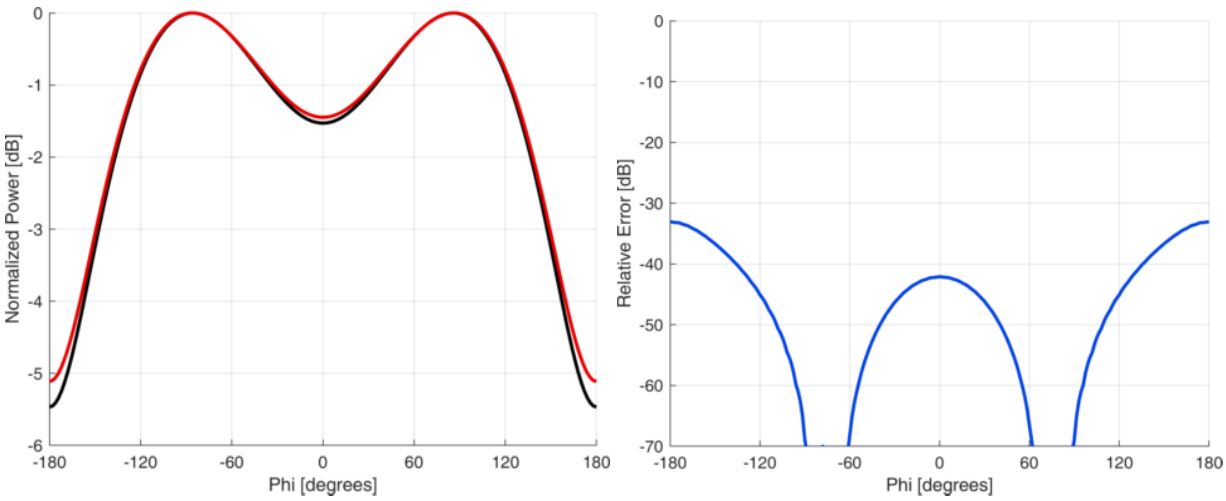

(a) **(b)**

Fig.4.3-2 : (a) Computed *EFIE- NFBOR* (red) and reference *FEKO* (black) scattered far-field relative power pattern in the xy-plane for a θ-polarised plane wave incident on the PEC sphere (radius 0.2λ) at angle (θ,ϕ) = (30°, 0°). (b) Corresponding relative error (blue) between the *NFBOR* and *FEKO* magnitudes, in the same plane.

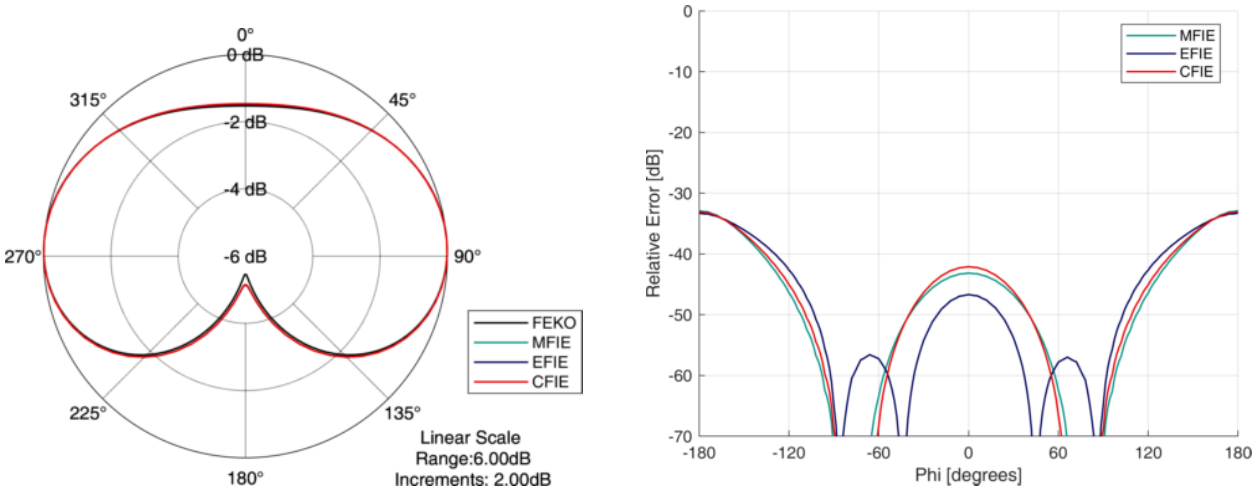

(a) **(b)**

Fig.4.3-3 : (a) Computed *NFBOR* (for three different IE types), and reference *FEKO*, scattered far-field relative power pattern in the xy-plane for a θ-polarised plane wave incident on the PEC sphere (radius 0.2λ) at angle (θ^{inc},ϕ^{inc}) = (30°, 0°). (b) Corresponding relative error between the three *NFBOR* and *FEKO* magnitudes, in the same plane.

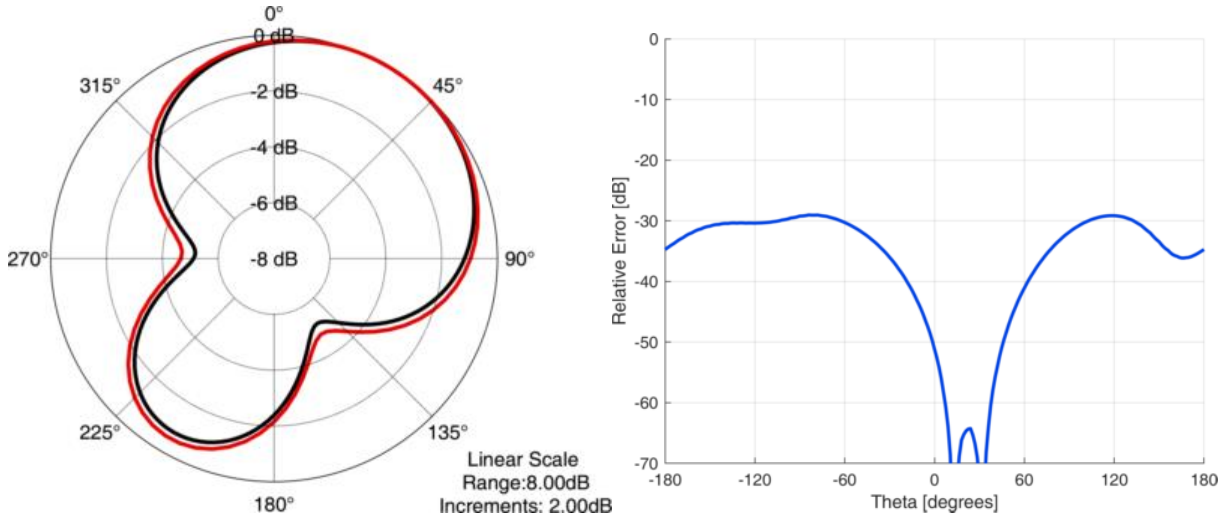

(a) **(b)**

Fig.4.3-4 : (a) Computed *EFIE- NFBOR* (red) and reference *FEKO* (black) scattered far-field relative power pattern in the xz-plane for a θ-polarised plane wave incident on the PEC sphere (radius 0.2λ) at angle (θ^{inc},ϕ^{inc}) = (30°, 0°). (b) Corresponding relative error (blue) between the *NFBOR* and *FEKO* magnitudes, in the same plane.

C. PEC Sphere of Radius a = λ

The incident field conditions, and computed outcomes observes, in this part are much the same as in Part B, except that the PEC spherical BOR is electrically larger, with a radius of 1λ. In fact, observations of Fig.4.3-5 through Fig.4.3-7 move us to draw the same conclusions as to the correctness of the *NFBOR* computations.

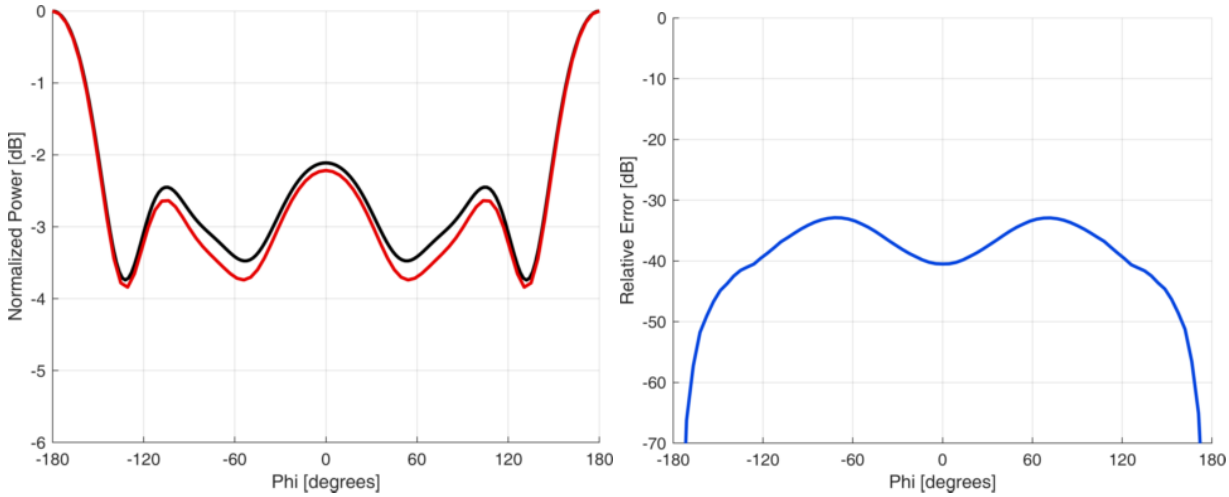

(a) **(b)**

Fig.4.3-5 : (a) Computed *EFIE- NFBOR* (red) and reference *FEKO* (black) scattered far-field relative power pattern in the xy-plane for a θ-polarised plane wave incident on the PEC sphere (radius λ) at angle (θ^{inc},ϕ^{inc}) = (30°, 0°). (b) Corresponding relative error (blue) between the *NFBOR* and *FEKO* magnitudes, in the same plane.

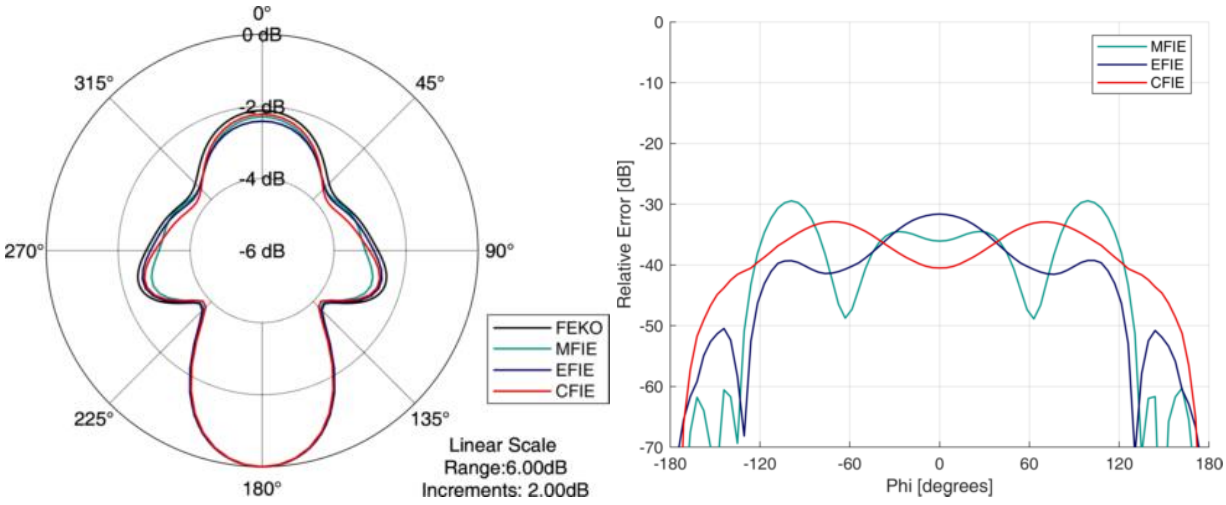

(a) **(b)**

Fig.4.3-6 : (a) Computed *NFBOR* (for three different IE types), and reference *FEKO*, scattered far-field relative power pattern in the xy-plane for a θ-polarised plane wave incident on the PEC sphere (radius λ) at angle (θ^{inc},ϕ^{inc}) = (30°, 0°). (b) Corresponding relative error between the three *NFBOR* and *FEKO* magnitudes, in the same plane.

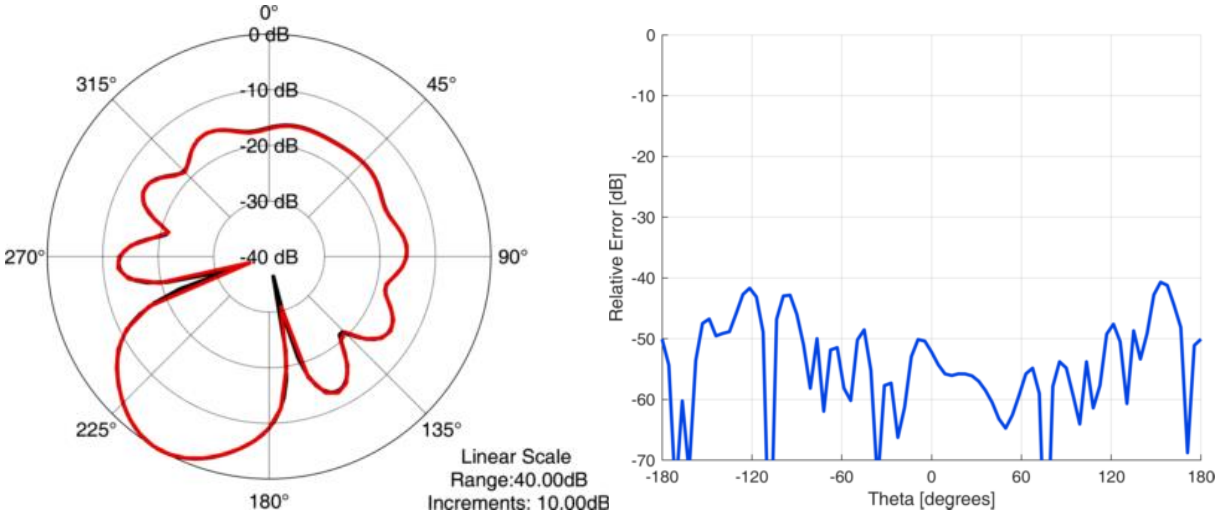

(a) **(b)**

Fig.4.3-7 : (a) Computed *EFIE- NFBOR* (red) and reference *FEKO* (black) scattered far-field relative power pattern in the xz-plane for a θ-polarised plane wave incident on the PEC sphere (radius λ) at angle (θ^{inc},ϕ^{inc}) = (30°, 0°). (b) Corresponding relative error (blue) between the *NFBOR* and *FEKO* magnitudes, in the same plane.

4.3.3 Infinitesimal Magnetic Dipole Next to a PEC Sphere of Radius a = 3λ

A. Incident Fields

We emphasize that the infinitesimal magnetic dipole being used in this test is simply a convenient impressed source other than a plane wave[49]. The *NFBOR* computations are again compared to those obtained using *FEKO* simulations of the same situation. The PEC spherical BOR is electrically larger than those used in Section 4.3.2.

[49] It is unrelated to the infinitesimal dipoles that will be used (in Section 4.4.5) in the determination of the incident fields $\bar{E}^{inc}(S_{meas})$ and $\bar{H}^{inc}(S_{meas})$ in the NF-to-FF transformation procedure.

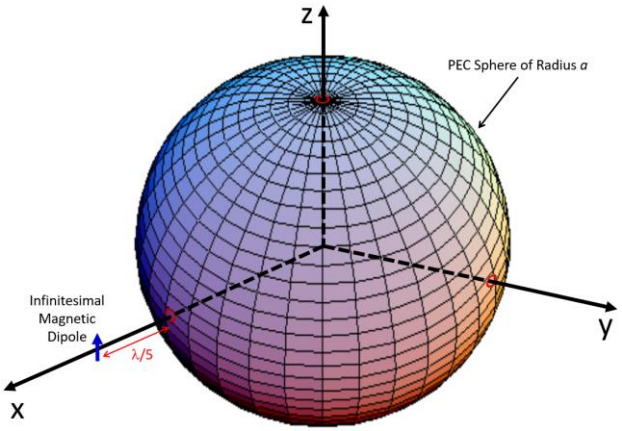

Fig.4.3-8 : Infinitesimal magnetic dipole adjacent to a PEC sphere of radius *a*. The grid shown is for diagrammatic purposes only and is unrelated to the mesh used in the moment method analysis of this configuration.

B. Computed Scattered Fields

Fig.4.3-9 and Fig.4.3-10 compare the scattered fields in the xy- and xz-planes, respectively. Note that the result in Fig.4.3-10 is normalized to the maximum value that in this case happens to occur in the xy-plane; thus all values are below 0dB in Fig.4.3-10. The relative error is once more around -30dB or less.

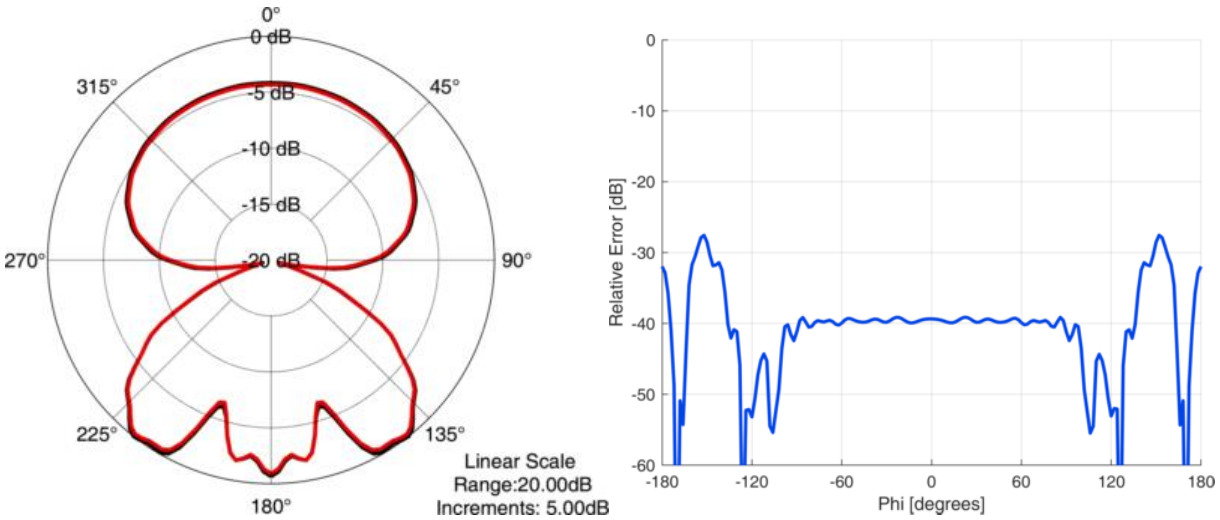

(a) **(b)**

Fig.4.3-9 : (a) Computed *EFIE- NFBOR* (red) and reference *FEKO* (black) scattered far-field relative power pattern in the xy-plane for the infinitesimal magnetic dipole impressed source specified in Part A. (b) Corresponding relative error (blue) between the *NFBOR* and *FEKO* magnitudes, in the same plane.

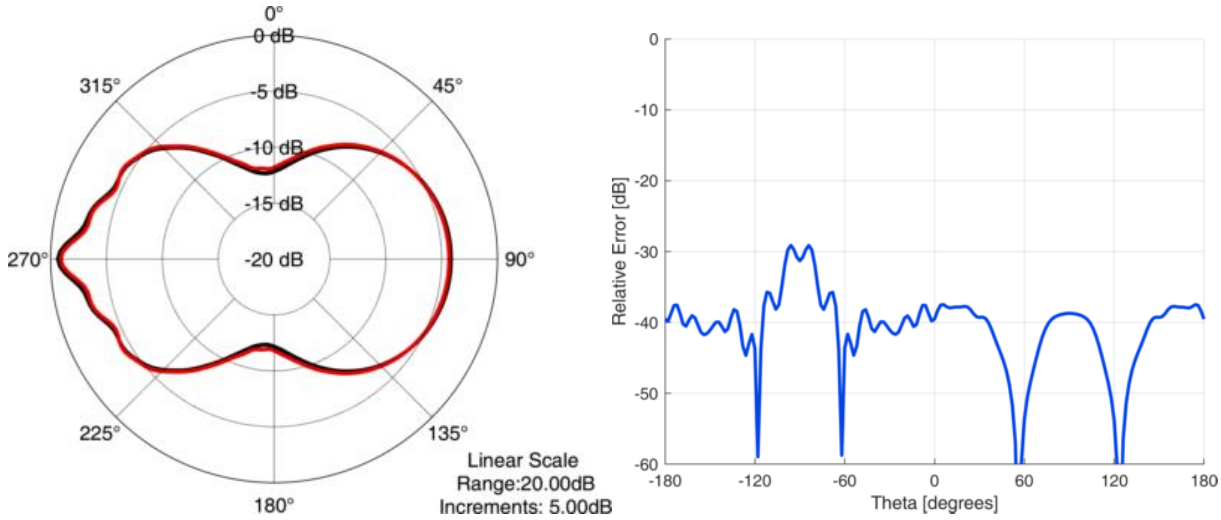

(a) **(b)**

Fig.4.3-10 : (a) Computed *EFIE- NFBOR* (red) and reference *FEKO* (black) scattered far-field relative power pattern in the xz-plane for the infinitesimal magnetic dipole impressed source specified in Part A. (b) Corresponding relative error (blue) between the *NFBOR* and *FEKO* magnitudes, in the same plane.

C. Computed Total Fields

Thus far the correctness of *NFBOR* for the computation of scattered fields has been shown. For completeness, we here examine the total fields (that is, the sum of the incident and scattered fields), for the same case as in Part B. The conclusions are the same – excellent agreement between the total fields in the two patterns cuts, and small relative error between *NFBOR* and *FEKO* computations.

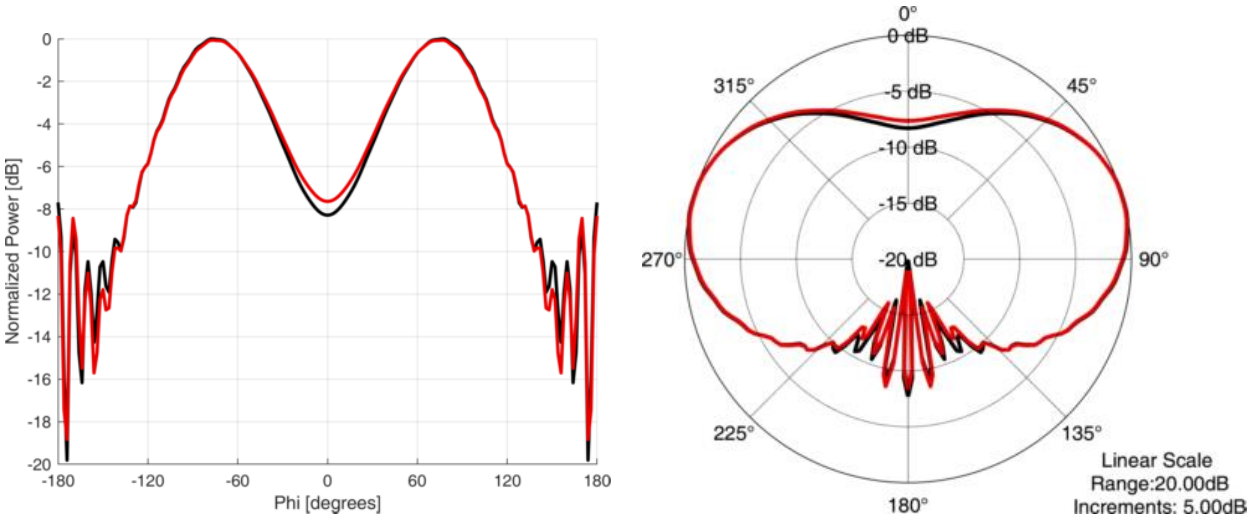

(a) **(b)**

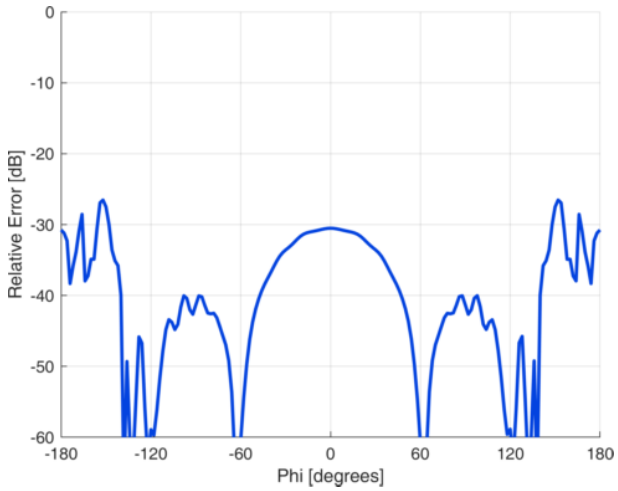

(c)

Fig.4.3-11 : (a) Computed *EFIE- NFBOR* (red) and reference *FEKO* (black) total far-field relative power pattern in the xy-plane for the infinitesimal magnetic dipole impressed source specified in Part A. (b) Corresponding relative error (blue) between the *NFBOR* and *FEKO* magnitudes, in the same plane.

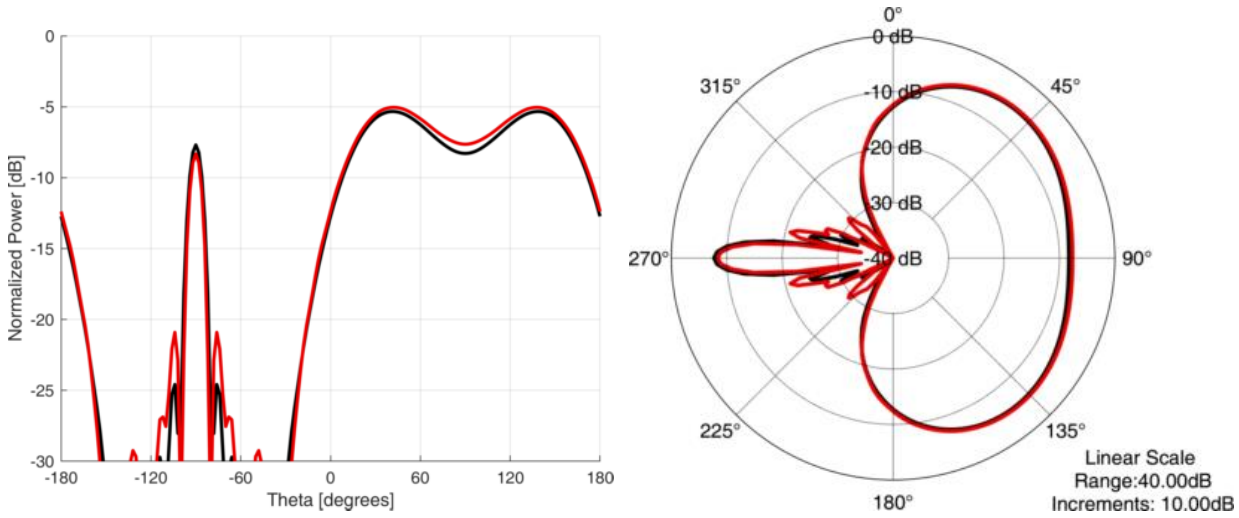

(a) **(b)**

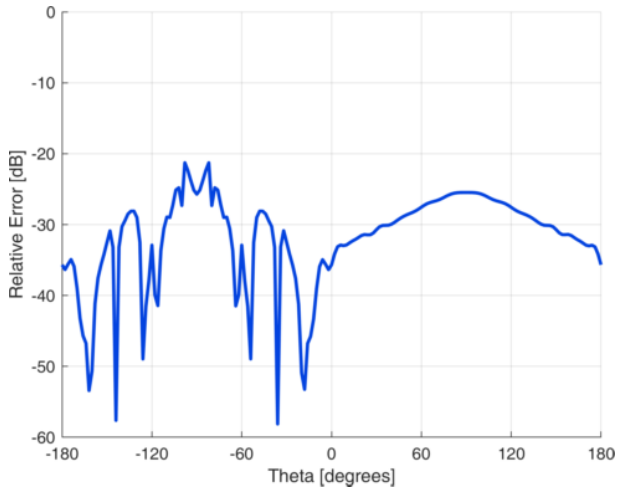

(c)

Fig.4.3-12 : (a) Computed *EFIE- NFBOR* (red) and reference *FEKO* (black) total far-field relative power pattern in the xz-plane for the infinitesimal magnetic dipole impressed source specified in Part A. (b) Corresponding relative error (blue) between the *NFBOR* and *FEKO* magnitudes, in the same plane.

4.3.4 Plane Wave Incidence on a Cone-Sphere

The benchmark problems in Sections 4.3.2 and 4.3.3 all involve a spherical PEC-BOR. In this section we consider a non-spherical BOR. The current density $\overline{J}_{pec}$ induced on the PEC-BOR is much more sensitive measure of solution accuracy than the resulting fields, because the fields are

obtained as integrations over these current densities. We therefore further demonstrate the correctness of the code *NFBOR* by comparing current densities on a cone-sphere (which is much like an ice cream cone) to known solutions. The axis of the cone-sphere is as usual the z-axis, with $z = 0$ at the tip of the cone. The radius of the hemispherical portion of the object is sphere is 0.2λ , and the cone half-angle is 10°. There is a θ-polarised plane wave incident, from direction $(\theta^{inc},\phi^{inc})$ = (180°, 0°), on the cone-sphere. In other words it is an x-polarised incident plane wave.

Fig.4.3-13(a) shows, taken from [MAUT 69], the EFIE-computed surface current density $|J_t|$ (normalised to the magnitude of the incident magnetic field) along the BOR in the xz-plane ($\phi = 0^\circ$) and $|J_\phi|$ along the BOR in the yz-plane ($\phi = 90^\circ$). Symbol N is in fact what we call N_t in this thesis, namely the number of expansion functions used along the generatrix of the BOR. Fig.4.3-13(b) shows the same results computes using the code *NFBOR* developed in this thesis. [MAUT 69] notes that whereas $|J_t|$ converges converges fairly rapidly, $|J_\phi|$ does so more slowly, and concludes that this is due to the sharp tip of the cone. Fig.4.3-14 shows similar results using MFIE-NFBOR and CFIE-BOR, which shows that for this object these exhibit improved convergence compared to EFIE-NFBOR. We conclude that NFBOR performs reliably on non-spherical objects.

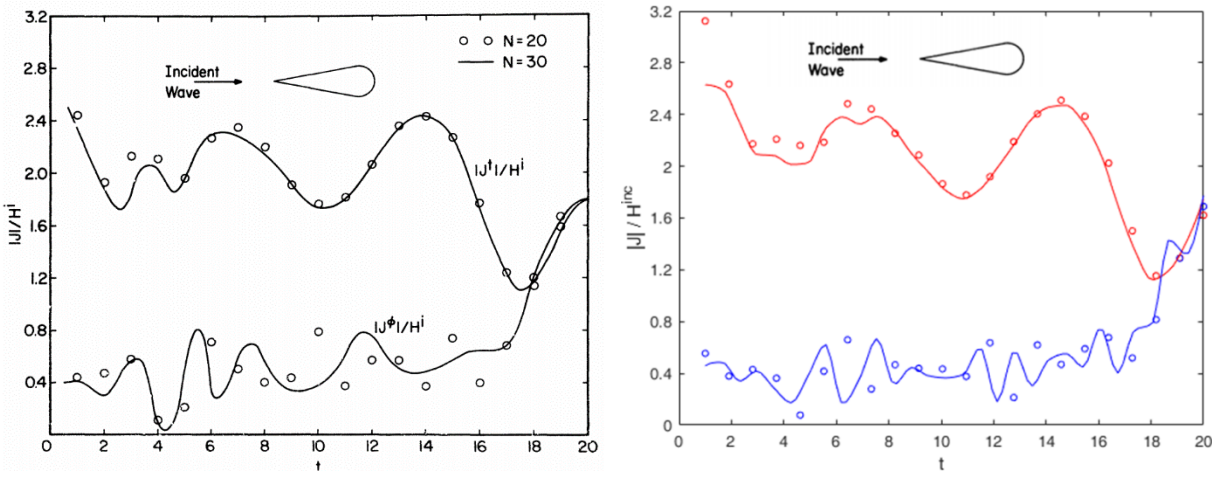

Fig.4.3-13 : (a) EFIE-computed $|J_t|$ and $|J_\phi|$ from [MAUT 69] for the cone-sphere; (b) *EFIE- NFBOR* computed $|J_t|$ (red) and $|J_\phi|$ (blue) for the same cone-sphere, where the dots are for $N_t = 22$ and the solid lines for $N_t = 30$.

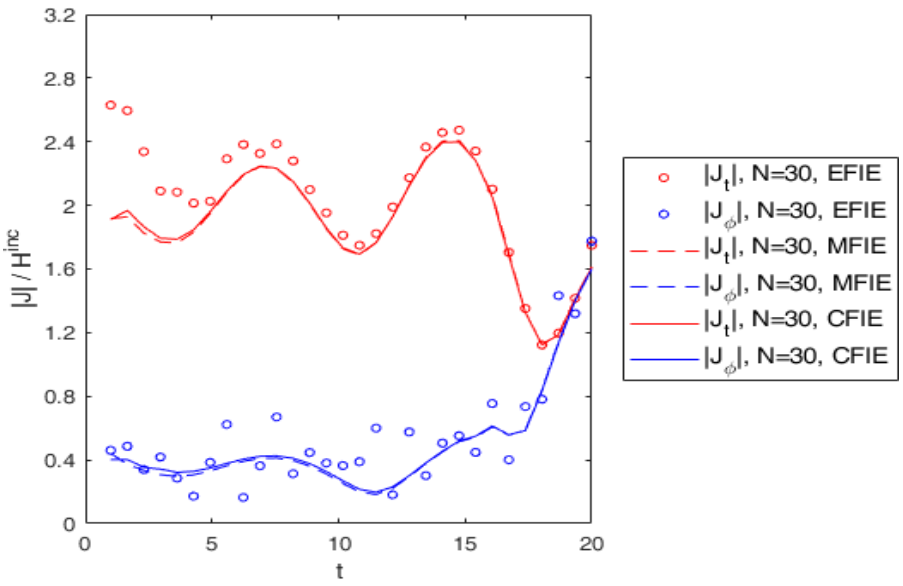

Fig.4.3-14 : *NFBOR*-computed $|J_t|$ and $|J_\phi|$ for the cone-sphere. The *EFIE-NFBOR* results are the same as those given in Fig.4.3-11(b).

4.4 DETERMINING THE INCIDENT FIELDS $\bar{E}^{inc}$ AND $\bar{H}^{inc}$ DUE TO $\bar{M}_s^{NF}$

4.4.1 Preliminary Remarks

In Section 3.3 we explained that the measured quantity $\hat{n}(S_{meas})\times\bar{E}^{NF}(S_{meas})$ is probed over the measurement surface S_{meas} and then via interpolation is known as a continuous function on this surface. This is then viewed as a known 'shroud' of magnetic current density $\bar{M}_s^{NF}(\bar{r}_s)$ via (3.3-2). We next consider how this $\bar{M}_s^{NF}(\bar{r}_s)$ may be used to find $(\bar{E}^{inc},\bar{H}^{inc})$ due to $\bar{M}_s^{NF}$ radiating in free space. Recall that this $(\bar{E}^{inc},\bar{H}^{inc})$ is needed at two different stages of the new NF-to-FF transformation, as explained in Section 3.4, first at points on S_{meas} itself, and then in the far-zone.

4.4.2 Brute Force Approach – Use of the Interpolated Shroud

If we have $\bar{M}_s^{NF}(\bar{r}_s)$ at any point $\bar{r}_s \in S_{meas}$, we could in principle evaluate

$$\bar{E}^{inc}(\bar{r}) = \oiint_{S_{meas}} \tilde{G}_{em}(\bar{r},\bar{r}') \cdot \bar{M}_s^{NF}(\bar{r}')\, dS' \tag{4.4-1}$$

and

$$\bar{H}^{inc}(\bar{r}) = \oiint_{S_{meas}} \tilde{G}_{mm}(\bar{r},\bar{r}') \cdot \bar{M}_s^{NF}(\bar{r}')\, dS' \tag{4.4-2}$$

Detailed expressions for the free-space dyadic Green's functions $\tilde{G}_{em}$ and $\tilde{G}_{mm}$ can be found in closed-form in many texts, such as [VOLA 12] and [KRIS 16].

Expressions (4.4-1) and (4.4-2) are difficult to evaluate numerically in a way that is both computationally efficient and accurate, for observation points in the near-zone. The most numerically favourable form of the integrals is that obtained when the Green's functions are written in terms of the vector and scalar potentials, but then there are spatial derivative operations outside the integral that would have to be numerically evaluated. If the derivatives are moved inside the integrals the integrands become strongly singular for observation points directly on the $\bar{M}_s^{NF}$ distribution itself. In Section 4.4.4 we therefore propose an alternative approach that models $\bar{M}_s^{NF}$ as a shroud of infinitesimal magnetic dipoles. This requires some additional geometrical considerations. These are discussed in Section 4.4.3.

4.4.3 Further Geometrical Information

The discussion in Section 4.2.2 is relevant as the starting point for that discussion in the present section. In Section 4.2.2 we emphasised that through interpolation we have the tangential electric field values at any point on the BOR. In what follows the red dots will still denote the set of acquisition points $\{\bar{r}_q, q = 1,2,....,Q\}$ defined in Section 3.3. As noted in Section 3.3 there is an angular separation $\Delta\phi_{acquire}$ between any two acquired points on the BOR. We will define another set of points $\{\bar{r}_p, p = 1,2,....,P\}$ at which we sample the interpolated tangential electric field values; reasons for doing this will be given in Section 4.4.4.

In order to describe what is done next we first consider the case $P = Q$, for which the number of points $\bar{r}_p$ is equal to the number of acquisition points $\bar{r}_q$, and refer to Fig.4.4-1(a). The red dots are still the acquisition points. Around each such point we have constructed a quadrilateral-like shape; the white lines now do denote[50] regions on the BOR and are not shown merely for pictorial reasons. We call them quadrilateral-like shapes because, whereas all four boundaries of a true quadrilateral are straight lines and its face is planar, the quadrilateral-like shapes have two straight sides and two curved sides (circular[51] arcs), and its face is curved. This is illustrated in Fig.4.4-2. Select for the moment a single generating curve in Fig.4.4-1(a); the black dots on this curve are the points (ρ_i^-, z_i^-) referred to in Section 2.4.3. Rotate the generating curve through an angle $\Delta\phi_{acquire}$, and we have a second line-of-longitude with the same black dots, albeit rotated. If this rotating is done Q_ϕ times we end up with the sketch in Fig.4.4-1(a). Each $\bar{r}_p$ position (the red dots) finds itself located in a quadrilateral-like portion of a frustum representation of the BOR. It is located halfway in angle between two lines-of-longitude, and along this line at $\{\rho, z\} = \left\{(\rho_i^- + \rho_{i+1}^-)/2, (z_i^- + z_{i+1}^-)/2\right\}$.

Next consider cases where $P > Q$. We take the case $P = 2Q$ for purposes of illustration, and refer the reader to Fig.4.4-1(b). There are now more sample points $\bar{r}_p$ (small red dots) than acquisition points (large red dots).

In Section 4.4.4 the area of the portion of the frustum shown in Fig.4.4-2 will be needed, and so is written down here. The length of the straight sides of the portion of the frustum representation of the BOR is

$$\ell = \sqrt{(\rho_{i+1}^- - \rho_i^-)^2 + (z_{i+1}^- - z_i^-)^2} \tag{4.4-3}$$

The complete area of the frustum is

$$A_{\text{frustrum}} = 2\pi\ell\left(\frac{\rho_{i+1}^- + \rho_i^-}{2}\right) = \pi\ell(\rho_{i+1}^- + \rho_i^-) \tag{4.4-4}$$

[50] Unlike those in Fig.4.2-1.
[51] Irrespective of the shape of the BOR.

If the frustum is divided into N_ϕ pieces in azimuth, then the area of each piece is

$$dA = \frac{A_{\text{frustrum}}}{N_\phi} = \frac{\pi \ell (\rho_{i+1}^{-} + \rho_i^{-})}{N_\phi} \tag{4.4-5}$$

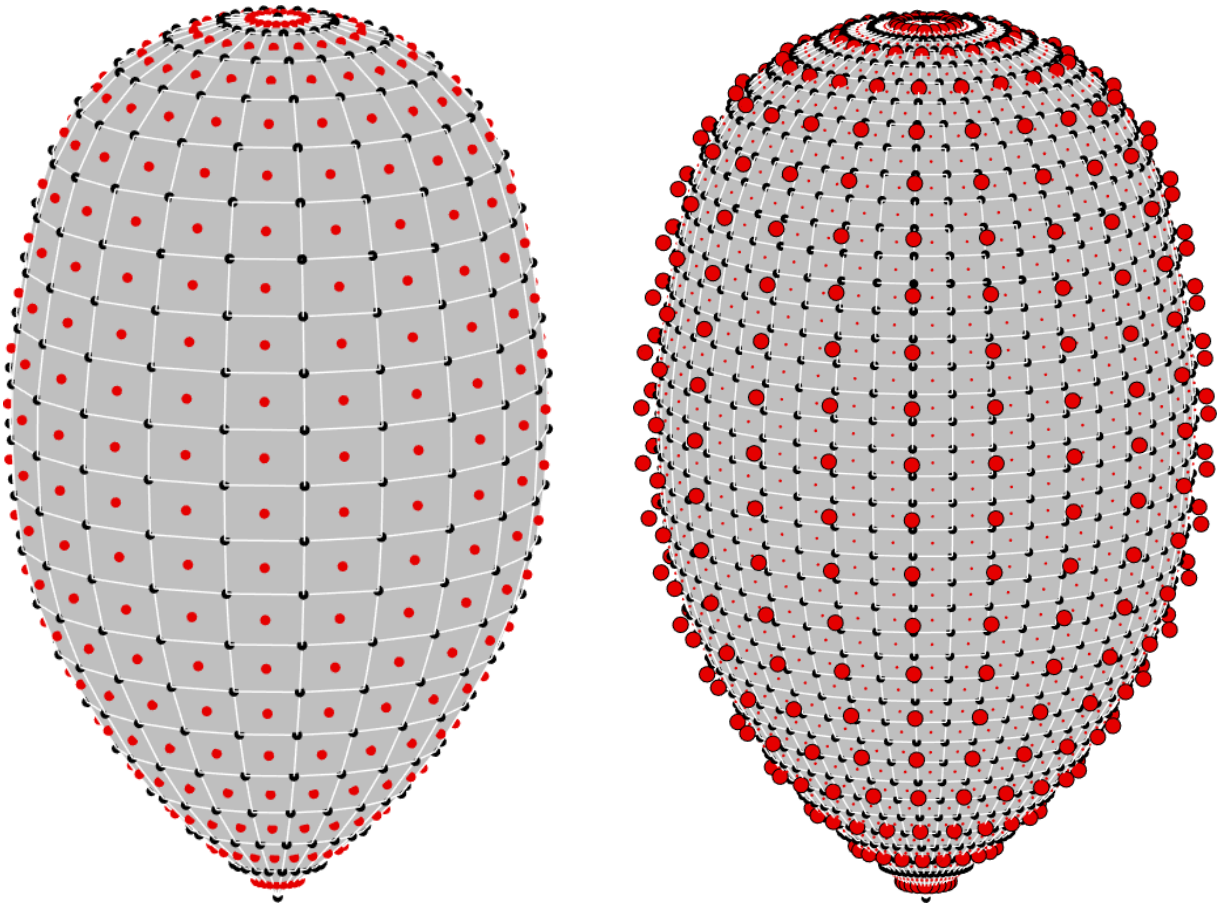

(a) **(b)**

Fig.4.4-1 : (a) Acquisition and sample points (red dots) for the case P = Q; (b) Acquisition points (large red dots) and sample points (small red dots) for the case P = 2Q.

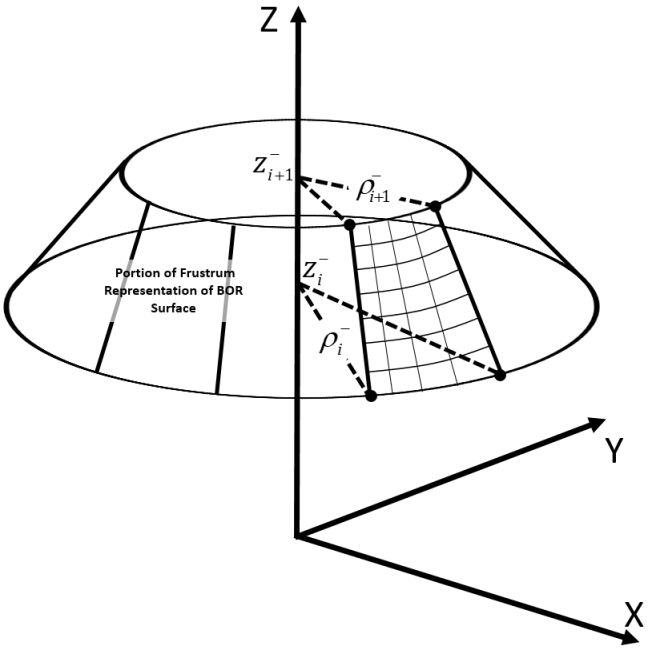

Fig.4.4-2 : Portion of the frustum representation of the BOR measurement surface S_{meas}

4.4.4 Infinitesimal Magnetic Dipole Set Approach

A. Infinitesimal Dipole Positions, Strengths & Orientations

A number of sample points $\{\bar{r}_p, p = 1, 2, ..., P\}$, with $\bar{r}_p \in S_{meas}$ and $P \geq Q$, is selected[52]. The field values at each $\bar{r}_p$ are "converted" to a sampled magnetic current density at each $\bar{r}_p$, as in (3.3-2), namely

$$\bar{M}_s^{NF}(\bar{r}_p) = -\hat{n}(\bar{r}_p) \times \bar{E}^{NF}(\bar{r}_p) = \underbrace{-E_\phi^{NF}(\bar{r}_p)}_{M_t^{NF}(\bar{r}_p)} \hat{t}(\bar{r}_p) + \underbrace{E_t^{NF}(\bar{r}_p)}_{M_\phi^{NF}(\bar{r}_p)} \hat{\phi}(\bar{r}_p) \qquad (4.4\text{-}6)$$

Quantities M_t^{NF} and M_ϕ^{NF} are complex scalars (that is, have a magnitude and phase). At each point $\bar{r}_p$ we imagine that there are two spatially orthogonal infinitesimal magnetic dipoles

$$\bar{p}_{mt}(\bar{r}_p) = M_t^{NF}(\bar{r}_p)\, dA(\bar{r}_p)\, \hat{t}(\bar{r}_p) \qquad (4.4\text{-}7)$$

[52] It is important to remember the purposeful different use of the symbols $\bar{r}_q$, $\bar{r}_p$ and $\bar{r}_s$, all points on S_{meas}. This is summarized for convenience in the "Glossary of Terms" near the front of the thesis.

and

$$\bar{p}_{m\phi}(\bar{r}_p) = M_{\phi}^{NF}(\bar{r}_p)\; dA(\bar{r}_p)\; \hat{\phi}(\bar{r}_p) \tag{4.4-8}$$

The factor $dA(\bar{r}_p)$, shown in Section 4.4.2 to be related to the differential geometry of the frustum representation of the BOR, accounts for the elemental surface element that appears in (4.4-1) and (4.4-2). By accounting for the measurement density and surface geometry in this way, non-uniform sets of sampling densities may be 'corrected' and be made compatible.

We will use the symbol $\bar{E}^{inc}\{\bar{p}_{mt}(\bar{r}_p), \bar{p}_{m\phi}(\bar{r}_p), \bar{r}\}$ to denote the electric field at any point $\bar{r}$ in space, due to $\bar{p}_{mt}(\bar{r}_p)$ and $\bar{p}_{m\phi}(\bar{r}_p)$, radiating together in free space. A similar meaning is attached to $\bar{H}^{inc}\{\bar{p}_{mt}(\bar{r}_p), \bar{p}_{m\phi}(\bar{r}_p), \bar{r}\}$. The incident fields due to the shroud of magnetic current density is then approximated as

$$\bar{E}^{inc}\{\bar{M}_s^{NF}, \bar{r}\} = \sum_{p=1}^{P} \bar{E}^{inc}\{\bar{p}_{mt}(\bar{r}_p), \bar{p}_{m\phi}(\bar{r}_p), \bar{r}\} = \sum_{p=1}^{P} \bar{E}^{inc}\{\bar{p}_{mt}(\bar{r}_p), \bar{r}\} + \sum_{p=1}^{P} \bar{E}^{inc}\{\bar{p}_{m\phi}(\bar{r}_p), \bar{r}\} \tag{4.4-9}$$

and

$$\bar{H}^{inc}\{\bar{M}_s^{NF}, \bar{r}\} = \sum_{p=1}^{P} \bar{H}^{inc}\{\bar{p}_{mt}(\bar{r}_p), \bar{p}_{m\phi}(\bar{r}_p), \bar{r}\} = \sum_{p=1}^{P} \bar{H}^{inc}\{\bar{p}_{mt}(\bar{r}_p), \bar{r}\} + \sum_{p=1}^{P} \bar{H}^{inc}\{\bar{p}_{m\phi}(\bar{r}_p), \bar{r}\} \tag{4.4-10}$$

B. Approach Used to Find the Fields of an Arbitrarily Oriented and Located Infinitesimal Dipole at Any Point in Space

Expressions are provided in Appendix C for the exact fields at any point $\bar{r}$ in space of a z-directed infinitesimal magnetic dipole located at the origin of the global coordinate system. It is clear from Part A that we will need to be able to determine the fields, at any point $\bar{r}$ in space, of an infinitesimal magnetic dipole $\bar{p}_m(\bar{r}_p) = \hat{\xi} A_{\mathrm{m}}$, where $\hat{\xi}$ is the orientation of the dipole, $\bar{r}_p$ its location, and A_m its strength. This can be done using the coordinate and vector component transformations described in Appendix D, along with the field expressions in Appendix C. This is shown in Part C and Part D below for $\hat{t}$-directed and $\hat{\phi}$-directed infinitesimal magnetic dipoles, respectively.

C. Fields of the Infinitesimal Dipole $\bar{p}_{mt}(\bar{r}_p)$

The goal of this section is to explain the evaluation of constituents of expressions (4.4-8) and (4.4-9), namely the fields due to a single $\hat{t}$-directed magnetic dipole in both the near-zone and the far-zone. The general approach to evaluation of these fields in the latter two zones is similar but not identical, and so the approaches are considered separately. The reader is referred to Appendix D for the groundwork.

■ **Near-Zone Fields** $\bar{E}^{inc}\{\bar{p}_{mt}(\bar{r}_p), \bar{r}\}$ ***and*** $\bar{H}^{inc}\{\bar{p}_{mt}(\bar{r}_p), \bar{r}\}$

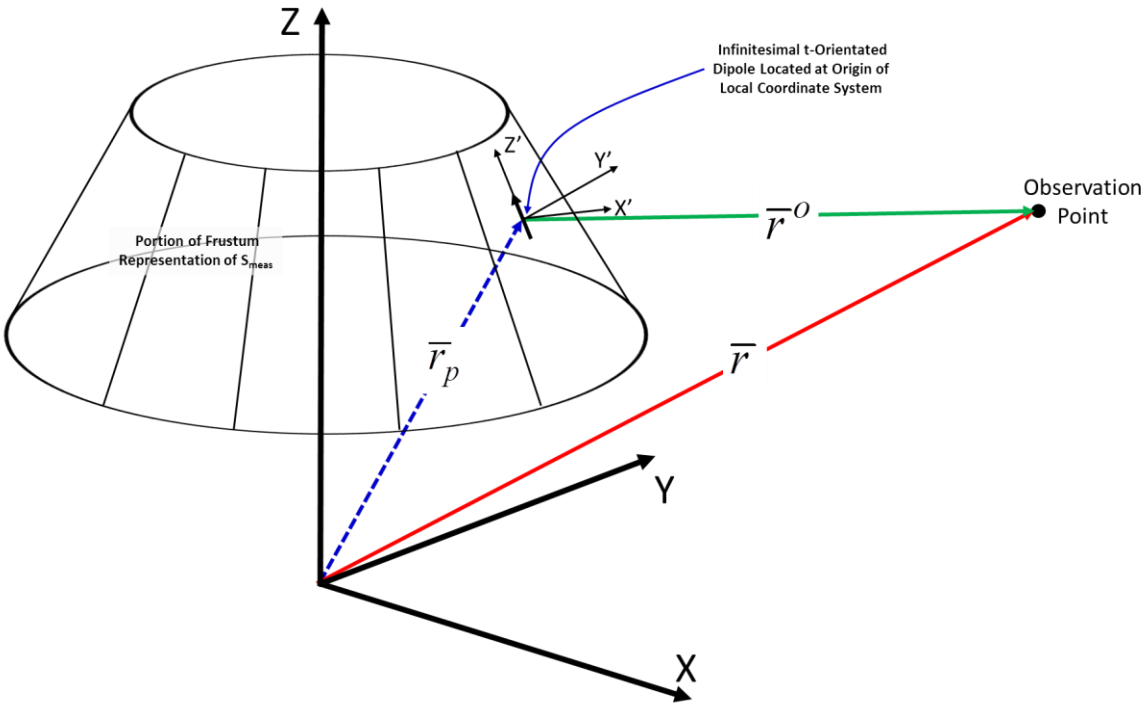

Fig.4.4-3 : Diagram accompanying the determination of the near-zone fields $\bar{E}^{inc}\{\bar{p}_{mt}(\bar{r}_p), \bar{r}\}$ **and** $\bar{H}^{inc}\{\bar{p}_{mt}(\bar{r}_p), \bar{r}\}$ **in the global coordinate system.**

● **Define the dipole source location on the BOR :** The magnetic dipole location, in the unprimed, global, coordinate system is $\bar{r}_p = (x_p, y_p, z_p)$, and is coincident with the location of the origin of the local coordinate system. Point (x_p, y_p, z_p) replaces (τ_x, τ_y, τ_z) of Appendix D.

● **Define the field observation coordinates :** The observation point, in the unprimed coordinate system is given by expression (D-11) and denoted by $\bar{r} = (x, y, z) = (r, \theta, \phi)$. This same observation point is at $\bar{r}^{\,o}$ relative to the dipole. We seek the fields at this observation point, and want their components expressed as spherical components in the unprimed (global) coordinate system $\bar{E}^s(\bar{r}) = \bar{E}(r, \theta, \phi)$ and $\bar{H}^s(\bar{r}) = \bar{H}(r, \theta, \phi)$. The approach is to first find the field in the natural system of the dipole, and then transform the vector from local to global coordinates. The fields are most easily evaluated at the observation point in the local system, at the observation point relative to the dipole, as shown in Appendix C.

● **Define the dipole's local, or primed, coordinate system :** At $\bar{r}_p = (x_p, y_p, z_p)$ we have three local unit vectors defined in terms of the global coordinate system as

$$\hat{n} = n_x \hat{x} + n_y \hat{y} + n_z \hat{z} \tag{4.4-11}$$

$$\hat{\phi} = \phi_x \hat{x} + \phi_y \hat{y} + \phi_z \hat{z} \tag{4.4-12}$$

$$\hat{t} = t_x \hat{x} + t_y \hat{y} + t_z \hat{z} \tag{4.4-13}$$

We orient the primed coordinate system so that the z'-axis is parallel to the local unit vector $\hat{t}$, the y'-axis parallel to the local unit vector $\hat{\phi}$ and the x'-axis parallel to the local unit surface normal $\hat{n}$. In other words,

$$\hat{z}' = \hat{t} = t_x \hat{x} + t_y \hat{y} + t_z \hat{z} \tag{4.4-14}$$

$$\hat{y} = \hat{\phi} = \phi_x \hat{x} + \phi_y \hat{y} + \phi_z \hat{z} \tag{4.4-15}$$

and

$$\hat{x}' = \hat{n} = n_x \hat{x} + n_y \hat{y} + n_z \hat{z} \tag{4.4-16}$$

We have thus correlated the orientation and position of the dipole's natural coordinate system, with that of the body-of-revolution.

● **Solve for the field in the dipole's natural coordinate system :** The natural coordinate system of the dipole is one in which the dipole's axis is aligned with the coordinate system's z-axis, with

the dipole is itself located at the origin and the observation point expressed relative to the dipole. To compute the magnetic dipole vector field quantities according to Appendix C, we must be in this local system. To perform this calculation for our present geometry and orientation, we will need to bring the primed system into alignment with the unprimed global system, remove the offset between the two systems, and then solve for the field at the observation point which itself must be expressed in the primed system.

To affect the alignment of the unprimed system into the primed system, we will use the transforms $[A]_c^{c'}$ and it's inverse, $[A]_{c'}^{c}$, of Appendix D to go easily back and forth between primed and unprimed systems. The first step in computing these transforms is to determine the Euler angles (α, β, γ) via the algorithm in [NIKO 18]. Given the Euler angles, it is now a straightforward matter to transform a vector written in term of it rectangular components in the unprimed system to the primed system, $[A]_c^{c'}$, and the inverse transform taking a vector from a Cartesian basis in the primed system, to that of the unprimed system, $[A]_{c'}^{c}$.

We now compute the vector offset

$$\bar{r}^{o} = (x^{o}, y^{o}, z^{o}) = \bar{r} - \bar{r}_{p} \tag{4.4-17}$$

which is a vector from the primed origin to the observation point, itself expressed in Cartesian coordinates of the unprimed system. We can translate $\bar{r}^{o}$ into the primed coordinate system via

$$\bar{r}^{o'} = [A]_c^{c'} \bar{r}^{o} \tag{4.4-18}$$

hence explicitly indicating the position at which the field is to be calculated, in its 'natural system'.

The fields of the magnetic dipole, as outlined in Appendix C are thus now computed at this point, $\bar{r}^{o'}$, and are expressed in the primed system, on a spherical basis as

$$\bar{E}' = \bar{E}^{'s'} = \begin{bmatrix} E'_{r'}(r', \theta', \phi') \\ E'_{\theta'}(r', \theta', \phi') \\ E'_{\phi'}(r', \theta', \phi') \end{bmatrix} \tag{4.4-19}$$

and

$$\bar{H}' = \bar{H}^{'s'} = \begin{bmatrix} H'_{r'}(r',\theta',\phi') \\ H'_{\theta'}(r',\theta',\phi') \\ H'_{\phi'}(r',\theta',\phi') \end{bmatrix} \tag{4.4-20}$$

● **Transform field to the unprimed (global) system :** The final step of the field-calculation is to transform the fields into the spherical basis of the unprimed system. The first step is to compute the spherical-to-Cartesian transform $[T]_{s'}^{c'}$ using the θ' and ϕ' angles substituted into equation (D-2) of Appendix D, and the Cartesian-to-spherical transform $[T]_s^c$ in the unprimed system using θ and ϕ in (D-3). We may then use the result (D-9) from the same appendix, and do this in a single step for the electric and magnetic in turn, as

$$\bar{E} = \bar{E}^s = \begin{bmatrix} E_r(r,\theta,\phi) \\ E_\theta(r,\theta,\phi) \\ E_\phi(r,\theta,\phi) \end{bmatrix} = [T]_c^s\,[A]_{c'}^c\,[T]_{s'}^{c'} \begin{bmatrix} E'_{r'}(r',\theta',\phi') \\ E'_{\theta'}(r',\theta',\phi') \\ E'_{\phi'}(r',\theta',\phi') \end{bmatrix} \tag{4.4-21}$$

and

$$\bar{H} = \bar{H}^s = \begin{bmatrix} H_r(r,\theta,\phi) \\ H_\theta(r,\theta,\phi) \\ H_\phi(r,\theta,\phi) \end{bmatrix} = [T]_c^s\,[A]_{c'}^c\,[T]_{s'}^{c'} \begin{bmatrix} H'_{r'}(r',\theta',\phi') \\ H'_{\theta'}(r',\theta',\phi') \\ H'_{\phi'}(r',\theta',\phi') \end{bmatrix} \tag{4.4-22}$$

In summary, the above process is a series of translations on the fields found originally expressed in a spherical basis in the primed (natural) system, to a Cartesian-basis in the primed system, followed by a change of basis into the unprimed (global) Cartesian system, followed, finally, by a conversion to a spherical basis in the unprimed system.

It is worth emphasizing that vectors $\bar{E}^{'s'}$ and $\bar{E}^s$ are the same vectors observed at the same physical point in space. Field $\bar{E}^s$ is expressed in terms of the coordinates of the point expressed in the spherical coordinates of the unprimed system, and in terms of the spherical components of the unprimed system. Field $\bar{E}^{'s'}$ is expressed in terms of the coordinates of the point expressed in

the spherical coordinates of the primed system, and in terms of the spherical components of the primed system.

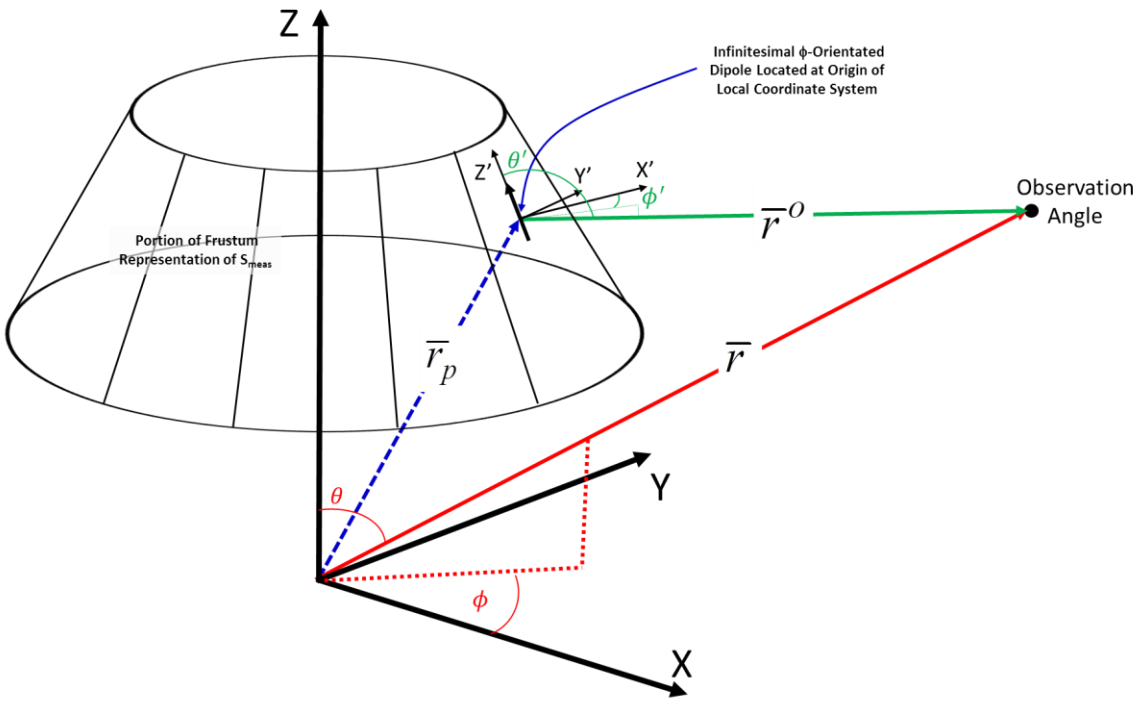

Fig.4.4-4 : Diagram accompanying the determination of the far-zone fields $\bar{E}^{inc}\{\bar{p}_{mt}(\bar{r}_p),\theta,\phi\}$ *and* $\bar{H}^{inc}\{\bar{p}_{mt}(\bar{r}_p),\theta,\phi\}$ in the global coordinate system.

■ Far-Zone Fields $\bar{E}^{inc}\{\bar{p}_{mt}(\bar{r}_p),\theta,\phi\}$ *and* $\bar{H}^{inc}\{\bar{p}_{mt}(\bar{r}_p),\theta,\phi\}$

The approach will be similar to that carried out for the near-zone fields. We bring the dipole, whose local primed system is aligned to the BOR, coincident with the unprimed axis by using the transforms associated with the Euler angles (α,β,γ) and then evaluate the field in this 'natural system' once $\bar{r}^{o}$ is expressed in the primed coordinate system, denoted as $\bar{r}^{o'}$. The field vectors are then transformed into the spherical coordinates of the unprimed system. The dipole is located at $\bar{r}_p=(x_p,y_p,z_p)$ as before. What was previously an observation point, at a finite position from the said dipole, is replaced by an observation direction[53]. Thus, instead of a 3-vector indicating the observation point, we now have (θ,ϕ) denoting the observation direction,

[53] The distance factor is removed in far-zone expressions.

as viewed from the origin. We seek the fields in this direction, and as before, it is required that their spherical components are expressed in the unprimed system.

● **Define the far-zone direction for we wish to evaluate the field :** As before, we will evaluate the far-zone field observation direction in the natural coordinates of the dipole. From the dipole's position at $\bar{r}_p = \left(x_p, y_p, z_p\right)$, the observation angle is located at a different set of directions, $\bar{r}^o = (\theta', \phi')$, whereas in the unprimed system, that same observation angle is expressed as $\bar{r} = (\theta, \phi)$.

● **Define the dipole's orientation & local, or primed, coordinate system :** The dipole's orientation on the BOR is identical as before, with the primed coordinate system aligned so that the z'-axis is parallel to the local unit vector $\hat{t}$, the y'-axis parallel to the local unit vector $\hat{\phi}$ and the x'-axis is parallel to the surface normal, $\hat{n}$.

Again, the Euler angles (α, β, γ) are determined via the algorithm in [NIKO 18], which enables direct computation of $[A]_c^{c'}$ and $[A]_{c'}^{c}$ transforms to achieve the change-of-basis between primed and unprimed systems.

The direction vector $\bar{r}^o = (\theta', \phi')$ may now be transformed into the primed coordinate system via

$$\bar{r}^{o'} = [A]_c^{c'} \bar{r}^o(\theta', \phi') \tag{4.4-23}$$

The values for θ' and ϕ' are computed using the results (D-14) and (D-15) from Appendix D. This then enables us to compute the transformation from spherical-to-Cartesian in the primed system, $[T]_{s'}^{c'}$, directly using (D-3) from Appendix D.

● **Solve for the far-zone field in the dipole's natural coordinate system :** Armed with these results, we can now evaluate the far-zone dipole expressions (C-7) through (C-12) in Appendix

C, in the direction $\bar{r}^{o'}$, all in the natural coordinate system. Recall that $\bar{r}'^{o'}$ is the observation angle, as expressed in the local coordinate system.

The fields computed in this way represent the fields we would observe at the correct observation angle, but with the dipole located at the origin, giving vector quantities $E_\theta^{ORIG}(\theta,\phi)$, $E_\phi^{ORIG}(\theta,\phi)$ & $E_r^{ORIG}(\theta,\phi)$ of Appendix D.

In order to reflect the phase offset of the dipole's location $\bar{r}_p = (x_p, y_p, z_p)$, we need to compute the fields, per (D-17) - (D-19), in the primed coordinate system

$$E_\theta^{'s'} = E_\theta^{shift}(\theta,\phi) = E_\theta^{ORIG}(\theta,\phi)\, e^{jk_0 x_p \sin\theta\cos\phi}\; e^{jk_0 y_p \sin\theta\sin\phi}\; e^{jk_0 z_p \cos\phi} \tag{4.4-24}$$

$$E_\phi^{'s'} = E_\phi^{shift}(\theta,\phi) = E_\phi^{ORIG}(\theta,\phi)\, e^{jk_0 x_p \sin\theta\cos\phi}\; e^{jk_0 y_p \sin\theta\sin\phi}\; e^{jk_0 z_p \cos\phi} \tag{4.4-25}$$

and

$$E_r^{'s'} = E_r^{shift}(\theta,\phi) = E_r^{ORIG}(\theta,\phi)\, e^{jk_0 x_p \sin\theta\cos\phi}\; e^{jk_0 y_p \sin\theta\sin\phi}\; e^{jk_0 z_p \cos\phi} \tag{4.4-26}$$

or simply, $E^{'s'} = [E_r^{'s'}, E_\theta^{'s'}, E_\phi^{'s'}]^T$. This is the field, expressed in a spherical basis, in the primed coordinate system.

● **Transform the far-zone field to the unprimed (global) system basis :** Using θ and ϕ in the unprimed system we can solve for $[T]_s^c$ directly from (D-3) In the same way, using the values for θ' and ϕ', we can directly compute $[T]_{s'}^{c'}$. Using these results, we may now transform the vector $E^{'s'} = [E_r^{'s'}, E_\theta^{'s'}, E_\phi^{'s'}]^T$ to a spherical basis in the unprimed system via:

$$\bar{E} = \bar{E}^s = \begin{bmatrix} E_r(\theta,\phi) \\ E_\theta(\theta,\phi) \\ E_\phi(\theta,\phi) \end{bmatrix} = [T]_c^s\, [A]_{c'}^c\, [T]_{s'}^{c'} \begin{bmatrix} E'_{r'}(\theta',\phi') \\ E'_{\theta'}(\theta',\phi') \\ E'_{\phi'}(\theta',\phi') \end{bmatrix} = [T]_c^s\, [A]_{c'}^c\, [T]_{s'}^{c'}\, \bar{E}^{'s'} \tag{4.4-27}$$

with similar expressions applying to the magnetic field, if needed.

D. Fields of the Infinitesimal Dipoles $\bar{p}_{m\phi}(\bar{r}_p)$

The goal of this section is to explain the evaluation of constituents of expressions (4.4-7) and (4.4-8) due to a single $\hat{\phi}$-directed magnetic dipole in both the near-zone and the far-zone. The general approach to evaluation of these fields in the latter two zones is similar but not identical, and so the approaches are considered separately. Figures. 4.4-5 and 4.4-6 are relevant.

■ **Near-Zone Fields** $\bar{E}^{inc}\{\bar{p}_{m\phi}(\bar{r}_p),\, \bar{r}\}$ ***and*** $\bar{H}^{inc}\{\bar{p}_{m\phi}(\bar{r}_p),\, \bar{r}\}$

The process is identical to the preceding section, except we now orient the primed coordinate system so that the z'-axis is parallel to the local unit vector $\hat{\phi}$, the y'-axis parallel to the local unit normal vector $\hat{n}$, and the x'-axis parallel to the local unit vector $\hat{t}$. In other words,

$$\hat{z}' = \hat{\phi} = \phi_x \hat{x} + \phi_y \hat{y} + \phi_z \hat{z} \tag{4.4-28}$$

$$\hat{y}' = \hat{n} = n_x \hat{x} + n_y \hat{y} + n_z \hat{z} \tag{4.4-29}$$

and

$$\hat{x}' = \hat{t} = t_x \hat{x} + t_y \hat{y} + t_z \hat{z} \tag{4.4-30}$$

■ **Far-Zone Fields** $\bar{E}^{inc}\{\bar{p}_{m\phi}(\bar{r}_p), \theta, \phi\}$ ***and*** $\bar{H}^{inc}\{\bar{p}_{m\phi}(\bar{r}_p),\, \theta, \phi\}$

The far-zone field evaluation for the $\bar{p}_{m\phi}(\bar{r}_p)$ element is identical to that of the far-zone calculation for the $\bar{p}_{mt}(\bar{r}_p)$ expression, but using the local coordinate system above.

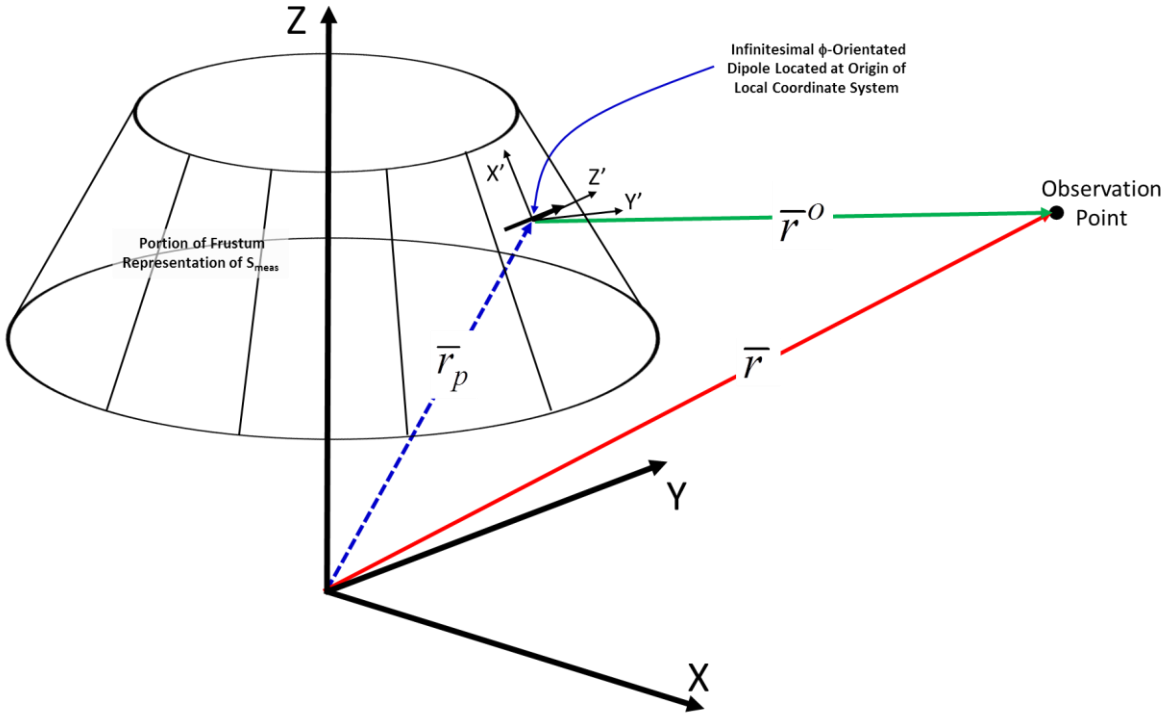

Fig.4.4-5 : Diagram accompanying the determination of the near-zone fields $\bar{E}^{inc}\{\bar{p}_{m\phi}(\bar{r}_p), \bar{r}\}$ and $\bar{H}^{inc}\{\bar{p}_{m\phi}(\bar{r}_p), \bar{r}\}$ in the global coordinate system.

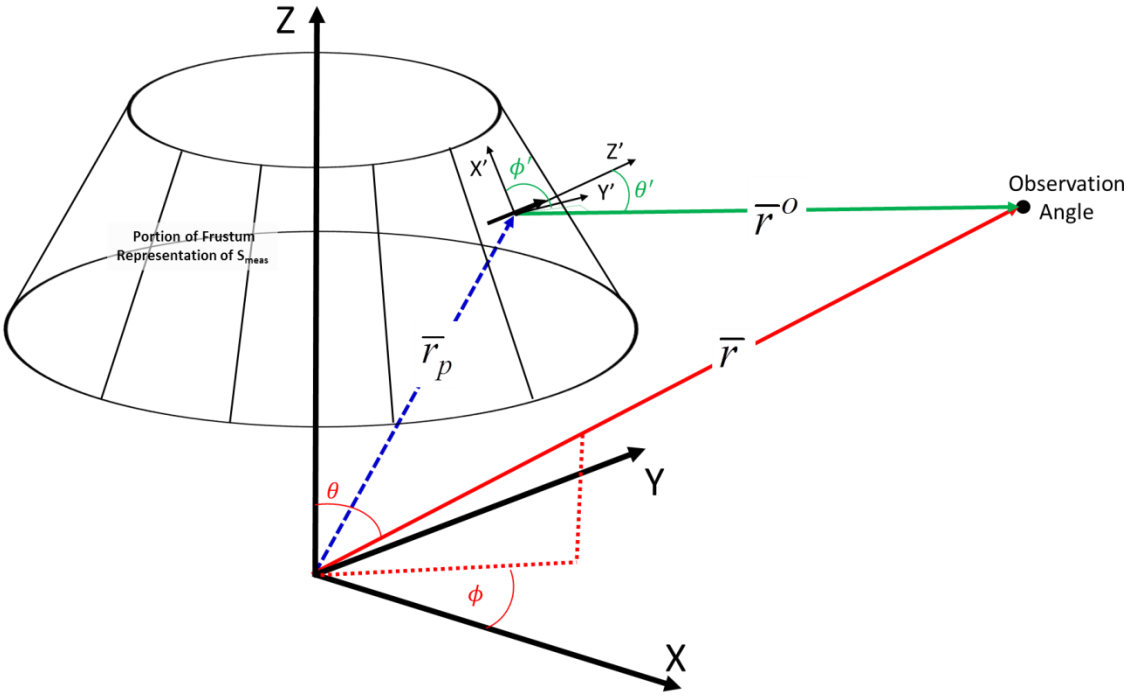

Fig.4.4-6 : Diagram accompanying the determination of the far-zone fields $\bar{E}^{inc}\{\bar{p}_{m\phi}(\bar{r}_p), \theta, \phi\}$ *and* $\bar{H}^{inc}\{\bar{p}_{m\phi}(\bar{r}_p), \theta, \phi\}$ in the global coordinate system.

4.5 TESTING OF THE SHROUD OF INFINITESIMAL ELECTRIC & MAGNETIC DIPOLES FOR 25-ELEMENT PLANAR ARRAY AUT – *FAR-ZONE RESULTS*

4.5.1 Numerical Test Plan

■ We refer to Fig.4.5-1. Surface S_{meas} is in the near-zone of the AUT, and is a spherical surface of radius[54] $R_{meas} = 3\lambda$. We choose this measurement surface because this distance is slightly larger than the MRS of our AUT (2.8λ), and is slightly more than 10x the approximate FF-distance (32λ) of the AUT, per Table E-1. We also found in the literature a radial distance of 3λ was used as a NF measurement surface in [JANS 19].

■ The fields of AUT are computed analytically at sample points on the measurement surface S_{meas}, and are denoted $\bar{E}^{NF}\{AUT, S_{meas}\}$ and $\bar{H}^{NF}\{AUT, S_{meas}\}$. These can be considered exact. Using these we can easily find $\hat{n}\times\bar{E}^{NF}\{AUT, S_{meas}\}$ and $\hat{n}\times\bar{H}^{NF}\{AUT, S_{meas}\}$. The quantity $\hat{n}\times\bar{E}^{NF}\{AUT, S_{meas}\}$ emulates what would be acquired on an actual NF test range. However, $\hat{n}\times\bar{H}^{NF}\{AUT, S_{meas}\}$ would normally not be available[55] on an actual NF test range.

■ The fields of AUT are also directly[56] computed analytically in directions (θ,ϕ) in the far-zone of the AUT and are denoted by $\bar{E}^{exact}\{AUT,\theta,\phi\}$ and $\bar{H}^{exact}\{AUT,\theta,\phi\}$.

■ Equivalent infinitesimal electric ($\bar{p}_e$) and magnetic ($\bar{p}_m$) dipole sets are found at the sample points $\{\bar{r}_p, p = 1,2,....,P\}$ on S_{meas} using $\hat{n}\times\bar{E}^{NF}\{AUT,\bar{r}_p\}$ and $\hat{n}\times\bar{H}^{NF}\{AUT,\bar{r}_p\}$, respectively, as described in Section 4.4.5.

■ We then find the far-zone fields $\bar{E}\{\bar{p}_m,\theta,\phi\}$ and $\bar{H}\{\bar{p}_m,\theta,\phi\}$ due to *only* the shroud of equivalent magnetic dipoles.

■ We similarly find the far-zone fields $\bar{E}\{\bar{p}_e,\theta,\phi\}$ and $\bar{H}\{\bar{p}_e,\theta,\phi\}$ due to *only* the shroud of equivalent electric dipoles.

■ According to the surface equivalence theorem we should find that

$$\bar{E}\{AUT,\theta,\phi\} = \bar{E}\{\bar{p}_e,\theta,\phi\} + \bar{E}\{\bar{p}_m,\theta,\phi\} \tag{4.5-1}$$

and

$$\bar{H}\{AUT,\theta,\phi\} = \bar{H}\{\bar{p}_e,\theta,\phi\} + \bar{H}\{\bar{p}_m,\theta,\phi\} \tag{4.5-2}$$

---

[54] As stated in Table E-1.

[55] But is available here for the purpose of this test to establish the effectiveness of using shrouds of magnetic and electric infinitesimal dipoles to represent actual fields, due to the surface equivalence principle currents $\bar{J}_s$ and $\bar{M}_s$.

[56] By "directly" we mean that there is no NF-to-FF transformation used.

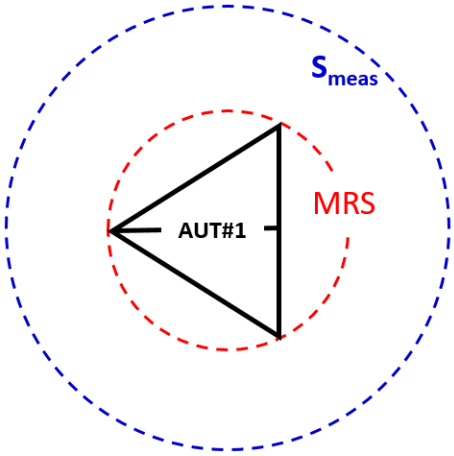

Fig.4.5-1 : Spherical surfaces surrounding AUT

4.5.2 Numerical Test Results

We saw in Section 1.2 that for a minimum sphere of radius MRS, the near field $\hat{n}\times\bar{E}^{NF}(S_{meas})$ needs to be sampled over a spherical S_{meas} of radius $R_{meas}\approx 2\times MRS$. As per the parameters of the 25-element planar array AUT given in Table E-1 this means that $R_{meas}=739.2\,\text{mm}$ and $\Delta\theta=\Delta\phi=2.18^{\circ}$. This would result in $\hat{n}\times\bar{E}^{NF}(S_{meas})$ being sampled at the set of points $\{\bar{r}_q, p=1,2,....,Q\}$. Interpolation is used to increase the sampling density so that $\hat{n}\times\bar{E}^{NF}(S_{meas})$ is known at the set of points $\{\bar{r}_p, p=1,2,....,P\}$.

If we had used a continuous shroud for currents $\bar{J}_s$ and $\bar{M}_s$, instead of representing them by sets of weighted discrete infinitesimal dipoles $\bar{p}_e$ and $\bar{p}_m$, respectively, then we would have found that the sum of their fields is identical to $\bar{E}^{exact}\{AUT,\theta,\phi\}$, shown in Fig.E-1. This is demanded by the surface equivalence principle. Fig.4.5-2 shows that the sum, of $\bar{E}\{\bar{p}_m,\theta,\phi\}$ in (a) and $\bar{E}\{\bar{p}_e,\theta,\phi\}$ in (b), which is shown in (c), is indeed almost indistinguishable from $\bar{E}^{exact}\{AUT,\theta,\phi\}$ plotted in Fig.E-1. Although illustrative, the 3D depictions in Fig.4.5-2 do not easily permit a quantitative assessment of the closeness of field predictions. We therefore show the field in two pattern cuts, normalized to the maximum of the 3D pattern. Fig.4.5-3 plots the

exact far-zone pattern $\left|\bar{E}^{exact}\{AUT,\theta,\phi\}\right|$ and the pattern $\left|\bar{E}\{\bar{p}_e,\theta,\phi\}+\bar{E}\{\bar{p}_m,\theta,\phi\}\right|$ in the xy-plane, and Fig.4.5-4 the same in the xz-plane. In plots (a) of both figures the two are indistinguishable. More revealing is the relative error, as defined in expression (4.3-9), in plots (b) of the two figures. In both planes this is below -80 dB. Thus the infinitesimal dipole representations in fact faithfully represent the far-zone fields of the continuous shrouds $\bar{J}_s$ and $\bar{M}_s$, giving us the correct far-zone radiation patterns. Fig.4.5-2(a) shows that (at least for the AUT under study) the shroud of $\bar{M}_s$, or equivalently $\bar{E}\{\bar{p}_m,\theta,\phi\}$, already provides a far-zone pattern reminiscent of $\bar{E}^{exact}\{AUT,\theta,\phi\}$. The fine-structure (eg. sidelobe details) are supplied by $\bar{E}\{\bar{p}_e,\theta,\phi\}$. In practice we would not know $\bar{E}\{\bar{p}_e,\theta,\phi\}$; it is instead found as the scattered field from the PEC-BOR as part of the NF-to-FF transformation proposed in this thesis.

The same tests were carried out with the AUT moved away to different locations within the same spherical surface S_{meas}, in other words not located at the centre of S_{meas}. So too with the AUT located at several positions within a non-spherical S_{meas} of the same shape as in Fig.2.4-1, and when S_{meas} is a prolate spheroid[57]. In all cases, although the relative contributions of and $\left|\bar{E}\{\bar{p}_m,\theta,\phi\}\right|$ and $\left|\bar{E}\{\bar{p}_e,\theta,\phi\}\right|$ vary, the relative error between $\left|\bar{E}^{exact}\{AUT,\theta,\phi\}\right|$ and $\left|\bar{E}\{\bar{p}_e,\theta,\phi\}+\bar{E}\{\bar{p}_m,\theta,\phi\}\right|$ was less than -80 dB.

[57] Recall that a surface generated by a half-revolution of an ellipse about its major axis is a prolate spheroid, whereas one generated by rotation about its minor axis is an oblate spheroid.

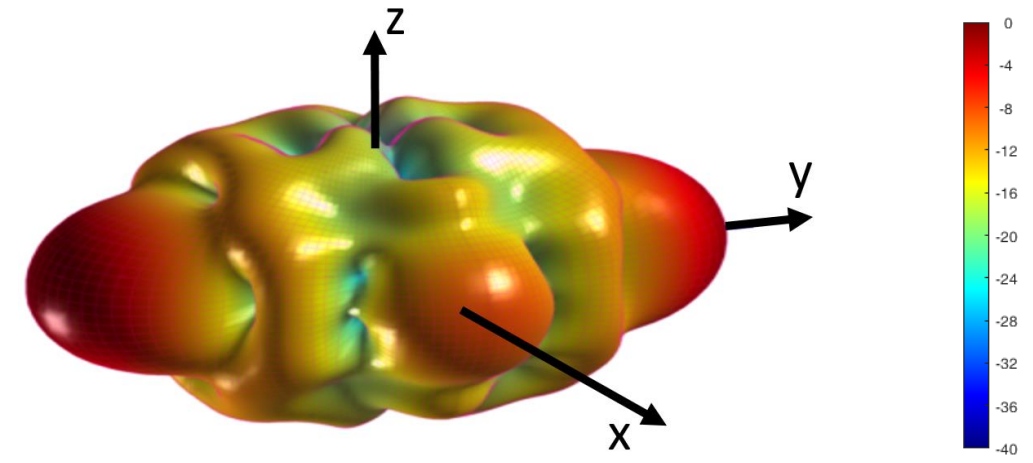

(a)

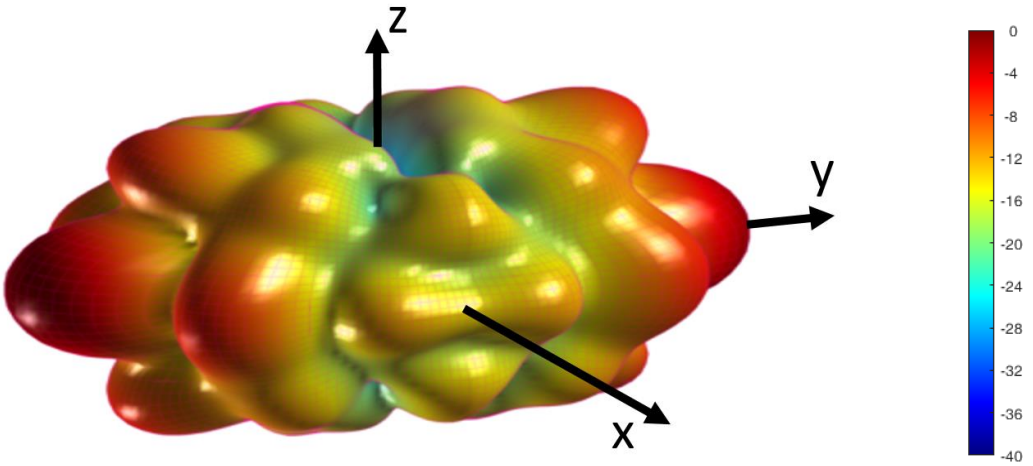

(b)

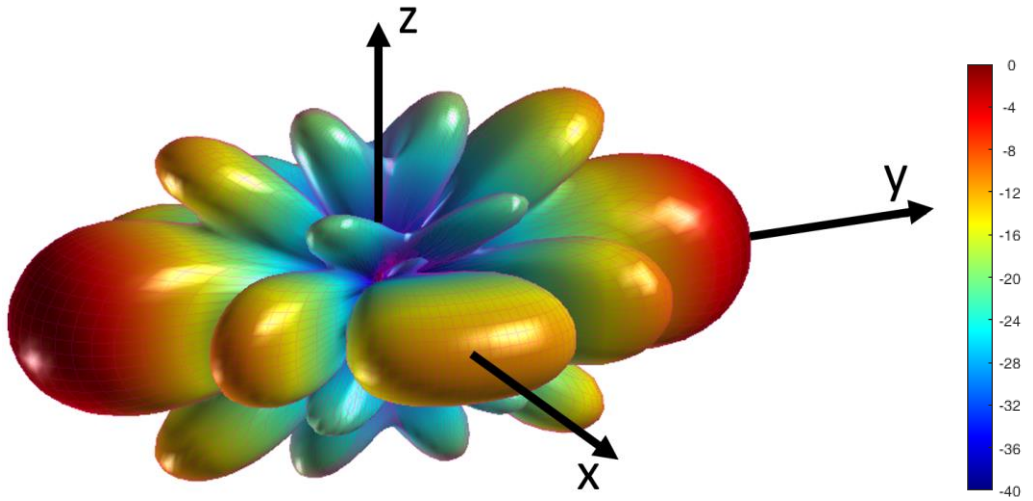

(c)

Fig.4.5-2 : 3D plots of (a) $\left|\bar{E}\{\bar{p}_m,\theta,\phi\}\right|$, **(b)** $\left|\bar{E}\{\bar{p}_e,\theta,\phi\}\right|$, **and (c)** $\left|\bar{E}\{\bar{p}_e,\theta,\phi\}+\bar{E}\{\bar{p}_m,\theta,\phi\}\right|$

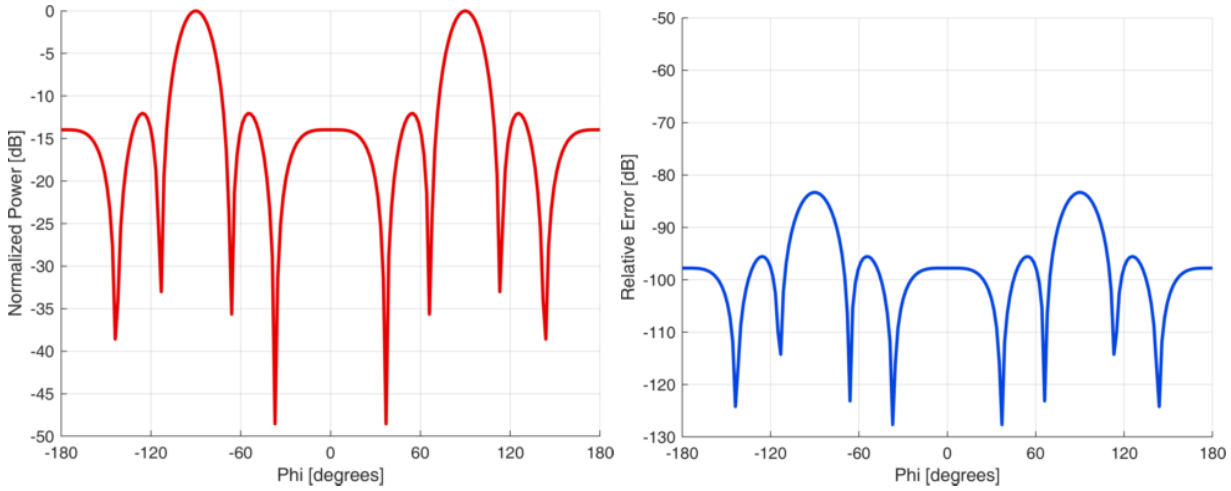

(a) **(b)**

Fig.4.5-3 : (a) $\left|\bar{E}\{\bar{p}_e,\theta,\phi\}+\bar{E}\{\bar{p}_m,\theta,\phi\}\right|$ **(red) and exact analytical** $\left|\bar{E}^{exact}\{AUT,\theta,\phi\}\right|$ **(black) far-zone patterns in the xy-plane. The exact (black) reference trace is completely covered by the calculated (red) trace; (b) Corresponding relative error between the curves (a).**

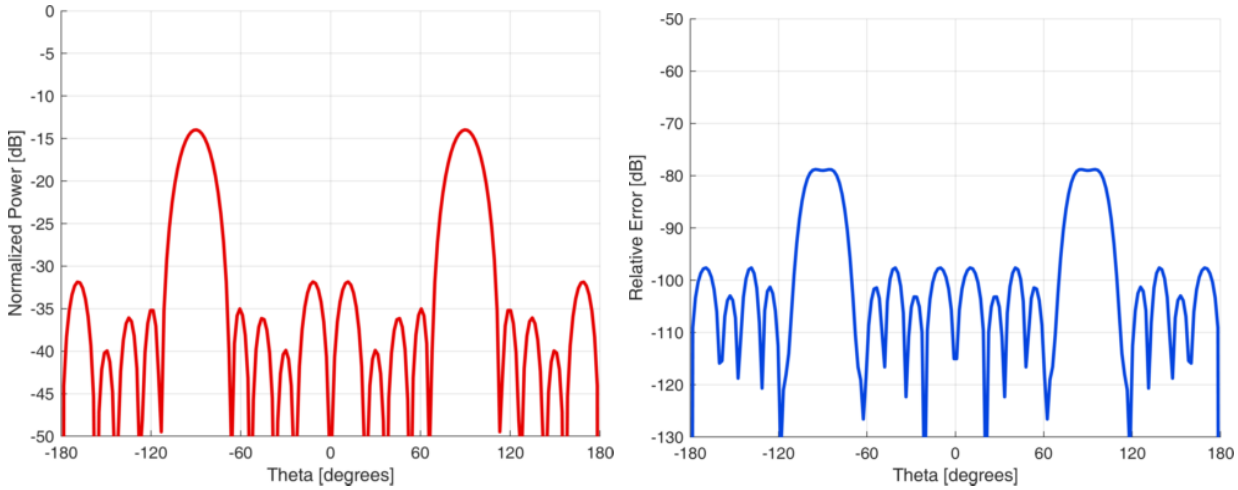

(a) **(b)**

Fig.4.5-4 : (a) $\left|\bar{E}\{\bar{p}_e,\theta,\phi\}+\bar{E}\{\bar{p}_m,\theta,\phi\}\right|$ **(red) and exact analytical** $\left|\bar{E}^{exact}\{AUT,\theta,\phi\}\right|$ **(black) far-zone patterns in the xz-plane. The exact (black) reference trace is completely covered by the calculated (red) trace; (b) Corresponding relative error between the curves in (a).**

4.6 TESTING OF THE SHROUD OF INFINITESIMAL ELECTRIC & MAGNETIC DIPOLES FOR 25-ELEMENT PLANAR ARRAY AUT – *NEAR-ZONE RESULTS*

4.6.1 Initial Remarks & Reminder of Notation

This test is similar to that in Section 4.5, except that the various fields are observed on a spherical surface S_{ref} slightly exterior to S_{meas}, defined as follows : Translate each point on S_{meas} along the unit normal at that point by amount δ_{offset}, so that each $\bar{r}_p \rightarrow \bar{r}_p + \delta_{\text{offset}}\hat{n}$. This is illustrated in Fig.4.6-1. Thus surface S_{ref} is of the same shape as S_{meas} but with each point ballooned out slightly (along the normal to S_{meas} at each point) to obtain the surface beyond S_{meas}. Both S_{meas} and S_{ref} are in the near-zone of the AUT. We will use $\delta_{\text{offset}} = 0.25\lambda$, because this takes us beyond the range of significant error, so that the radius $R_{ref} = R_{meas} + \delta_{\text{offset}} = 3.25\lambda$. The reason for using surface S_{ref} instead of S_{meas} will be given in Section 4.6.2.

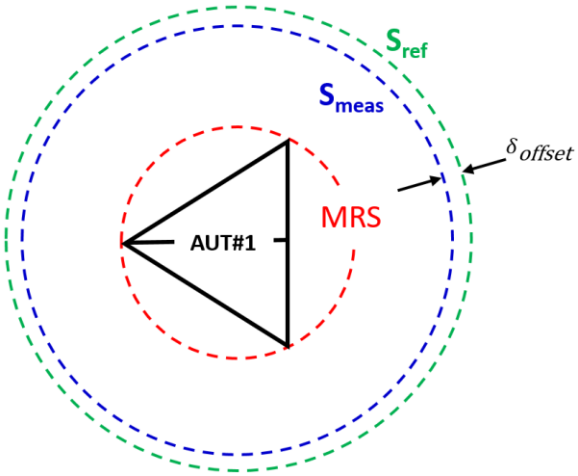

Fig.4.6-1 : Spherical Surfaces Surrounding AUT

We remind ourselves of the following notation/terminology:

- The fields of the AUT computed analytically at sample points on the measurement surface S_{meas} are $\bar{E}^{NF}\{AUT, S_{meas}\}$ and $\bar{H}^{NF}\{AUT, S_{meas}\}$. We recall that these are exact. The

fields of the AUT computed analytically at sample points on the surface S_{ref} will be denoted $\bar{E}^{NF}\{AUT, S_{ref}\}$ and $\bar{H}^{NF}\{AUT, S_{ref}\}$, and are also exact.

- Equivalent infinitesimal magnetic and electric dipole sets are found at the sample points on S_{meas} using $\hat{n}\times\bar{E}^{NF}\{AUT, S_{meas}\}$ and $\hat{n}\times\bar{H}^{NF}\{AUT, S_{meas}\}$, respectively, as before. These are the respective dipole shrouds on S_{meas}. This is precisely what was done in Section 4.5, and is merely re-stated here for convenience.

- The fields on S_{ref} due to ***only*** the equivalent electric dipole shroud are now computed and denoted by $\bar{E}\{\bar{p}_e, S_{\text{ref}}\}$ and $\bar{H}\{\bar{p}_e, S_{\text{ref}}\}$. Similarly, the fields on S_{ref} due to ***only*** the equivalent magnetic dipole shroud are computed and denoted by $\bar{E}\{\bar{p}_m, S_{\text{ref}}\}$ and $\bar{H}\{\bar{p}_m, S_{\text{ref}}\}$.

4.6.2 Observation of the Fields on S_{meas} and S_{ref} due to the Dipole Shrouds on S_{meas}

Fig.4.6-2(a) shows the exact $\left|\bar{E}^{NF}\{AUT, \bar{r}\}\right|$ depicted in the yz-plane, in the vicinity of the AUT. Fig.4.6-2(b) shows, in the same region, the field $\left|\bar{E}\{\bar{p}_e, \bar{r}\}+\bar{E}\{\bar{p}_m, \bar{r}\}\right|$, with the equivalent infinitesimal dipole shroud draped on S_{meas}. Visual checking, and in fact more detailed examination that will be shown below, shows[58] that the two quantities are almost the same at surface S_{ref} when $\delta_{\text{offset}} = 0.25\lambda$. Fig.4.6-2(c) shows the relative error term between the two quantities; we have zoomed in to the region close to S_{meas} and S_{ref}. This error is indeed extremely small on S_{ref}, but has peaks on S_{meas} at the locations of the dipoles (where we know the fields in fact are infinite. We will therefore compare the near-fields $\left|\bar{E}^{NF}\{AUT, S_{ref}\}\right|$ **and** $\left|\bar{E}\{\bar{p}_e, S_{\text{ref}}\}+\bar{E}\{\bar{p}_m, S_{\text{ref}}\}\right|$ on S_{ref}, and then in Section 5.2 discuss how $\left|\bar{E}\{\bar{p}_m, S_{\text{ref}}\}\right|$ will be used in the NF-to-FF transformation instead of $\left|\bar{E}\{\bar{p}_m, S_{\text{meas}}\}\right|$.

4.6.3 Numerical Test Results

According to the surface equivalence theorem we should find that

[58] Note that internal to S_{meas} the field $\left|\bar{E}\{\bar{p}_e, \bar{r}\}+\bar{E}\{\bar{p}_m, \bar{r}\}\right|$ is zero, precisely as expected from the surface equivalence theorem.

$$\bar{E}^{NF}\{AUT, S_{ref}\} = \bar{E}\{\bar{p}_e, S_{\text{ref}}\} + \bar{E}\{\bar{p}_m, S_{\text{ref}}\} \tag{4.6-1}$$

and

$$\bar{H}^{NF}\{AUT, S_{ref}\} = \bar{H}\{\bar{p}_e, S_{\text{ref}}\} + \bar{H}\{\bar{p}_m, S_{\text{ref}}\} \tag{4.6-2}$$

if the equivalent shroud of infinitesimal dipoles concept is valid. Fig.4.6-3 shows, in much the same format[59] as for Fig.4.5-2, that this is true, as can be seen by comparison to Fig.E-3. Since it is not customary to depict fields on a (near-field) surface in terms of lobes, their "heat-map" depiction on the surface S_{ref} is included alongside. The agreement, on S_{ref}, between the two field quantities is shown in Fig.4.6-4 and Fig.4.6-5 via plots of the fields along circles on S_{ref} in two different planes. The relative error is seen to be below -55dB. It is necessary to compare both the electric and magnetic fields because, in the near-zone, they are of course not as simply related as in the far-zone. Similar outcomes as those above for the electric field are found for the magnetic field.

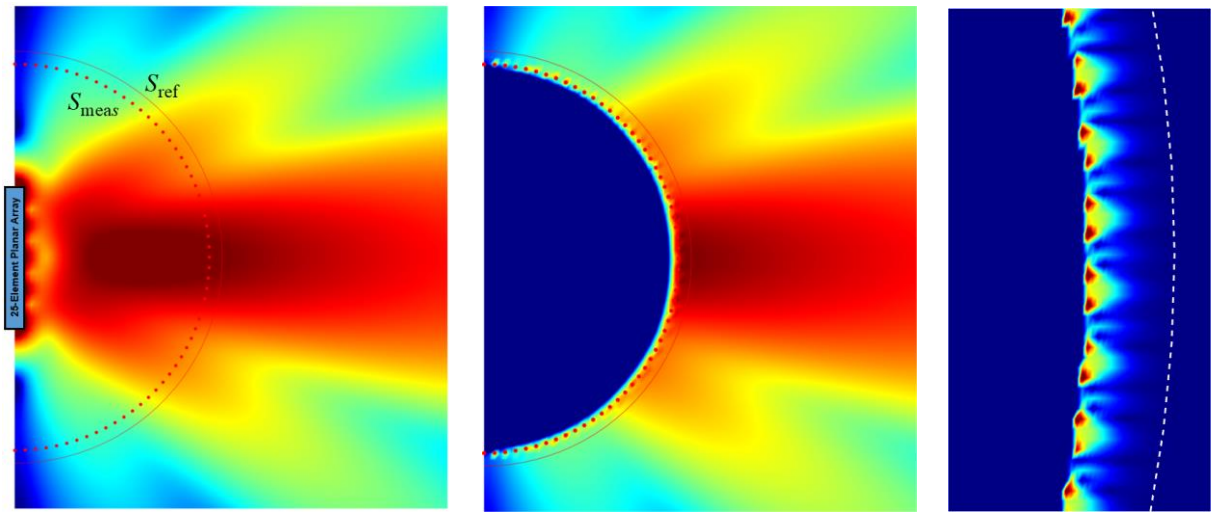

(a) **(b)** **(c)**

Fig.4.6-2 : (a) Exact analytically computed near-field fields of the AUT; (b) those computed from the equivalent shrouds of magnetic and electric dipoles; (c) close-up of the relative error term between (a) and (b) to show the peakedness directly on S_{meas} (and the white dashed line now representing S_{ref} for clarity).

[59] Although in Fig.4.5-2 they were far-zone fields, and thus on an infinite radius surface, where as here the fields are those on a finite radius spherical surface S_{ref}.

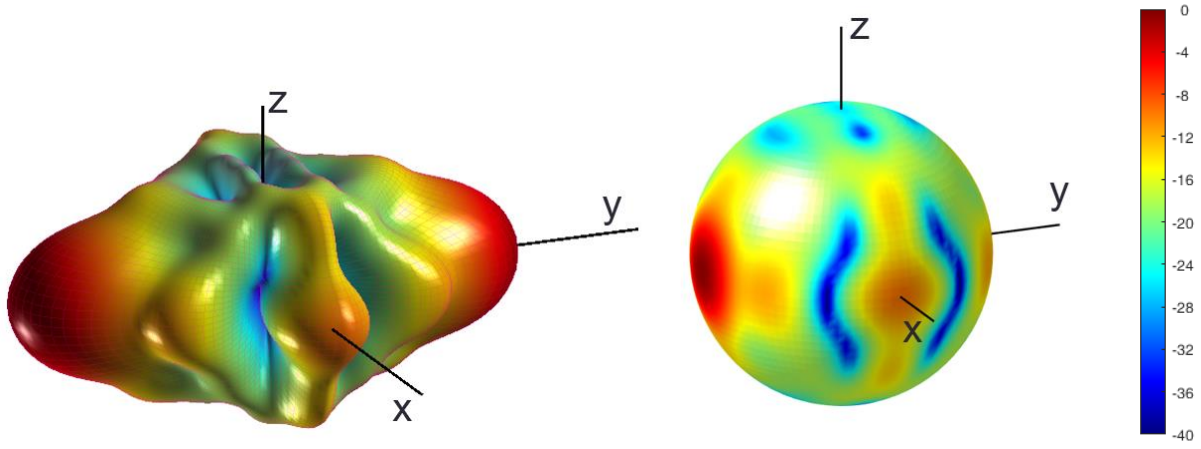

(a)

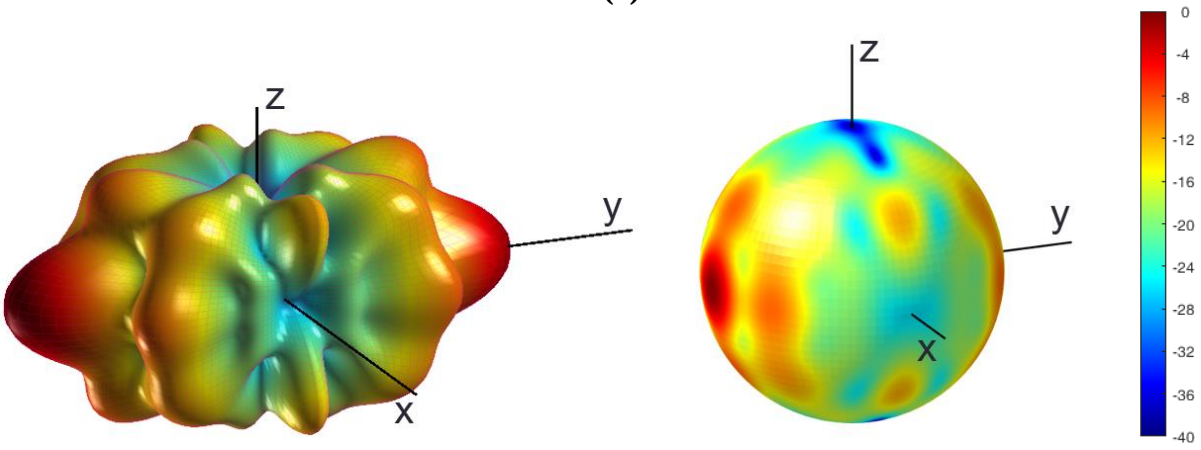

(b)

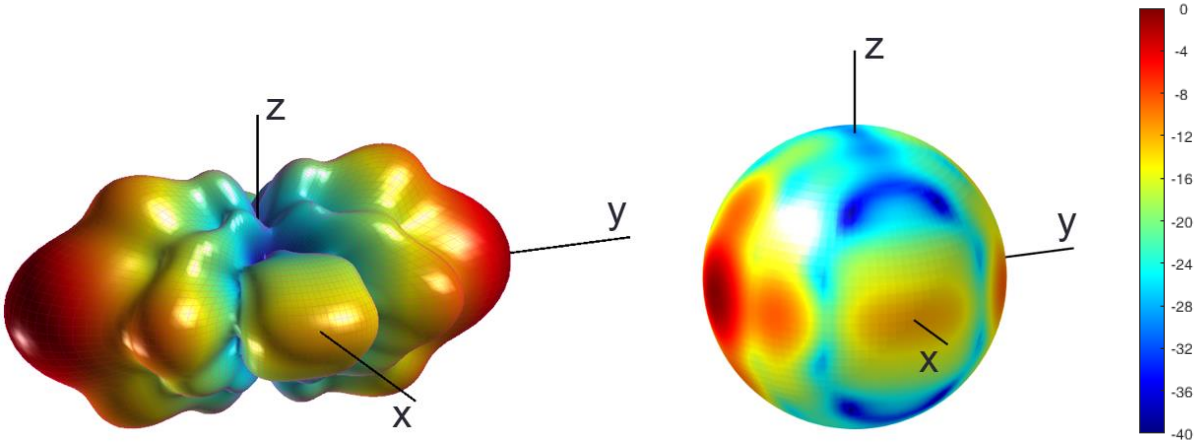

(c)

Fig.4.6-3 : 3D plots of (a) $\left|\bar{E}\{\bar{p}_m, S_{\text{ref}}\}\right|$**, (b)** $\left|\bar{E}\{\bar{p}_e, S_{\text{ref}}\}\right|$**, and (c)** $\left|\bar{E}\{\bar{p}_e, S_{\text{ref}}\} + \bar{E}\{\bar{p}_m, S_{\text{ref}}\}\right|$

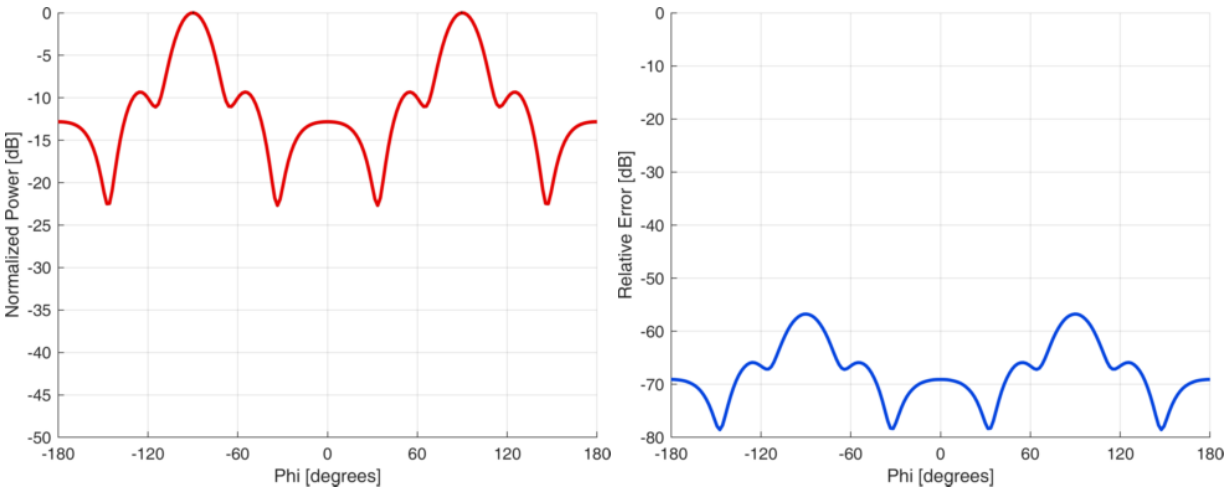

(a) **(b)**

Fig.4.6-4 : (a) $\left|\bar{E}\{\bar{p}_e, S_{\text{ref}}\} + \bar{E}\{\bar{p}_m, S_{\text{ref}}\}\right|$ **(red) and exact analytical** $\left|\bar{E}^{exact}\{AUT, S_{\text{ref}}\}\right|$ **(black) plot in the xy-plane along a circle of radius** $R_{ref.}$ **The exact (black) reference trace is completely covered by the calculated (red) trace; (b) Corresponding relative error curve in the same plane.**

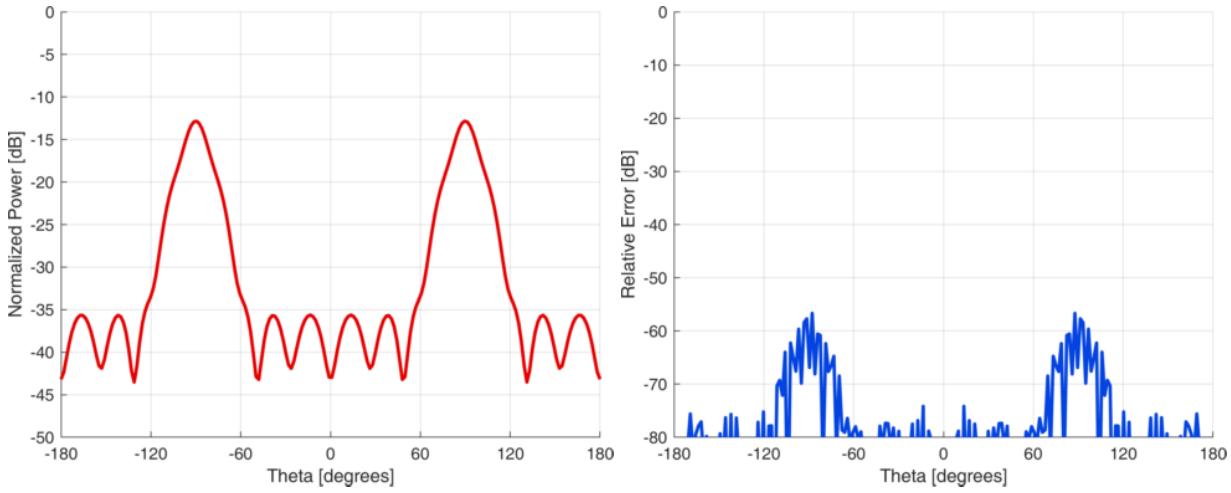

(a) **(b)**

Fig.4.6-5 : (a) $\left|\bar{E}\{\bar{p}_e, S_{\text{ref}}\} + \bar{E}\{\bar{p}_m, S_{\text{ref}}\}\right|$ **(red) and exact analytical** $\left|\bar{E}^{exact}\{AUT, S_{\text{ref}}\}\right|$ **(black) plot in the xz-plane along a circle of radius** R_{ref}**. The exact (black) reference trace is completely covered by the calculated (red) trace; (b) Corresponding relative error curve in the same plane.**

4.6.4 Influence of the Sample Point Density (on the Measurement Surface)

The comparisons between $\left|\bar{E}^{NF}\{AUT, S_{ref}\}\right|$ and $\left|\bar{E}\{\bar{p}_e, S_{\text{ref}}\}+\bar{E}\{\bar{p}_m, S_{\text{ref}}\}\right|$ in Section 4.6.2 were for the case $P/Q=3$, which is case (c) in Fig.4.6-6. Fig.4.6-7 reveals that $P/Q=2$ is sufficient to have a relative error below -40dB, and so on[60].

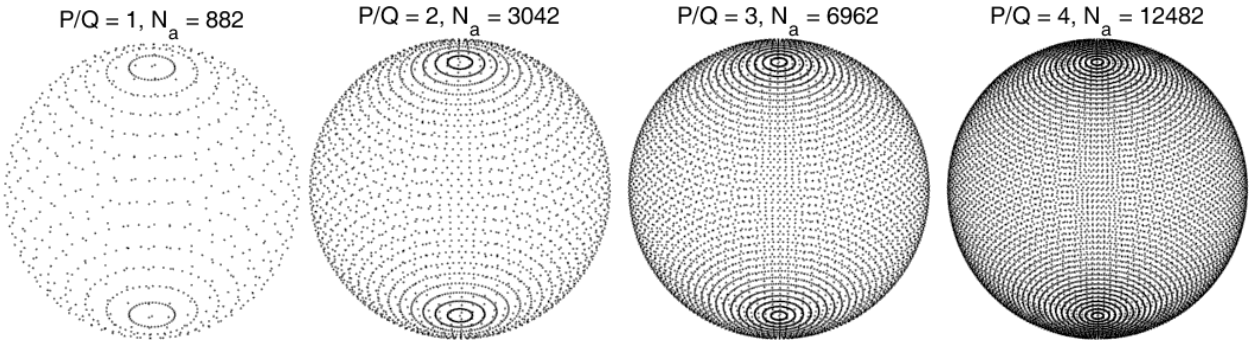

(a) **(b)** **(c)** **(d)**

Fig.4.6-6 : Depiction of set of sample points $\{\bar{r}_p, p=1,2,....,P\}$ for various values of *P/Q* on a spherical surface.

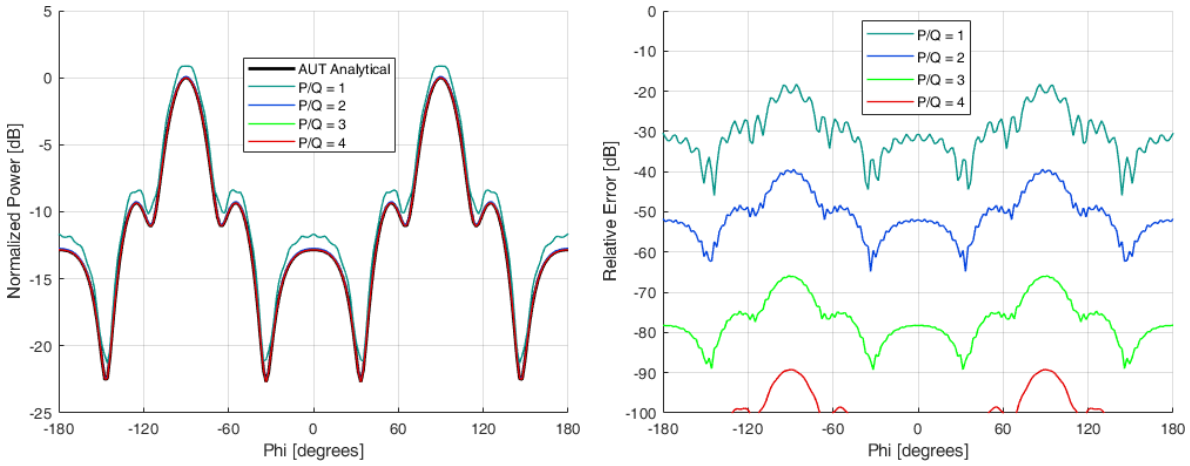

(a) **(b)**

Fig.4.6-7 : (a). $\left|\bar{E}\{\bar{p}_e, S_{\text{ref}}\}+\bar{E}\{\bar{p}_m, S_{\text{ref}}\}\right|$ (red) and exact analytical $\left|\bar{E}^{exact}\{AUT, S_{\text{ref}}\}\right|$ (black) plot in the xy-plane along a circle of radius R_{ref} for various values of *P/Q* and (b) the corresponding relative error curve in the same plane.

[60] The curves are normalised to the maximum value of the exact result.

4.7 CONCLUSIONS

Formulations for the moment method solution of the EFIE, MFIE and CFIE to model scattering from a perfectly conducting body-of-revolution have been implemented in computer code. This considerable task was necessary because such a code is not available commercially or elsewhere. Thus it has in its own right made available a computational tool that might be useful in areas of electromagnetic engineering other than that of interest in this thesis. Section 4.2 mentioned that the numerical analysis used in its implementation largely followed the approaches recommended in the original references for the IE formulations, but described some changes that were brought about for reasons of computational efficiency. The code was validated using benchmark tests in Section 4.3.

In Section 4.5 sampled equivalent infinitesimal electric ($\bar{p}_e$) and magnetic ($\bar{p}_m$) dipole sets were shown to successfully represent the surface equivalent currents $\bar{J}_s$ and $\bar{M}_s$ on S_{meas}, as regards the far-zone fields. The conclusion is that $\bar{E}\{\bar{p}_m, \theta, \phi\}$ can indeed represent $(\bar{E}^{inc}, \bar{H}^{inc})$ due to $\bar{M}_s^{NF}$ almost identically in the far-zone, as part of the proposed NF-to-FF transformation. Similar tests were run in Section 4.6, in which it was seen that the equivalent magnetic dipole set on S_{meas} cannot precisely provide $\bar{E}^{inc}(S_{meas})$ and $\bar{H}^{inc}(S_{meas})$ due to $\bar{M}_s^{NF}$ at observation points on S_{meas} itself. The fields are infinite at the locations $\bar{r}_p$ of each dipole. This was expected, as the expressions for the fields of individual dipoles in Appendix B and Appendix C clearly show. However, it was shown that these "hot-spots" are weakened if we observe $\bar{E}^{inc}(S_{ref})$ and $\bar{H}^{inc}(S_{ref})$ at points on a surface S_{ref} of the same shape as S_{meas} but slightly ballooned-out from it. The decision was taken to assume that the PEC-BOR used in the proposed NF-to-FF transformation will be assumed to be S_{ref} instead of S_{meas}, even though the AUT data would have been acquired on S_{meas}. This approximation will be used, encouraged by the additional fact that the incident fields so calculated lie within an integration operation[61] when the MM excitation vectors are evaluated, thus undergoing some additional 'smoothing'. In the next chapter the NF-to-FF transformation will be applied in full.

[61] This can be seen in expressions (2.4-16) and (2.4-17) for the MFIE case, and (2.4-31) and (2.4-32) for the EFIE case.

CHAPTER 5

Validation of the CEM-Based Near-Field to Far-Field Transformation

5.1 INTRODUCTION

In Chapter 3 a new NF-to-FF transformation was proposed in order to be able to perform antenna near-field testing using any rotationally symmetric measurement surface S_{meas} instead of only a spherical one. This requires that the acquired tangential electric field data on S_{meas} be considered to be (converted to) a shroud of impressed magnetic surface current density, and its field be computed and used as the field incident on a PEC surface identical to S_{meas}. An IE/MM formulation uses these incident fields as excitation, and solves for the surface electric current density $\bar{J}_{\text{pec}}$ on the PEC surface. This current density provides the far-zone **scattered field** in the MM model, namely $\bar{E}^{scat}\{\bar{J}_{\text{pec}}, \theta, \phi\}$, which when added to the far-zone field of the above impressed magnetic current density gives the desired far-zone radiation pattern of the AUT. The components for the implementation of the NF-to-FF transformation were discussed and validated in Chapter 4. In the present chapter this NF-to-FF transformation implementation will be applied to the AUT described in Appendix E and used in Chapter 4.

5.2 APPLICATION OF THE NF-TO-FF TRANSFORMATION FOR 25-ELEMENT ARRAY AUT : SPHERICAL S_{meas} AND S_{ref}

The surfaces S_{meas} and S_{ref} are as specified in Section 4.6.1. The need to use S_{ref}, instead of S_{meas} directly, has already been explained in Sections 4.6 and Section 4.7, and applies to all geometries, including the present spherical case. It has been noted in [MAUT 77] that any positive value of α can be used in the CFIE (2.3-18). In this work we used $\alpha = 0$ because for the problems considered, no internal resonance problems were encountered. We may therefore go directly to a summary of the outcome $\left|\bar{E}\{AUT, \theta, \phi\}\right|$ of the implemented NF-to-FF transformation. Fig.5.2-1 compares this to $\left|\bar{E}^{exact}\{AUT, \theta, \phi\}\right|$ in the xy-plane[62], and Fig.5.2-2 in

[62] The orientation of these planes with respect to the AUT can be seen from Fig.E-1.

the yz-plane. The largest errors occur in the direction of the pattern dips, where it is under -20dB. In the direction of the main lobes the error is below about -30dB.

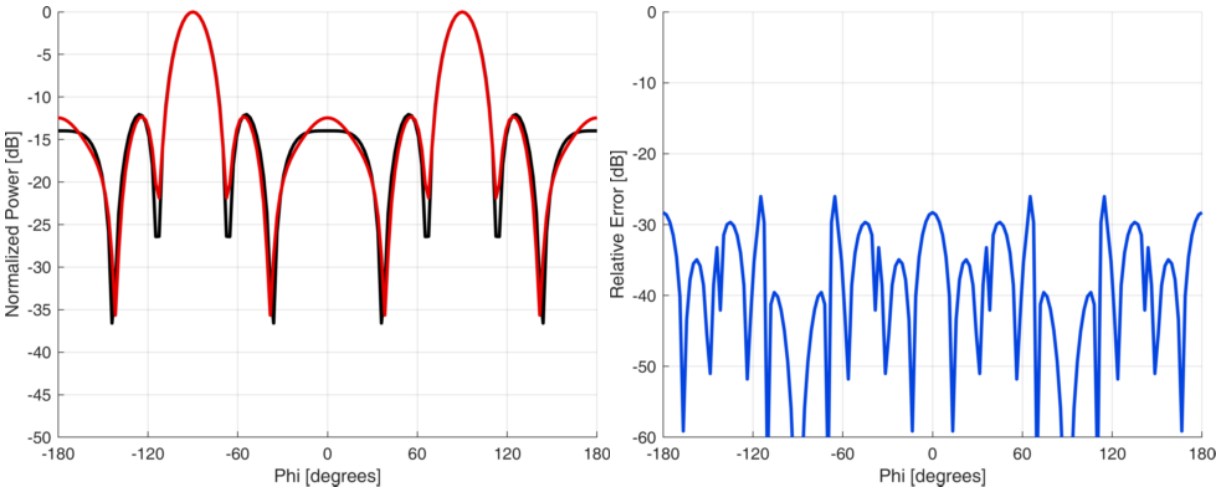

(a) **(b)**

Fig. 5.2-1 : (a) Computed $\bar{E}\{AUT,\theta,\phi\}$ (red,) & reference $\bar{E}^{exact}\{AUT,\theta,\phi\}$ (black,) total electric far-zone field magnitude for a cut in the XY-plane through the primary-lobes. (b) Corresponding relative error (blue) between the computed and reference electric far-field magnitudes. Ratio $P/Q=4$.

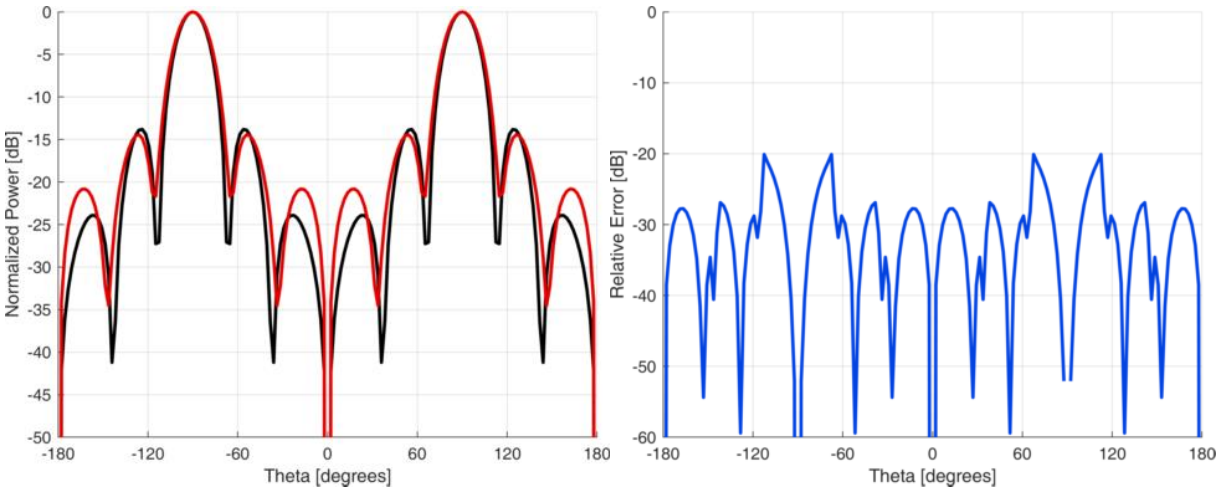

(a) **(b)**

Fig. 5.2-2 : (a) Computed $\bar{E}\{AUT,\theta,\phi\}$ (red,) and reference $\bar{E}^{exact}\{AUT,\theta,\phi\}$ (black,) total electric far-zone field magnitude for a cut in the YZ-plane. (b) Corresponding relative error (blue) between the computed and reference electric far-zone field magnitudes. Ratio $P/Q=4$.

5.3 APPLICATION OF THE NF-TO-FF TRANSFORMATION FOR 25-ELEMENT ARRAY AUT : PROLATE SPHEROIDAL S_{meas} AND S_{ref}

The same AUT was used with surfaces S_{meas} and S_{ref} now prolate spheroids, as shown in Fig.5.3-1. The sampling density for the prolate spheroid, both in $\Delta\theta$ and $\Delta\phi$, are the same as for the spherical case previously considered. The outcome $\left|\bar{E}\left\{AUT,\theta,\phi\right\}\right|$ of the implemented NF-to-FF transformation for this case is shown in Fig.5.3-3 in the yz-plane. In this case the largest errors (around -20dB) occur in the direction of the pattern dips and also the first sidelobe directions. We have also found that the $\left|\bar{E}\left\{AUT,\theta,\phi\right\}\right|$ obtained is sensitive to the value chosen for[63] δ_{offset}.

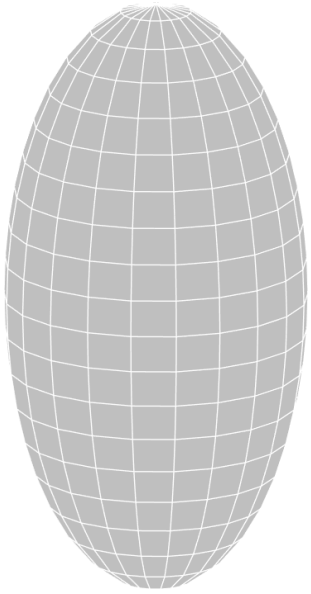

Fig. 5.3-1 : Illustration of S_{meas} surface for prolate spheroid case. The spheroid has a minor (horizontal) axis radius of 3λ and a major axis radius of 6λ. The surface S_{ref} is coincident with corresponding radii of 3.25λ & 6.25λ respectively. Ratio $P/Q=4$.

[63] Recall that δ_{offset} was defined in Section 4.6.1.

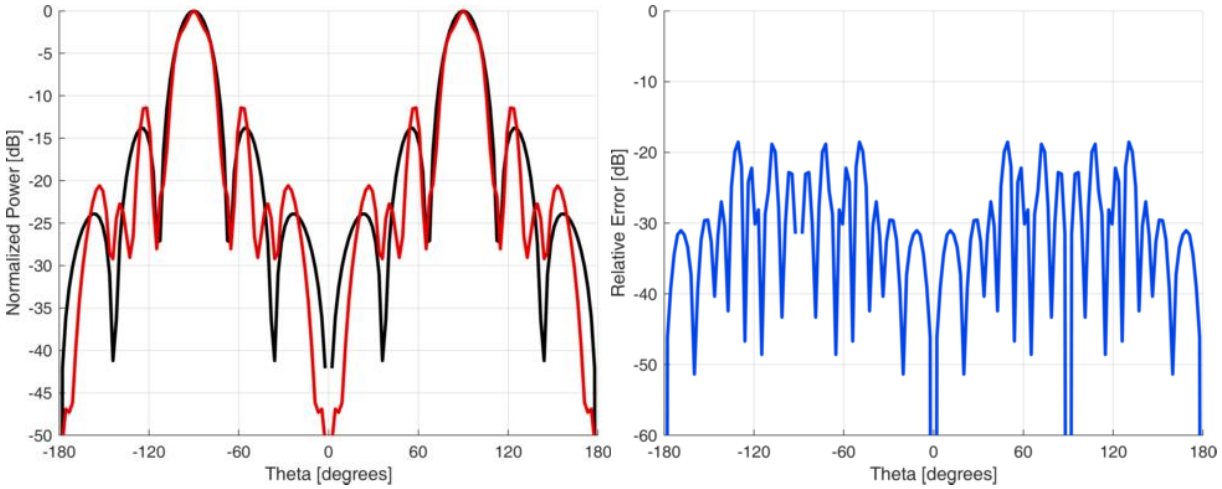

(a) **(b)**

Fig. 5.3-2 : (a) Computed $\bar{E}\{AUT,\theta,\phi\}$ (red,) and reference $\bar{E}^{exact}\{AUT,\theta,\phi\}$ (black,) total electric far-zone field magnitude for a cut in the YZ-plane through the primary lobes. (b) Corresponding relative error (blue) between the computed and reference electric far-zone field magnitudes.

After the thesis defense we ran and oblate spheroid case. The results are no more accurate than the prolate spheroid case, and so these will not be shown. The thesis has made the point that an S_{ref} (eg. a ballooned S_{meas}) is needed because the incident fields, $\bar{E}^{inc}$ and $\bar{H}^{inc}$, were to be computed rapidly and this has been shown to be less than acceptable for elongated measurement surfaces S_{meas}. A more precise (and rapid) approach thus needs to be sought for computing these incident fields. Showing oblate spheroid results will not alter this conclusion.

5.4 CONCLUDING REMARKS

The implementation, developed in Chapter 4, of the proposed NF-to-FF transformation has been applied and validated in the present chapter for a 25-elemenrt planar array AUT. Sensitivity of the outcome $\bar{E}\{AUT,\theta,\phi\}$ to the choice of the value of δ_{offset} points to the use of the equivalent set of infinitesimal magnetic dipoles as an approximation for the actual shroud $\bar{M}_s^{NF}$ on the measurement surface[64], and the attendant inaccuracy due to use of the dipoles in the near field, as the causes of the reduced (an error below -20dB is desired) accuracy. Possible improvements connected to this aspect of the implementation of the NF-to-FF transformation are suggested in Chapter 6. It is not the NF-to-FF transformation idea that is in error, or the implementation of the IE/MM code *NFBOR* that has been separately validated in Section 4.3.

[64] For the purposes of finding the field due to $\bar{M}_s^{NF}$ on S_{meas} itself. The use of the set of infinitesimal dipoles approximation to find the field due to $\bar{M}_s^{NF}$ in the far-zone was found in Section 4.5 to be sound.

CHAPTER 6
General Conclusions

6.1 CONTRIBUTIONS

Chapter 3 proposed an approach for a new CEM-based NF-to-FF transformation that allows the near-field to be acquired on any rotationally symmetric 'body of revolution' (BOR) measurement surface S_{meas}, and not only a spherical one. The acquired tangential electric field of the antenna under test (AUT) on the BOR measurement surface S_{meas} is converted into a shroud of magnetic current density $\bar{M}_s^{NF}\{S_{meas}\}$ on S_{meas}, and the fields $\bar{E}^{inc}\{\bar{M}_s^{NF}, S_{meas}\}$ and $\bar{H}^{inc}\{\bar{M}_s^{NF}, S_{meas}\}$ of this shroud determined. The latter fields form the incident fields on a PEC surface identical to S_{meas}, and a MM formulation is used to compute the resulting induced electric surface current density $\bar{J}_{pec}$ on the BOR. The far-zone field $\bar{E}^{scat}\{\bar{J}_{pec}, \theta, \phi\}$ due to this induced current density, when added to the far-zone field $\bar{E}^{inc}\{\bar{M}_s^{NF}, \theta, \phi\}$ due to $\bar{M}_s^{NF}\{S_{meas}\}$, gives the far-zone radiation pattern $\bar{E}\{AUT, \theta, \phi\} = \bar{E}^{inc}\{\bar{M}_s^{NF}, \theta, \phi\} + \bar{E}^{scat}\{\bar{J}_{pec}, \theta, \phi\}$ of the AUT. The whole process constitutes the NF-to-FF transformation.

Chapter 4 described the numerical implementation of the tools needed to implement this idea in a computationally efficient manner. This consisted of a MM code (NFBOR) that implements the EFIE, MFIE or CFIE for scattering from the PEC surface, and customized to exploit the BOR nature of the surface geometry S_{meas}. Benchmark problems were used to demonstrate the correctness of the MM implementation. A numerically efficient means of finding the incident fields the fields $\bar{E}^{inc}\{\bar{M}_s^{NF}, S_{meas}\}$ and $\bar{H}^{inc}\{\bar{M}_s^{NF}, S_{meas}\}$ due to the shroud of magnetic current density mentioned above was developed. It approximates $\bar{M}_s^{NF}$ by a set of infinitesimal magnetic dipoles on S_{meas}. The far-zone fields of the set of infinitesimal dipoles $\bar{E}^{inc}\{\bar{p}_m, \theta, \phi\}$ was shown to be almost identical to $\bar{E}^{inc}\{\bar{M}_s^{NF}, \theta, \phi\}$, and can be computed very rapidly. However, due to the fact that $\bar{E}^{inc}\{\bar{p}_m, S_{meas}\}$ and $\bar{H}^{inc}\{\bar{p}_m, S_{meas}\}$ have singularities at the locations of

the individual infinitesimal dipoles, it is necessary to compute these at points slightly offset from S_{meas}, on a surface which we called S_{ref}, and assume that the PEC surface was actually S_{ref} and not the true S_{meas} on which the AUT near-fields would have been acquired. Nevertheless, the validity of the proposed new NF-to-FF transformation was demonstrated in principle in Chapter 5.

6.2 PROBLEM ISSUES & POSSIBLE FUTURE WORK

The new proposed NF-to-FF transformation, and the implementation of the IE/MM analysis to implement it, is sound. However, the approximation of $\bar{E}^{inc}\{\bar{M}_s^{NF}, S_{meas}\}$ and $\bar{H}^{inc}\{\bar{M}_s^{NF}, S_{meas}\}$ by $\bar{E}^{inc}\{\bar{p}_m, S_{meas}\}$ and $\bar{H}^{inc}\{\bar{p}_m, S_{meas}\}$, respectively, results in inaccuracies in the predicted far-zone patterns of the AUT. The fields of $\bar{E}^{inc}\{\bar{M}_s^{NF}, S_{meas}\}$ and $\bar{H}^{inc}\{\bar{M}_s^{NF}, S_{meas}\}$ would be smooth functions, since $\bar{M}_s^{NF}$ is a smooth function. Even though[65] incident fields lie within an integration operation when the MM excitation vectors are evaluated, thus undergoing some additional 'smoothing', the non-physical singularities in by $\bar{E}^{inc}\{\bar{p}_m, S_{meas}\}$ and $\bar{H}^{inc}\{\bar{p}_m, S_{meas}\}$ at each infinitesimal dipole location result in inaccurate evaluation of the MM excitation vectors. By approximating S_{meas} by S_{ref} the singularity issue is removed, but now the problem being solved to find $\bar{E}^{scat}\{\bar{J}_{pec}, \theta, \phi\}$ is too unlike the actual problem we wish to solve for correct execution of the NF-to-FF transformation to be sufficiently accurate.

Several recommendations can be made for future work. *Firstly*, instead of approximating $\bar{M}_s^{NF}$ by infinitesimal dipoles, it can be represented by a linear or higher-order function over each of the quadrilateral-like regions described in Section 4.4.3, weighted by the acquired tangential electric field at the centroid of the region. The resulting incident fields on S_{meas} will then not have unphysical singularities. The incident fields on S_{meas} would need to be obtained by numerical integration over each quadrilateral-like region, something we said in Section 4.4.2 we wished to avoid. With hindsight, we note that these incident fields on S_{meas} could be

[65] As optimistically hoped in Section 4.7.

obtained for just one set of quadrilateral-like regions along a line-of-longitude, for unity weight $\bar{M}_s^{NF}$ on each such region, and stored. These would not change for a given S_{meas} and frequency. The fields due to similar regions that are located at other locations in azimuth on the BOR could be obtained by simply altering the value of the azimuth angle, and applying the weight appropriate to that particular quadrilateral like region. *Secondly*, it has come to our attention, that even if $\bar{M}_s^{NF}$ and its fields on S_{meas} are found correctly, there may still be issues in computing the excitation vectors of the MM, which arises whenever (as in the present case) the source distribution is on the same surface on which we wish to know its fields. In such cases a procedure that has been given the name of the pseudo-image approach (to find the excitation vectors) could be used [YUAN 87]. It has not been used in the BOR context, and appears to be not well known. However, if a sufficiently large number (N_t) of expansion functions can be used along the generatrix of the BOR, we believe that use of the pseudo-image will not be necessary. Thirdly, probe correction could possibly included as part of the excitation vector evaluation process, although with the way the probe would be used to acquire data (always normal to the close rotationally symmetric S_{meas}) this may also not be needed [PARI 14].

References

[ABRA 64] M.Abramowitz and I.A.Stegun, *Handbook of Mathematical Functions* (US Government Printing Office, 1964).

[ALMA 19] E.Almajali, D.J.Janse van Rensburg and D.A.Mcnamara, “Customized spherical near-field test time reduction for wireless base station antennas”, *IEEE Antennas Wireless Propagat. Letters*, Vol.18, No.1, pp.172-176, Jan.2019.

[BEAU 13] V.Beaulé, D.A.McNamara, D.J.Janse van Rensburg and L.Shafai, "Exploration of the feasibility of adaptive spherical near-field antenna measurements", *35th Annual AMTA Symp.*, Oct.2013, USA.

[BUCCI 87] O.M.Bucci and G.Franseschetti, “On the spatial bandwidth of scattered fields”, *IEEE Trans. Antennas Propagation*, Vol.35, pp.1445-1455, 1987.

[BUCCI 88] O.M.Bucci and G. Di Massa, “The truncation error in the application of sampling series to electromagnetic problems”, *IEEE Trans. Antennas Propagation*, Vol.36, pp.941-949, 1988.

[BUCCI 89] O.M.Bucci and G.Franseschetti, “On the degrees of freedom of scattered fields”, *IEEE Trans. Antennas Propagation*, Vol.37, pp.918-926, 1989.

[CANO 11] F.J.Cano-Facila and S. Pivnenko, "A new method to reduce truncation errors in partial spherical near-field measurements", Proc. *5th European Conf. Antennas Propagat.*, pp. 3259-3263, Rome, Italy, 2011.

[CONN 01] P.D.T.O’Connor, Editorial, *IEEE Spectrum*, July 2001, pp.18

[DIRE 12] R.H. Direen & H.G. Direen, “Spherical near-field measurments: Going off grid”, *34th Annual AMTA Symp.*, Oct.2012, USA.

[FARO 16] F.Farouq, M.Serhir and D.Picard, “Antenna far-field assessment from near-field measured over arbitrary surfaces”, *IEEE Trans. Antennas Propagation*, Vol.64, No.12, pp.5122 - 5130, Dec. 2016.

[FEKO] *FEKO*, Altair Inc. (www.altair.com).

[GIBS 08] W.C.Gibson, *The Method of Moments in Electromagnetics* (Chapman & Hall, 2008).

[GLIS 80a] A.W.Glisson and D.R.Wilton, “Simple and efficient numerical methods for problems of electromagnetic radiation and scattering from surfaces”, IEEE Trans. Antennas Propagat., Vol.28, No.5, pp.593-603, Sept.1980.

[GLIS 80b] A.W.Glisson and C.M.Butler, “Analysis of a wire antenna in the presence of a body of revolution”, *IEEE Transactions on Antennas and Propagation*, vol. 28, no. 5, pp 604-609, Sept.1980.

[HANS 88] J.E.Hansen, *Spherical Near-field Antenna Measurements* (Peter Peregrinus Ltd, 1988).

[HARR 61] R.F.Harrington, *Time-Harmonic Electromagnetic Fields* (McGraw-Hill, 1961).

[HARR 68] R.F.Harrington, *Field Computation by Moment Methods* (McGraw-Hill, 1968).

[JANS 19] D.J.Janse van Rensburg, B.Walkenhorst, Q.Ton and J.Demas, "A robotic near-field antenna test system relying on non-canonical transformation techniques”, *41st Annual AMTA Symp.*, San Diego, USA, Oct.2019.

[KRIS 16] G.Kristensson, *Scattering of Electromagnetic Waves by Obstacles* (SciTech Publ., 2016)

[KUCH 20a] A.A.Kucharski, “Resonances in heterogeneous dielectric bodies with rotational symmetry – Volume integral-equation formulation”, IEEE Trans. Antennas Propagat., Vol.48, No.5, pp.766- 770, May 2000.

[KUCH 20b] A.A.Kucharski, “A method of moments solution for electromagnetic scattering by inhomogeneous dielectric bodies of revolution”, IEEE Trans. Antennas Propagat., Vol.48, No.8, pp.1202-1210, Aug.2000

[LI 12] P.Li and L.Jiang, “The far field transformation for the antenna modelling based on spherical electric field measurements”, *Progress Electromagnetics Research*, Vol.123, pp.243-261, 2012.

[LYON 11] R.G.Lyons, *Understanding Digital Signal Processing* (Prentice-Hall, 2011) 3rd Edition.

[MART 11] E.Martini, S.Maci and L.J.Foged, "Spherical near field measurements with truncated scan area", Proc. 5*th European Conf. Antennas Propagat.*, pp. 3256 - 3258, Rome, Italy, April 2011.

[MAUT 69] J.R.Mautz and R.F.Harrington, “Radiation and scattering from bodies of revolution”, Appl. Sci. Res., Vol.20, pp.405-435, June 1969.

[MAUT 77] J.R.Mautz and R.F.Harrington, *H-Field, E-Field, and Combined-Field Solutions for Bodies of Revolution*, Tech. Report RADC-TR-77-109, Department of Electrical Engineering, Syracuse University, New York, March 1977.

[MAUT 78] J.R.Mautz and R.F.Harrington, “H-field, E-field, and combined-field solutions for bodies of revolution”, AEÜ,Vol.32, No.4, pp.157-164, April 1978.

[McNA 16] D.A.McNamara, Course Notes for *ELG7100 : The Moment Method in Electromagnetics*, University of Ottawa, Fall 2016.

[MORI 90] N.Morita, N.Kumagai & J.R.Mautz, *Integral Equation Methods for Electromagnetics* (Artech House, 1990997).

[NIKO 18] P.Nikolaev, "Calculation of Euler angles", www.geom3d.com/data/documents (Accessed 2018).

[NSI] NSI2000 Software User Manual, NSI-MI Technologies (www.nsi-mi.com), USA.

[PARI 14] C.Parini, S.Gregson, J.McCormick & D.J.Janse van Rensburg, *Principles, Theory and Practice of Modern Antenna Range Measurements* (IET Electromagnetic Wave Series, 2014)

[PETE 97] A.Peterson, S.Ray and R.Mittra, *Computational Methods for Electromagnetics* (IEEE Press, 1997).

[POPO81] B.D.Popovic, "Electromagnetic field theorems", IEE Proc., Vol.128, Pt.A, No.1, pp.47-63, Jan.1981

[POZA12] D.M.Pozar, *Microwave Engineering* (Wiley, 2012).

[RAHM 79] Y.Rahmat-Samii, "Useful coordinate transformations for antenna applications", *IEEE Trans. Antennas Propagation*, Vol.27, No.4, pp.571-574, July 1979.

[SCHW 59] M.Schwartz, *Information, Transmission, Modulation, and Noise* (McGraw-Hill, 1959).

[VAES 12] J.A.H.M. Vaessen, M.C. van Beurden A.G. Tijhuis, "Accurate and efficient computation of the modal green's function arising in the electric-field integral equation for a body of revolution", *IEEE Trans. Antennas Propagation*, Vol.60, No.7, 3294-3304, July 2012.

[VOLA 07] J.L.Volakis (Edit.), *Antenna Engineering Handbook* (McGraw-Hill, 2007)

[VOLA 12] J.L.Volakis and K.Sertel, *Integral Equation Methods for Electromagnetics* (SciTech Publ., 2012).

[WALK 97] S.S.Walklin, "Multilevel signaling for increasing the capacity of high-speed optical communication systems", PhD Thesis, University of Alberta, Canada, 1997.

[WEEK 68] W.L.Weeks, *Antenna Engineering* (McGraw-Hill, 1968).

[YAGH 81] A.D.Yaghjian, "Augmented electric- and magnetic-field integral equations", *Radio Science*, Vol.16, No.6, pp.987-1001, Nov.-Dec. 1981.

[YUAN 87] X.Yuan, R.F. Harrington and J.R.Mautz, "The pseudo-image method for computing the electromagnetic field that penetrates into a cavity", *Archiv für Elektronik und Übertragungstechnik* (AEÜ), Vol.41, No.5, pp.307-317, May 1987.

APPENDIX A

Basic Notation for Electromagnetic Fields

Any electromagnetic field, and hence the electromagnetic field of *any* antenna can be written (with respect to the chosen coordinate origin) as

$$\bar{E}(r,\theta,\phi) = E_\theta(r,\theta,\phi)\,\hat{\theta} + E_\phi(r,\theta,\phi)\,\hat{\phi} + E_r(r,\theta,\phi)\,\hat{r} \qquad \text{(A-1)}$$

and

$$\bar{H}(r,\theta,\phi) = H_\theta(r,\theta,\phi)\,\hat{\theta} + H_\phi(r,\theta,\phi)\,\hat{\phi} + H_r(r,\theta,\phi)\,\hat{r} \qquad \text{(A-2)}$$

where (r,θ,ϕ) specifies an observation point in the three-dimensional space surrounding the antenna. A useful viewpoint is to think of a sphere of radius r surrounding the antenna, with observation point (r,θ,ϕ) a point on this sphere. The pair (θ,ϕ) gives the direction of the observation point and r its distance from the origin of the coordinate system. The first two components in each of the above expressions are the *transverse* components of the antenna's electromagnetic field. Quantities $E_r(r,\theta,\phi)$ and $H_r(r,\theta,\phi)$, are the *radial* components of the electromagnetic field. The magnetic field $\bar{H}(r,\theta,\phi)$ can be found from $\bar{E}(r,\theta,\phi)$ using Maxwell's equations, and vice versa.

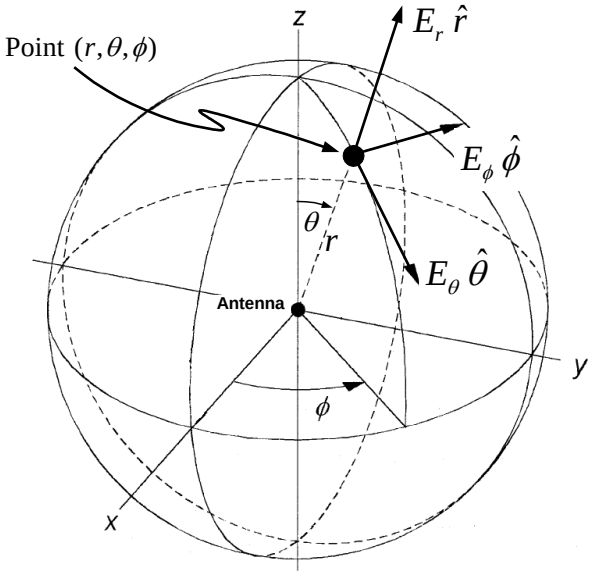

Fig.A-1 : Spherical coordinate system and vector components.

The physical space around an antenna is considered to consist of three different regions : the reactive near-zone region, the radiating near-zone region (also called the Fresnel region), and the radiating far-zone region (also called the Fraunhofer region). The boundaries of these regions cannot be precisely delineated, but the general properties of the electromagnetic fields in each zone can be established. The reactive near-zone is defined as that region of the field immediately surrounding the antenna wherein the reactive near field dominates. If we consider the "centre of mass" of the antenna to be located at the coordinate origin, then r can be considered to be a measure of distance from the antenna. In the reactive near zone the reactive fields predominate and fall off at rates $1/r^2$ or $1/r^3$. The Fresnel zone is defined as that region of the field of an antenna between the reactive near-zone region and the far-zone region where the radiation fields predominate but wherein the angular field distribution (that is, the dependence on θ and ϕ) is dependent on the distance r from the antenna. Both the reactive near-zone and Fresnel zone are usually simply referred to as the *near-zone*. Finally, the *far-zone* is the region where the angular field distribution is essentially independent of the distance r from the antenna. In this region the fields decay as $1/r$. The far-zone fields – namely those at observation points (r,θ,ϕ) that are distant from the antenna – are best considered in terms of their transverse and radial components. It is found that :

■ The *radial* components of the fields (namely E_r and H_r) are negligible compared to the transverse components in the far-zone region of the antenna, so that we can say

$$E_r(r,\theta,\phi) = \hat{r}\cdot\bar{E}(r,\theta,\phi) \approx 0 \qquad H_r(r,\theta,\phi) = \hat{r}\cdot\bar{H}(r,\theta,\phi) \approx 0 \qquad \text{(A-3)}$$

■ The components of the *transverse* fields take the form

$$E_\theta(r,\theta,\phi) = F_\theta(\theta,\phi)\frac{e^{-jkr}}{r} \qquad \text{(A-4)}$$

and

$$E_\phi(r,\theta,\phi) = F_\phi(\theta,\phi)\frac{e^{-jkr}}{r} \qquad \text{(A-5)}$$

so that the transverse electric field is

$$\bar{E}(r,\theta,\phi) = \bar{F}(\theta,\phi)\,\frac{e^{-jkr}}{r} \qquad \text{(A-6)}$$

with

$$\bar{F}(\theta,\phi) = F_\theta(\theta,\phi)\,\hat{\theta} + F_\phi(\theta,\phi)\,\hat{\phi} \tag{A-7}$$

If we set E_r and H_r to zero then from the Maxwell curl equations in the far-zone of an antenna (and ***only*** in the far-zone) are related through

$$\bar{H}(r,\theta,\phi) = \frac{1}{\eta}\hat{r}\times\bar{E}(r,\theta,\phi) = \frac{1}{\eta}\hat{r}\times\bar{F}(\theta,\phi)\frac{e^{-jkr}}{r} \tag{A-8}$$

with $\eta = \sqrt{\mu_o / \varepsilon_o}$. The structure of the electromagnetic fields in the near-zone of an antenna is more complicated than that in the far-zone.

APPENDIX B

Fields of an Infinitesimal Electric Dipole

A z-directed infinitesimal magnetic dipole of strength I_e, located at the origin of the coordinate system, has fields [HARR 68]

$$E_r(r,\theta,\phi) = \frac{\eta_0 I_e}{2\pi}\cos\theta\left\{\frac{1}{r^2}+\frac{1}{jk_0 r^3}\right\}e^{-jk_0 r} \tag{B-1}$$

$$E_\theta(r,\theta,\phi) = \frac{j\eta_0 k_0 I_e}{4\pi}\sin\theta\left\{\frac{1}{r}+\frac{1}{jk_0 r^2}-\frac{1}{{k_0}^2 r^3}\right\}e^{-jk_0 r} \tag{B-2}$$

$$E_\phi(r,\theta,\phi) = 0 \tag{B-3}$$

$$H_r(r,\theta,\phi) = 0 \tag{B-4}$$

$$H_\theta(r,\theta,\phi) = 0 \tag{B-5}$$

$$H_\phi(r,\theta,\phi) = \frac{jk_0 I_e}{4\pi}\sin\theta\left\{\frac{1}{r}+\frac{1}{jk_0 r^2}\right\}e^{-jk_0 r} \tag{B-6}$$

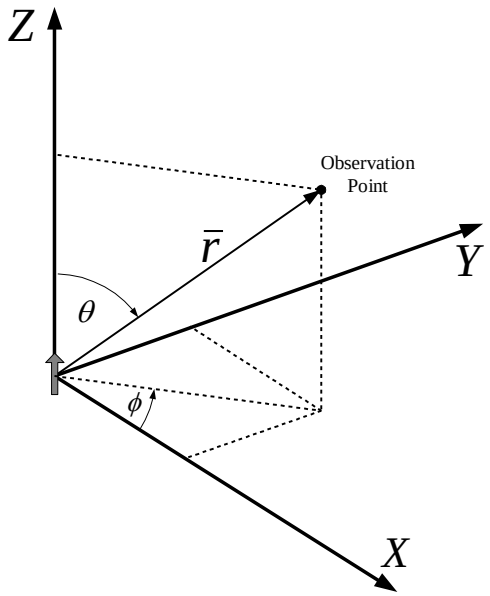

Fig. B-1 : $\hat{z}$ - Directed infinitesimal electric dipole located at the coordinate origin

The far-zone forms of these dipoles are obtained by taking the limit as $r \to \infty$. In the far-zone (B-1) through (B-6) hence become

$$E_r(r,\theta,\phi) = 0 \tag{B-7}$$

$$E_\theta(r,\theta,\phi) = \frac{j\eta_0 k_0 I_e}{4\pi} \sin\theta \, e^{-jk_0 r} \tag{B-8}$$

$$E_\phi(r,\theta,\phi) = 0 \tag{B-9}$$

$$H_r(r,\theta,\phi) = 0 \tag{B-10}$$

$$H_\theta(r,\theta,\phi) = 0 \tag{B-11}$$

$$H_\phi(r,\theta,\phi) = \frac{jk_0 I_e}{4\pi} \sin\theta \, e^{-jk_0 r} \tag{B-12}$$

APPENDIX C

Fields of an Infinitesimal Magnetic Dipole

A z-directed infinitesimal magnetic dipole of strength I_m, located at the origin of the coordinate system can, by applying duality [HARR 68] to the expressions in Appendix B, be found to be

$$E_r(r,\theta,\phi)=0 \tag{C-1}$$

$$E_\theta(r,\theta,\phi)=0 \tag{C-2}$$

$$E_\phi(r,\theta,\phi)=-\frac{jk_0 I_m}{4\pi}\sin\theta\left\{\frac{1}{r}+\frac{1}{jk_0 r^2}\right\}e^{-jk_0 r} \tag{C-3}$$

$$H_r(r,\theta,\phi)=\frac{I_m}{2\pi\eta_0}\cos\theta\left\{\frac{1}{r^2}+\frac{1}{jk_0 r^3}\right\}e^{-jk_0 r} \tag{C-4}$$

$$H_\theta(r,\theta,\phi)=\frac{jk_0 I_m}{4\pi\eta_0}\sin\theta\left\{\frac{1}{r}+\frac{1}{jk_0 r^2}-\frac{1}{k_0{}^2 r^3}\right\}e^{-jk_0 r} \tag{C-5}$$

$$H_\phi(r,\theta,\phi)=0 \tag{C-6}$$

The far-zone forms of these dipoles are obtained by taking the limit as $r\to\infty$ and allowing the $e^{-jk_0 r}/r$ terms to fall away, to give

$$E_r(r,\theta,\phi)=0 \tag{C-7}$$

$$E_\theta(r,\theta,\phi)=0 \tag{C-8}$$

$$E_\phi(r,\theta,\phi)=-\frac{jk_0 I_m}{4\pi}\sin\theta e^{-jk_0 r} \tag{C-9}$$

$$H_r(r,\theta,\phi)=0 \tag{C-10}$$

$$H_\theta(r,\theta,\phi)=\frac{jk_0 I_m}{4\pi\eta_0}\sin\theta\, e^{-jk_0 r} \tag{C-11}$$

$$H_\phi(r,\theta,\phi)=0 \tag{C-12}$$

APPENDIX D

Transformations of Coordinate Systems & Associated Vector Fields

The first part of this description applies when the observation point $\bar{r} = (r, \theta, \phi)$ can be any point whatsoever. The last part, starting just below Fig.D-2, applies to observation points at infinity (that is, in practice in the far-zone of the antenna).

Consider a vector $\bar{F}$ written in the form of a column vector. The column vector may contain its rectangular coordinate system components[66] $[F_x, F_y, F_z]^T$ or spherical coordinate system components $[F_r, F_\theta, F_\phi]^T$. If the matrix $\left[T_c^s\right]$ represents the transformation of the vector from its rectangular form to spherical component form, namely

$$[F_r, F_\theta, F_\phi]^T = \left[T_c^s\right][F_x, F_y, F_z]^T \tag{D-1}$$

then [RAHM 79]

$$[T_c^s] = \begin{pmatrix} \sin\theta\cos\phi & \sin\theta\sin\phi & \cos\theta \\ \cos\theta\cos\phi & \cos\theta\sin\phi & -\sin\theta \\ -\sin\phi & \cos\phi & 0 \end{pmatrix} \tag{D-2}$$

The inverse of this transformation ("going the other way") from spherical to rectangular components is then

$$[T_s^c] = [T_c^s]^{-1} = \begin{pmatrix} \sin\theta\cos\phi & \cos\theta\cos\phi & -\sin\phi \\ \sin\theta\sin\phi & \cos\theta\sin\phi & \cos\phi \\ \cos\theta & -\sin\theta & 0 \end{pmatrix} \tag{D-3}$$

[66] Superscript 'T' denotes the transpose operation.

If we denote by $[F'_{x'}, F'_{y'}, F'_{z'}]^T$ the rectangular components of the same vector in another coordinate system (call it the primed coordinate system) related to the unprimed coordinate system via the Euler angles, then these may be related by a matrix $\left[A_c^{c'} \right]$ as

$$[F'_{x'}, F'_{y'}, F'_{z'}]^T = \left[A_c^{c'} \right] [F_x, F_y, F_z]^T \tag{D-4}$$

where [RAHM 79]

$$\left[A_c^{c'} \right] = \begin{bmatrix} A_{11} & A_{12} & A_{13} \\ A_{21} & A_{22} & A_{23} \\ A_{31} & A_{32} & A_{33} \end{bmatrix} \tag{D-5}$$

with

$$\begin{aligned} A_{11} &= \cos\gamma\cos\alpha - \sin\gamma\cos\beta\sin\alpha \\ A_{21} &= -\sin\gamma\cos\alpha - \cos\gamma\cos\beta\sin\alpha \\ A_{31} &= \sin\beta\sin\alpha \\ A_{12} &= \cos\gamma\sin\alpha + \sin\gamma\cos\beta\cos\alpha \\ A_{22} &= -\sin\gamma\sin\alpha + \cos\gamma\cos\beta\cos\alpha \\ A_{32} &= -\sin\beta\cos\alpha \\ A_{13} &= \sin\gamma\sin\beta \\ A_{23} &= \cos\gamma\sin\beta \\ A_{33} &= \cos\beta \end{aligned} \tag{D-6}$$

In other words, $\left[A_c^{c'} \right]$ transforms a vector written in terms of its rectangular components in the unprimed system to the same vector but written in terms of its rectangular components in the primed coordinate system. The inverse transformation matrix is

$$[A]_{c'}^{c} = \begin{bmatrix} A_{11} & A_{12} & A_{13} \\ A_{21} & A_{22} & A_{23} \\ A_{31} & A_{32} & A_{33} \end{bmatrix}^{-1} = \begin{bmatrix} A_{11} & A_{21} & A_{31} \\ A_{12} & A_{22} & A_{32} \\ A_{13} & A_{23} & A_{33} \end{bmatrix} \tag{D-7}$$

Consider therefore the vector

$$\begin{bmatrix} E'_{r'}\left(r',\theta',\phi'\right) \\ E'_{\theta'}\left(r',\theta',\phi'\right) \\ E'_{\phi'}\left(r',\theta',\phi'\right) \end{bmatrix} \tag{D-8}$$

defined a point P in space described by spatial coordinates $\left(r',\theta',\phi'\right)$ in the primed coordinate system, and expressed in terms of the spherical coordinate unit vectors $\left(\hat{r}',\hat{\theta}',\hat{\phi}'\right)$. The same point P has spatial coordinates $\left(r,\theta,\phi\right)$ in terms of the unprimed coordinate system. Then the same vector expressed in terms of the spherical coordinate unit vectors $\left(\hat{r},\hat{\theta},\hat{\phi}\right)$ is

$$\begin{bmatrix} E_r\left(r,\theta,\phi\right) \\ E_\theta\left(r,\theta,\phi\right) \\ E_\phi\left(r,\theta,\phi\right) \end{bmatrix} = [T]_c^s\ [A]_{c'}^{c}\ [T]_{s'}^{c'} \begin{bmatrix} E'_{r'}\left(r',\theta',\phi'\right) \\ E'_{\theta'}\left(r',\theta',\phi'\right) \\ E'_{\phi'}\left(r',\theta',\phi'\right) \end{bmatrix} \tag{D-9}$$

By omitting $[T]_c^s$ in (D-9) we of course obtain

$$\begin{bmatrix} E_x\left(r,\theta,\phi\right) \\ E_y\left(r,\theta,\phi\right) \\ E_z\left(r,\theta,\phi\right) \end{bmatrix} = [A]_{c'}^{c}\ [T]_{s'}^{c'} \begin{bmatrix} E'_{r'}\left(r',\theta',\phi'\right) \\ E'_{\theta'}\left(r',\theta',\phi'\right) \\ E'_{\phi'}\left(r',\theta',\phi'\right) \end{bmatrix} \tag{D-10}$$

Lastly we want to relate the position vector of the point P, written entirely in terms of its components in the unprimed system to its components written entirely in terms of its components in the primed system. This is

$$\begin{bmatrix} r'\sin\theta'\cos\phi' \\ r'\sin\theta'\sin\phi' \\ r'\cos\theta' \end{bmatrix} = [A]_c^{c'} \begin{bmatrix} r\sin\theta\cos\phi - \tau_x \\ r\sin\theta\sin\phi - \tau_y \\ r\cos\theta - \tau_z \end{bmatrix} \qquad \text{(D-11)}$$

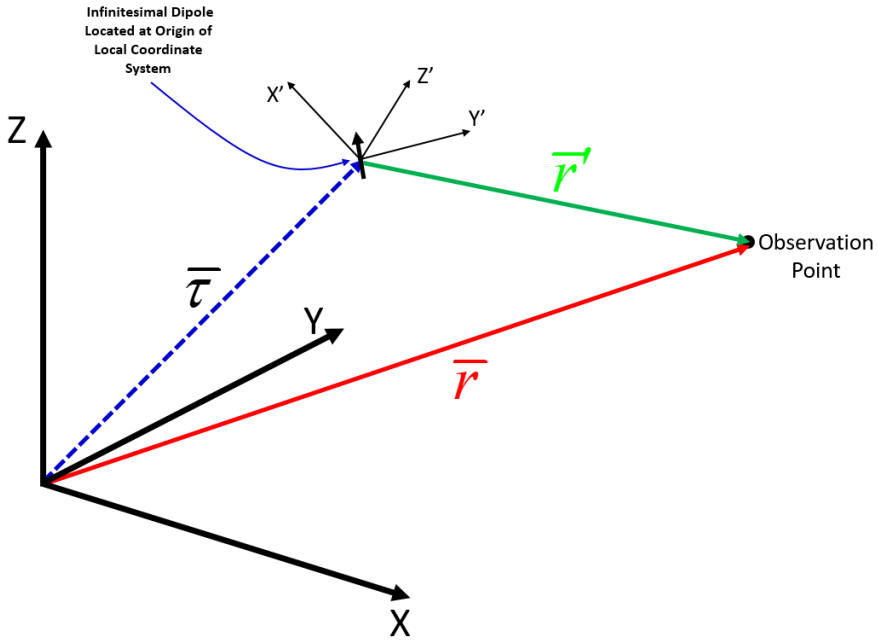

Fig.D-1 : Primed and unprimed coordinate systems.

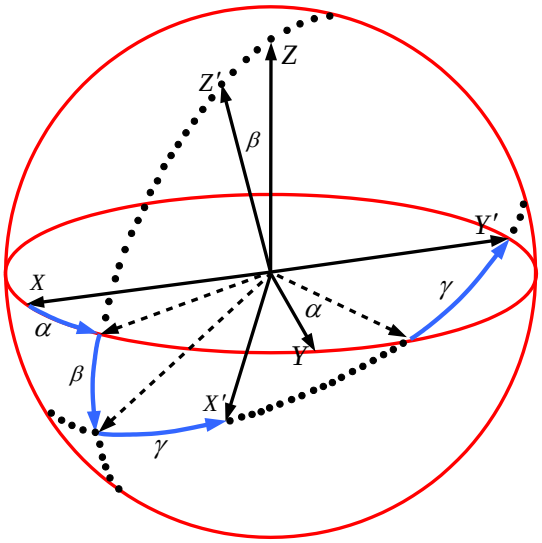

Fig.D-2 : Euler angles.

We next consider the manner in which the above coordinate transformation process simplifies when the observation point is at infinity. Let us now assume that the dipole offset $\left[\tau_x, \tau_y, \tau_z\right]^T$ is now zero, and hence $r' = r$ in (D-11), therefore we may write

$$\begin{bmatrix} \sin\theta'\cos\phi' \\ \sin\theta'\sin\phi' \\ \cos\theta' \end{bmatrix} = [A]_c^{c'} \begin{bmatrix} \sin\theta\cos\phi \\ \sin\theta\sin\phi \\ \cos\theta \end{bmatrix} \tag{D-12}$$

Once the far-zone direction (θ, ϕ) has been specified all terms in the right hand side of (D-12) are known, and this can be used to find $\sin\theta'\cos\phi', \sin\theta'\sin\phi' \,\&\, \cos\theta'$. Suppose we set

$$\begin{bmatrix} \sin\theta'\cos\phi' \\ \sin\theta'\sin\phi' \\ \cos\theta' \end{bmatrix} = \begin{bmatrix} b_1 \\ b_2 \\ b_3 \end{bmatrix} \tag{D-13}$$

From the bottom equation in (D-13) we have $\sin\theta' = \sqrt{1-(b_3)^2}$. This must be positive, because $0 \le \theta' \le 180^o$, over which $\sin\theta' \ge 0$. From the top equation in (D-13) we have $\cos\phi' = b_1 / \sin\theta'$, and from the middle equation in (D-13) it follows that $\sin\phi' = b_2 / \sin\theta'$. These last two expressions always apply unless $\theta' = 0^o$ or $\theta' = 180^o$, but for the latter values of θ' the value of ϕ' never matters. We can set it equal to any value we wish.

From the above we find that

$$\theta' = \cos^{-1} b_3 \tag{D-14}$$

$$\phi' = \cos^{-1}\left(\frac{b_1}{\sqrt{1-b_3^{\,2}}}\right) \tag{D-15}$$

ensuring that $0 \le \theta' \le 180^o$ and $0 \le \phi' \le 360^o$. Putting these results together, we can now use result (D-9) in the far-zone as

$$\begin{bmatrix} E_r(\theta,\phi) \\ E_\theta(\theta,\phi) \\ E_\phi(\theta,\phi) \end{bmatrix} = [T]_c^s\ [A]_{c'}^c\ [T]_{s'}^{c'} \begin{bmatrix} E'_{r'}(\theta',\phi') \\ E'_{\theta'}(\theta',\phi') \\ E'_{\phi'}(\theta',\phi') \end{bmatrix} \qquad \text{(D-16)}$$

This will give us the far-zone field of the dipole when it is located at the origin of the unprimed coordinate system, but suitably re-oriented in this system. We will denote this by $E_\theta^{orig}(\theta,\phi)$, $E_\phi^{orig}(\theta,\phi)$ & $E_r^{orig}(\theta,\phi)$.

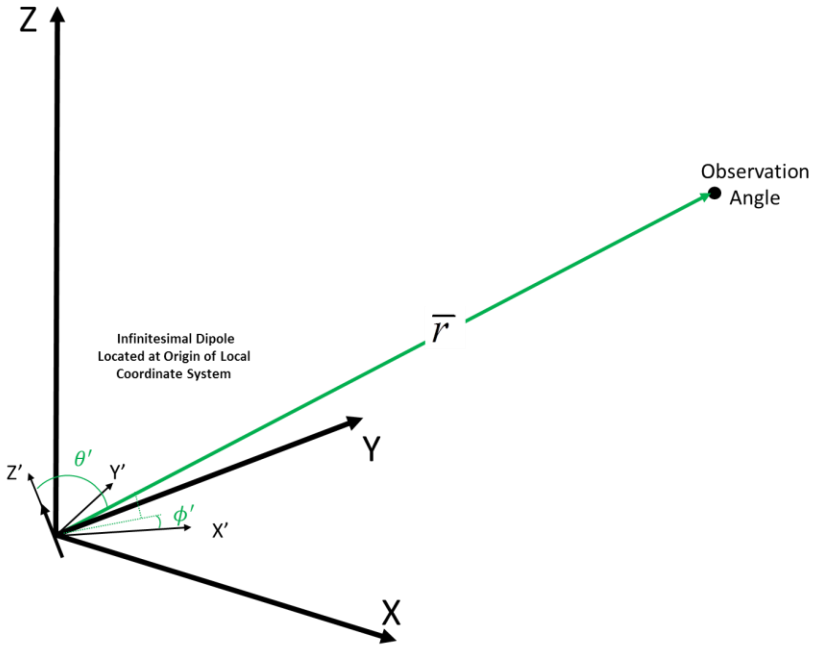

Fig.D-3 : Primed and unprimed coordinate systems for far-zone field representation.

With the dipole not at the origin of the unprimed coordinates, but instead at a point (x_o, y_o, z_o), these fields become

$$E_\theta^{shift}(\theta,\phi) = E_\theta^{ORIG}(\theta,\phi)\, e^{jk_0 x_0 \sin\theta\cos\phi}\ e^{jk_0 y_0 \sin\theta\sin\phi}\ e^{jk_0 z_0 \cos\phi} \qquad \text{(D-17)}$$

$$E_\phi^{shift}(\theta,\phi) = E_\phi^{ORIG}(\theta,\phi)\, e^{jk_0 x_0 \sin\theta\cos\phi}\ e^{jk_0 y_0 \sin\theta\sin\phi}\ e^{jk_0 z_0 \cos\phi} \qquad \text{(D-18)}$$

and

$$E_r^{shift}(\theta,\phi) = E_r^{ORIG}(\theta,\phi)\, e^{jk_0 x_0 \sin\theta\cos\phi}\ e^{jk_0 y_0 \sin\theta\sin\phi}\ e^{jk_0 z_0 \cos\phi} \qquad \text{(D-19)}$$

APPENDIX E

Antenna Under Test (AUT)

In order to validate computed fields at several points in the thesis we will need an AUT for which we know the complete fields (electric and magnetic) at any position in space, both near-zone and far-zone. Such information is not readily obtained through measurement (eg. even in standard NF measurements we only obtain the tangential components of the electric field over a sphere, and not the magnetic field also. A theoretical antenna model must therefore be used to satisfy this requirement, and act as a stand-in for actual measured near-field data. The AUT is a planar array consisting of $N_{array} \times N_{array}$ infinitesimal electric dipole elements[67], $q = 1, 2, ..., N_{array} \times N_{array}$, each with relative complex amplitude a_q, located at space at $(x_q, y_q, 0)$, and z-directed. A sketch for the case $N_{array} = 5$ is shown in Fig.E-1. Rigorous expressions for the field components[68] of such an element, of unit amplitude and located at the origin (the reference element) is provided in Appendix B. The fields of the AUT at any point in space $\bar{r}_{obs}$ (not only in the far-zone) is obtained by finding the field due to each of the elements in turn, using[69] the transformation in Appendix D, and then determining the AUT field though vector superposition. Thus the field, both electric and magnetic, of the AUT are known analytically. In this thesis we will use the 25-element planar array AUT. Parameters associated with the AUT are summarized in Table E-1.

[67] It should be remembered that these dipoles are unrelated to the infinitesimal dipoles that is used (in Section 4.4.4) in the determination of the incident fields field fields $\bar{E}^{inc}(S_{meas})$ and $\bar{H}^{inc}(S_{meas})$ in the NF-to-FF transformation procedure. Indeed, to avoid any confusion we will, after the present section, never again refer to the fact that the AUT is composed of infinitesimal dipoles because this is irrelevant to the way the fields of the AUT will need to be used. We will simply refer to a single-element AUT, a 4-element AUT and a 25-element AUT.

[68] At any point in space, and not only in the far-zone of the element.

[69] Because all but one dipole is located away from the origin. All dipole elements in the planar array have the same orientation though, namely parallel to the z-axis.

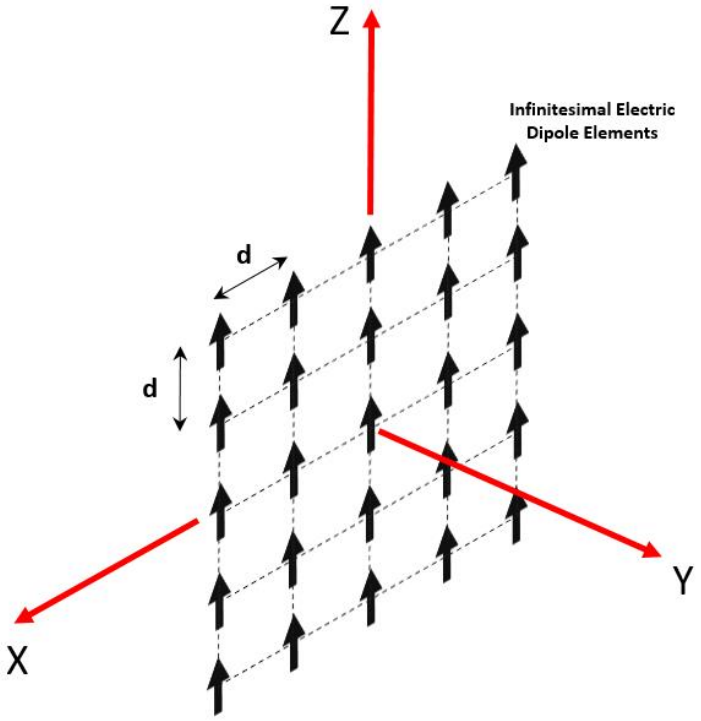

Fig.E-1 : 25-Element Planar Array AUT

Table E-1 : 25-Element Planar Array AUT

Quantity	Value
Frequency	1 GHz
Free Space Wavelength	300 mm
d	λ/2 = 150 mm
Outer Dimensions	4d × 4d
$\mathrm{MRS} = \sqrt{8}\,d$	1.4142 λ = 424.62 mm
$\Delta\theta$	2.18°
$\Delta\phi$	2.18°
Measurement Radius R_{meas}	900 mm (3λ)
Approximate Far-Zone Distance	9600 mm (32λ)

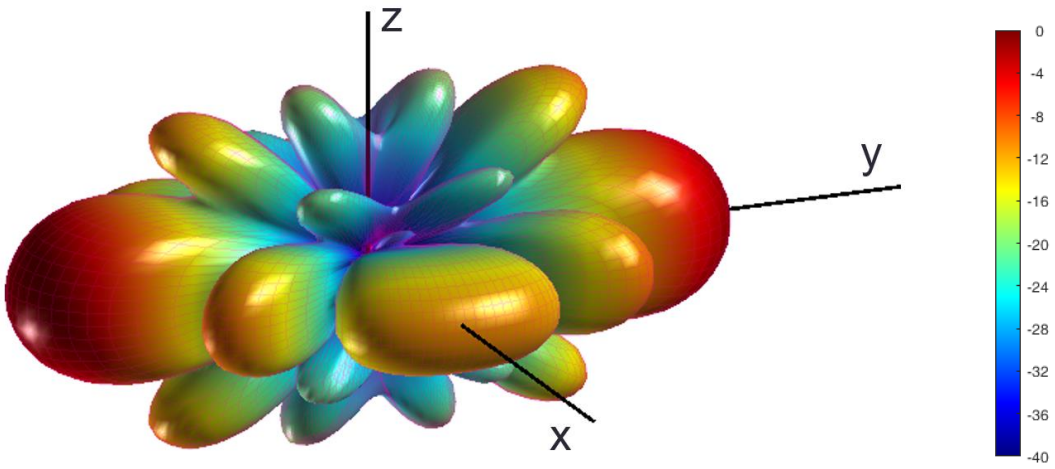

Fig.E-2 : 3D Radiation Far-Zone Pattern of $\bar{E}^{exact}\{AUT,\theta,\phi\}$ for the 25-Element AUT

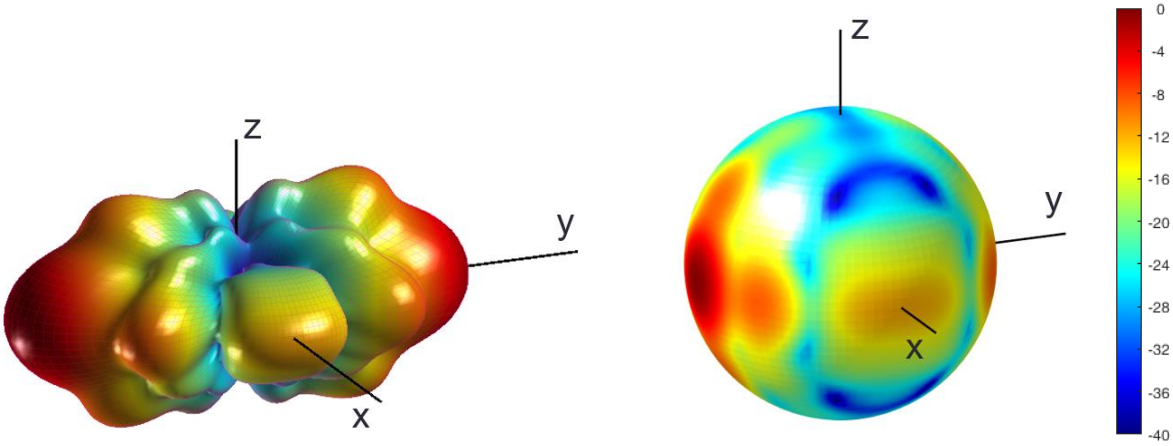

Fig.E-3 : 3D Radiation Near-Zone Field of $\bar{E}^{exact}\{AUT,S_{meas}\}$ for the 25-Element AUT

APPENDIX F

Use of the FFT in the Evaluation of Excitation Vector Terms

F.1 Introductory Remarks

Evaluation of excitations in the MM formulation requires finding solutions to integrals that are identified as having the form of the continuous Fourier transform (CFT). The objective is to carry out these operations using the FFT on a computer.

We consider the following individual excitation term, for a single i^{th} expansion function, taken from a portion of the MFIE excitation evaluation in (2.4-16), to illustrate the approach:

$$\mathbb{I}_{ni}^{t} = \int dt\, \rho f_i(t) \int_0^{2\pi} \left(\hat{t} \times \hat{n}\right) \cdot \overline{H}^{inc} e^{-jn\phi} d\phi \qquad \text{(F-1)}$$

F.2 Geometry

For numerical evaluation in the MM formulation, the triangle functions, $\rho f_i(t)$ are discretized into 4 individual parts, which is expressed as:

$$\mathbb{I}_{ni}^{t} = \sum_{q=1}^{4} T_q w_q \int_0^{2\pi} \left(\hat{t} \times \hat{n}\right) \cdot \overline{H}^{inc} e^{-jn\phi} d\phi \qquad \text{(F-2)}$$

The discretization is illustrated graphically in Fig.F-1. The relationship between the nodes (ρ_i^-, z_i^-) belonging to triangles, and the spans t_i, indicating where the q = 1,2,3,4 parts of the triangle are evaluated, is illustrated in Fig.F-2. The BOR span locations are at $t_i = \left(\frac{\rho_i^- + \rho_{i+1}^-}{2}, \frac{z_i^- + z_{i+1}^-}{2} \right)$ and lie midway between the (ρ_i^-, z_i^-) points in the t-direction along the generator.

The summations in equation (F-2) are straightforward over the q=1,2..4 parts of the N_t expansion functions. With careful bookkeeping, one may avoid repeating calculations that arise due to overlapping nature of the triangles. The solution of equation (F-2) need only be done once for each unique span between nodes, but, of course, excitations must be carefully reassembled into the form implicit in equation (F-2).

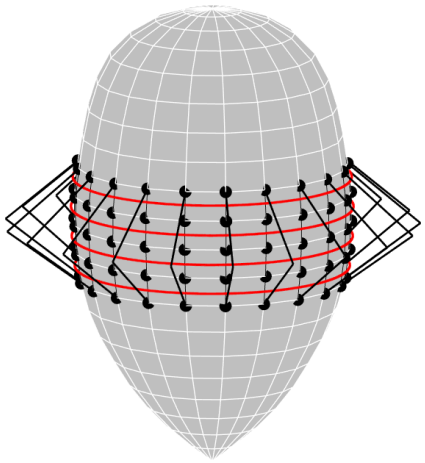

Fig.F-1 : The discretization & domain of the excitation in equation (F-2) for the fifth expansion function (i=5). The expansion function is triangular in t, and harmonic in phi. The triangles are illustrated at discrete azimuths, but are in fact continuous in azimuth. The four q^{th} parts of the BOR spans associated with the triangle are indicated as continuous red bands.

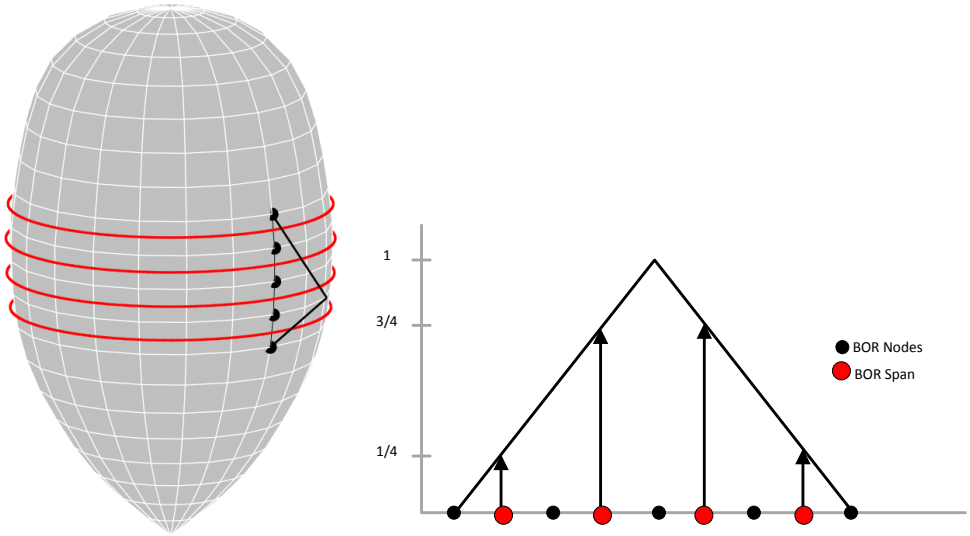

(a) **(b)**

Fig.F-2 : (a) Expansion function for i = 5 with the associated triangle illustrated at a single azimuth. The four q^{th} parts at which the triangle is to be evaluated are shown as red bands. (b) Illustration of (black) BOR nodes, which support the triangle and the (red) BOR spans at which the integral is to be evaluated. The w_q weights of the triangle are indicated on the y-axis.

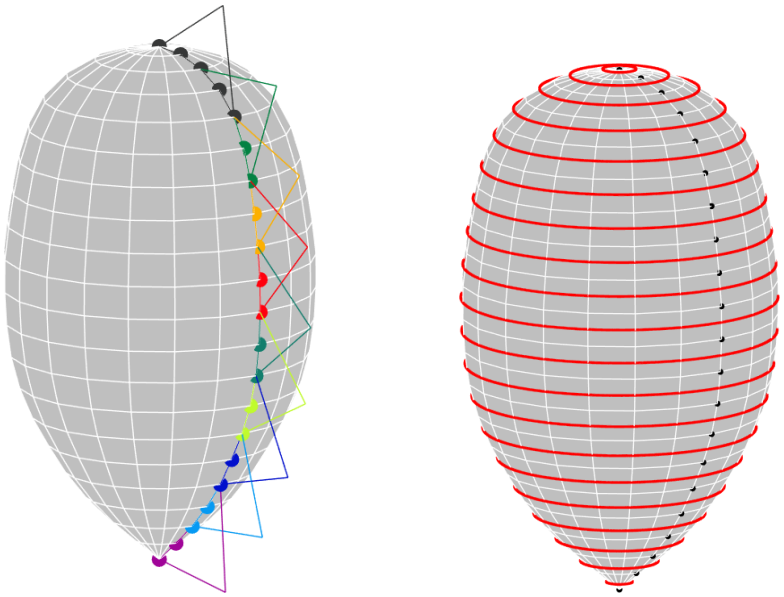

(a) **(b)**

Fig.F-3 : (a) Illustrating the overlapping nature of the triangles of the expansion functions. (b) Illustration of unique nodes (ρ_i^-, z_i^-) (as black dots), and spans, t_i, (red) associated with unique evaluations of the integral term of equation (F-2). Solution of equation (F-2) must only be sought once around each of the red rings.

F.3 Weights

Equation (F-2) indicates weighting terms T_q and w_q. The w_q terms for the triangles are $\left[\frac{1}{4},\frac{3}{4},\frac{3}{4},\frac{1}{4}\right]$ and are as illustrated in Fig.F-2(b). The weights T_q, that are defined in reference [MAUT 77, Eq.(29)], are dependent upon the distribution of node points in our generatrix set (ρ_i^-, z_i^-). Determination of the weights involves calculation of slant-distances, d_i, along the generatrix, as

$$d_i = \sqrt{\left(\rho_{i+1}^- - \rho_i^-\right)^2 + \left(z_{i+1}^- - z_i^-\right)^2} \qquad \text{(F-3)}$$

The T_q weights are then calculated via

$$T_1 = \frac{kd_{i-2}^2}{2\left(d_{i-2} + d_{i-1}\right)} \tag{F-4}$$

$$T_2 = \frac{k\left(d_{i-2} + \frac{d_{i-1}}{2}\right)d_{i-1}}{\left(d_{i-2} + d_{i-1}\right)} \tag{F-5}$$

$$T_3 = \frac{k\left(d_{i+1} + \frac{d_i}{2}\right)d_i}{\left(d_i + d_{i+1}\right)} \tag{F-6}$$

$$T_4 = \frac{kd_{i+1}^2}{2\left(d_i + d_{i+1}\right)} \tag{F-7}$$

F.4 The Fast Fourier Transform (FFT)

Having sorted the discretization of the geometry and the summations and weights, of equation (F-2), we turn to the evaluation of the integral term

$$\int_0^{2\pi} \left(\hat{t} \times \hat{n}\right) \cdot \overline{H}^{inc} e^{-jn\phi} d\phi \tag{F-8}$$

The incident field $\overline{H}^{inc}$, and local coordinates $\hat{t}$ & $\hat{n}$ all vary azimuthally, but are at a fixed t-value along the surface in equations (F-2) and (F-8). To highlight the relationship with the continuous Fourier transform (CFT) and justify use of the discrete Fourier transform (DFT), we may write all terms in the integrand, other than the exponential one, as $f\left(\phi\right)$, and rewrite (F-8) as

$$\int_0^{2\pi} f\left(\phi\right) e^{-jn\phi} d\phi \tag{F-9}$$

For clarity regarding the related signal-processing discussion, we will switch to the generally standard signal-processing nomenclature from here throughout the remainder of this appendix. Time and frequency signals are referred to throughout; however, it should be noted that the

Fourier transform can be applied to signals of other dimensions, for example a probability density function can be mapped to a characteristic function using the Fourier transform [WALK 97]. In the MM case the analogous Fourier transform relationship pair is ϕ-to-harmonic frequency. We thus hereby alter our notation, and **reassign variables n, t and x** as

$$n \triangleq \text{generalized index} \tag{F-10a}$$

$$t \triangleq \text{general variable, typically time} \tag{F-10b}$$

$$x \triangleq \text{discrete time record name} \tag{F-10c}$$

In [SCHW 59, Eq.(2-11a)] equation (F-9) is written as the form yielding the Fourier coefficients c_n

$$c_n = \int_0^{2\pi} f(t) e^{-j\omega_n t} dt \tag{F-11}$$

for a periodic function, $f(t)$, with period $T = 2\pi$, and is expressed by [SCHW 59, Eq.(2-10a)] as

$$f(t) = \frac{1}{T} \sum_{-\infty}^{+\infty} c_n e^{j\omega_n t} \tag{F-12}$$

Equation (F-12) is a statement that the function can be represented by a Fourier series, and the coefficients of the solution of our integral are the Fourier coefficients c_n. Equation (F-11) is recognized as the CFT, which [LYON 11, Eq.3-1] expresses as

$$X(f) = \int_{-\infty}^{+\infty} x(t) e^{-j2\pi ft} dt \tag{F-13}$$

and gives the discrete Fourier transform (DFT) exponential form in [LYON 11, Eq.3-2] as

$$X(m) = \sum_{n=0}^{N-1} x(n) e^{-j2\pi nm/N} \tag{F-14}$$

MATLAB defines the FFT almost identically, and starts indexing at 1.

$$X(m)=\sum_{n=1}^{N}x(n)e^{-j2\pi(n-1)(m-1)/N} \qquad \text{(F-15)}$$

The offset in n for the summation presents no difficulty and so we use the FFT to obtain the Fourier coefficients c_n of equation (F-11).

All that remains is to set the sample duration, T, the sample interval Δt, apply any necessary scaling factors and circularly shift the FFT results so that the negative frequency components are spectrally below the positive ones. The sample duration of our integral is defined along a circle and so is periodic, with period $T=2\pi$.

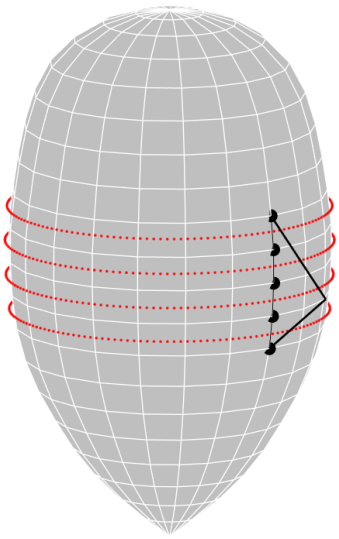

Fig. F-4 : Discrete azimuthal sample locations for the i = 5 expansion function involved in evaluation of the excitation via the FFT.

The relationship between the sample period, T, and the sampling interval Δt is illustrated below, after [WALK 97], for a generalized periodic function, of period T.

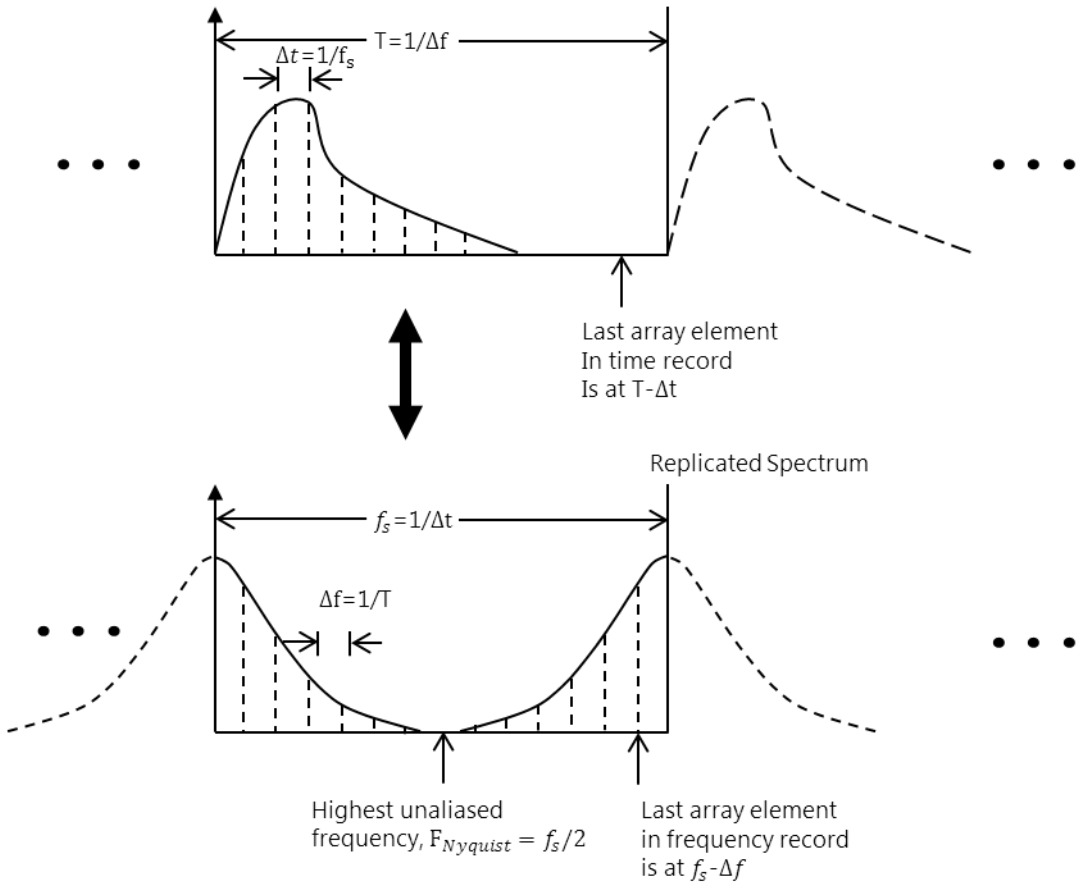

Fig.F-5 : Relationship between (a) the discrete time record $\{x(n)\}$ (top) and the discrete frequency record $\{X(m)\}$ on the bottom

Only a single period is stored in the discrete time and frequency record arrays from 0 to 2π and 0 to f_s, respectively. The period of the replicated time record is $T = 1/\Delta f$ and for the replicated frequency record is $f_s = 1/\Delta t$. The time record $\{x(n)\}$ will consist of samples at $\{0, \Delta t, 2\Delta t, ..., T - \Delta t\}$ whereas the frequency record $\{X(m)\}$ will consist of samples at $\{0, \Delta f, 2\Delta f, ..., f_s - \Delta f\}$. The time record will have $N = T/\Delta t$ elements. Because there are N samples, the frequency resolution is $\Delta f = f_s / N$.

FFT results will have unique values in the samples record up to the Nyquist frequency, beyond which the values correspond to negative frequencies. Therefore the FFT results must be shifted circularly by N/2 indices to interpret the FFT results as if it were a frequency spectrum with both positive and negative frequencies. This shifting operation is implemented as the

fftshift command in MATLAB. Once so shifted, the samples correspond to spectral frequencies, in Hz, from $-f_S/2$ to $f_S/2$ in frequency steps of $\Delta f = f_s/N$. In order to obtain integer angular frequencies ω_n in equation (F-11) these frequencies in Hz ought to be multiplied by 2π to correspond to our (integer) angular harmonic frequencies for plotting, as in figure (F-6) & (F-7).

Finally is the issue of magnitude scaling factors of our FFT. Because the Fourier coefficients in equation (F-11) are for a generalized function in equation (F-12) which includes a 1/T term, we must multiply the frequency record $\{X(m)\}$ by the period, T, to get the correct value. In our solution we decided to define the sample interval by specifying the Nyquist frequency. Doing things this way allowed us to predetermine the highest angular harmonic that may be accurately sampled. This decision implicitly specifies the sampling rate $\Delta t = 1/(2*F_{Nyquist})$ (or $\Delta\phi$, in fact). This signifies we can tailor a solution to accurately measure up to a prescribed azimuthal harmonic order. In this way we set the maximum harmonic we wish to measure accurately. For example, if we expect that only 20 such harmonic modes are excited, it would not make sense to sample at such a tiny interval that achieved a Nyquist frequency of, say, 1000.

In summary, to solve the integral in equation (F-9), we sample the continuous function $f(\phi)$ at an appropriate sampling interval $\Delta\phi = 1/(2F_{Nyquist})$, which is specified via the desired Nyquist frequency & hence obtain the sample record $\{x(n)\}$, having N points. To solve the integral, we process the sample record via equation (F-16), which is written using MATLAB function notation as:

$$\int_0^{2\pi} f(\phi)\, e^{-jn\phi} d\phi = fftshift\left(fft(\{x(n)\})\right) \cdot \frac{2\pi}{N} \qquad \text{(F-16)}$$

F.5 Excitation Spectra

In the MM formulation when one expresses the excitation vector for use in a solution, it is necessarily for one specific azimuthal harmonic, and the $\hat{t}$ - and $\hat{\phi}$-directed excitation responses are stacked, and each block ordered according to expansion function index. Not so with a solution based upon the FFT. In that case things are flipped so that one will simultaneously obtain the solution for *all* harmonics for *one* specific expansion function. This difference allows us to easily visualize the excitation magnitudes and provides insight into the bandwidth and spectral features in the modal excitation.

Selected spectral plots for a θ-polarised plane-wave incident upon a 0.2 λ radius sphere, at an oblique incident angle of (θ, ϕ) = (30°, 0°) are shown illustrating the frequency amplitude spectrum. The solution specified $N_t = 40$ expansion functions and the FFT was configured with a harmonic Nyquist frequency of $F_{Nyquist}$ = 50. The normalization is performed relative to the largest excitation magnitude in the solution across all harmonics and all expansion functions.

Fig. F-6 shows the $\hat{t}$-directed excitation terms for the EFIE solution with $N_t = 40$ expansion functions. At left are the excitations for the first expansion function (i = 1), at the bottom of the sphere, and at right is the excitation at the expansion function straddling the equator (i = 20) for the two different excitation response orientations. The high signal to noise ratio of the DFT solution can be seen, and it is clear that there is no angular frequency components of significance higher than about the 20th azimuthal harmonic. The harmonic excitation clearly has a broader spectral bandwidth at the equator than at the pole which intuitively makes sense given that a larger radial dimension could more easily support higher azimuthal modes. Fig.F-7 shows the corresponding $\hat{\phi}$-directed excitation vector terms. While the excitation magnitudes and bandwidths are similar to the t-response case, it is striking that that there is no DC harmonic in the $\hat{\phi}$-terms, in contrast to the $\hat{t}$-terms.

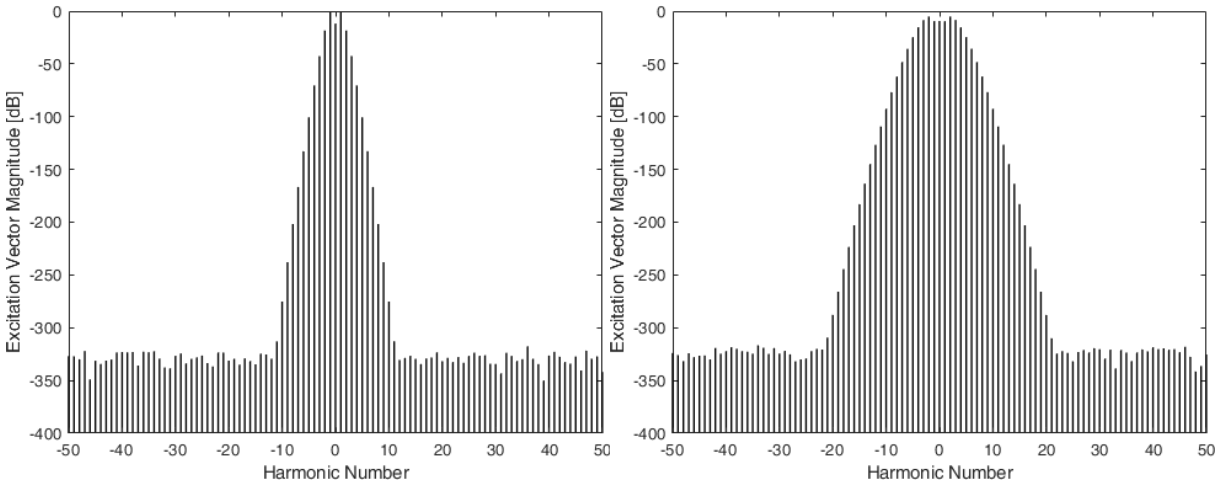

Fig.F-6 : (a). $\hat{t}$ -directed excitation vector magnitude response for the electric field for the EFIE for the *i* = 1 expansion function on the left; (b). $\hat{t}$ -directed excitation vector magnitude response for the equatorial expansion function (*i* =20) on the right.

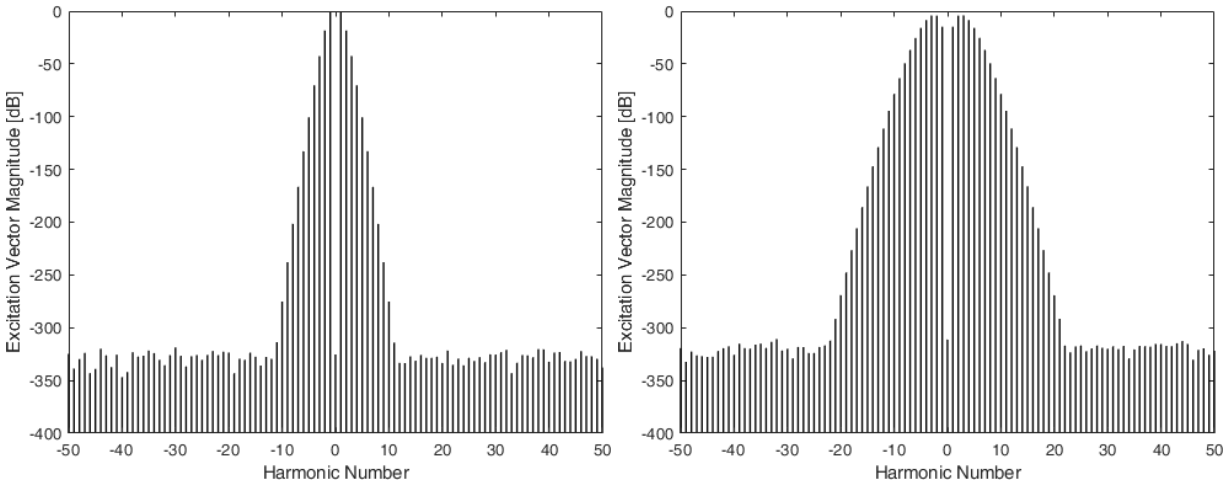

Fig.F-7 : (a). $\hat{\phi}$ -directed excitation vector magnitude response for the electric field for the EFIE for the *i* = 1 expansion function on the left; (b). $\hat{\phi}$ -directed excitation vector magnitude response for the equatorial expansion function (*i* = 20) on the right.


DEUS
EST
SCIENTIARUM DOMINUS